Unsteady Compressor Distortion Response and Compressor Instability

by

Robert E. Plumley

B.S. Mechanical Engineering, Michigan Technological University (1984)

SUBMITTED IN PARTIAL FULFILLMENT OF THE REQUIREMENTS FOR THE DEGREE OF

Master of Science
in
Aeronautics and Astronautics
at the
Massachusetts Institute of Technology

February, 1990

Signature of Author _____
Department of Aeronautics and Astronautics
November, 1989

Certified by _____
Professor Edward M. Greitzer
Thesis Supervisor

Accepted by _____
Professor Harold Y. Wachman
Chairman, Departmental Graduate Committee

Unsteady Compressor Distortion Response
and Compressor Instability

by

Robert E. Plumley

Submitted to the Department of Aeronautics and Astronautics
on October 27, 1989 in partial fulfillment of the
requirements for the Degree of Master of Science in
Aeronautics and astronautics

Abstract

An experimental and theoretical investigation of compressor response to rotating inlet distortions has been undertaken. The results show that the compressor stable flow range is strongly dependent on the distortion rotation rate. Compared to the situation with a stationary distortion, the stable flow range was improved for negative (contra-rotating) rotation rates and degraded for positive (co-rotating) rotation rates. In addition, the most severe decrease occurred, as predicted, at a rotation rate near that associated with the naturally occurring rotating stall modes in the compressor.

An experimental examination of compressor flow field instabilities prior to the onset of rotating stall was performed for undistorted and distorted flow. The presence of pre-stall travelling waves was observed. In the distorted case, the largest wavelike pertubations were seen at the location near the trailing edge of the low total pressure region, also as predicted by theory.

ACKNOWLEDGEMENTS

The author wishes to thank all of those who made the completion of this work possible, especially the following:

My advisor, Professor Edward M. Greitzer, for his help and guidance and for staying behind me even when I was in Cincinnati.

Dr. C.S. Tan for his friendliness, concern, and helpful advice.

Dr. J.P. Longley for all of his patient explanations, also for his computer programs without which....well, I don't like to think about that.

Mr. Bob Haimes for giving me help and extra space when I needed it.

Mr. Gwo-tung Chen and Mr. Randy Chue for teaching me to run some early codes.

Ms. Diana Park for helping me with Macintosh problems and letting me use her Mac II.

Mrs. Holly Rathbun for her help with financial matters.

Ms. Karen Hemmick for her help and for not complaining when I used her phone.

Mr. Mark Turner for bringing Tara in when he could.

Mr. Peter Curless for advising me to return to school; I hope to repay him someday.

Mr. Peter Silkowski, the best roomate I ever had, for his tolerance of me and for the many good times we shared.

Mr. George Pappas for his office courtesy and for exposing me to "different" music.

General Electric and especially Dr. D.C. Wisler for allowing us to conduct the experiment and without whom none of this would have been possible.

Mr. Terry Khera and Mr. Charlie Winters for designing and building the screen and screen control.

Dr. Brent Beacher for answering my questions about compressor blading.

Additionally, at General Electric I would like to thank the following five individuals who I worked with daily. They helped me stay happy and cheerful and made the year I spent there pass very quickly:

Dr. H.W. Shin for all of his patience, help with instrumentation and data reduction, and especially for lending me his fitness center card even though I didn't look like a "Shin".

Mr. Don Menner for his sincere interest in the project, the ridiculous hours he worked, and for allowing me to install the screen myself (the bleeding has stopped-thanks).

Mr. Gary Osterbrock for sharing his tools and running some crucial errands.

Mr. Bill Groll for sharing his electrical supplies with almost no grumbling, and for explaining many things, some even technical.

Mr. Thomas Herdman of Computer Horizons Corp. for helping me with some programming, and also for making me very proud of my truck.

I would also like to thank a few others for their friendship and companionship while they were here, but they finished and left before me, so they don't deserve to be mentioned.

A special word of thanks must go to the city and drivers of Boston for keeping my motivation to finish at a constant high level.

Other than the experimental work in Evendale, this project was conducted at the Gas Turbine Lab under a grant from the Air Force Office of Scientific Research, Dr. J.M. McMicheal and Capt. H. Helin, program managers. Financial support for the author was provided by the Air Force Research in Aero Propulsion Technology (AFRAPT) program, AFSOR-85-0288.

I must also thank my family and "soon to be" family for their love and support. This was not easy for them either.

Most especially I want to thank my fiancee, Linda, for her love, patience, and faith in me throughout this separation. She endured more than what was fair.

Table of Contents

Nomenclature

a = speed of sound

A = flow-through area

B = nondimensional stability parameter (defined in Chapter 6)

C = fourier coefficient

D = source parameter

DC(60) = distortion parameter (defined in Chapter 3)

f = distortion rotation rate = $\omega_{distortion}/\omega_{wheel}$

K = screen pressure drop coefficient (defined in Chapter 3)

L = normalized height of screen

L_{Tot} = overall effective length of compressor and ducting

n = n^{th} data point (Chapter 5) or harmonic number (Chapter 6)

N = number of data points

P = static pressure

PC = performance loss coefficient (defined in Chapter 5)

P_t = total pressure

r = mean radius

u = dimensionless velocities

U = mean wheel speed

v = dimensioned equivalent of u velocities

V = velocity normal to screen

V_{plenum} = volume of plenum

Y = unspoiled section of downstream flowfield (0<Y<1)

η = nondimensional effective length = L_{Tot}/r

λ = inertia parameter for rotors (defined in Chapter 6)

μ = inertia parameter for all blade rows (defined in Chapter 6)

ϕ = flow coefficient = axial velocity/U

ψ = nondimensional pressure rise in axisymmetric flow = $(P_2 - P_{t1})/\rho U^2$ or stream function for screen design (Chapter 3)

ω = angular velocity

θ = circumferential angle

ρ = density

σ = RMS of data (measure of probe sensitivity, defined in Chapter 5))

σ^* = RMS of RMS's (used to normalize sensitivity of probes, defined in Chapter 5)

subscripts

1 = compressor inlet

2 = compressor exit

I = irrotational region

II = rotational region

j = denotes which hot film probe

k = fourier number

m = mean quantity

List of Figures

Chapter 1 Introduction and Background Information

It is well known that a compressor operating with an inlet distortion suffers a loss in performance and that stall margin and peak pressure rise are also typically reduced. The importance of these effects has been recognized for many years, but the ability to predict these losses in stability and performance is still not adequate.

The current research project was prompted by recent interest in compressor stability with rotating inlet distortions such as might be encountered by a high pressure compressor fed by a fan or low pressure compressor which was operating in rotating stall. There is very little experimental data available for rotating inlet distortions. Figure 1-1 shows results from work by Ludwig and Nenni. For positive screen rotations, the compressor stability was demonstrated to be a very strong function of distortion rotation rate. The test compressor demonstrated greater stability with a contra-rotating distortion than it did with a distortion rotating in the same direction as the compressor. Similar trends were demonstrated in [2] (Figure 1-2).

Reference [3] describes a method to predict the onset of flow instability for low speed, high hub-to-tip ratio, axial compressors operating with a circumferential inlet total pressure distortion. In this approach, following [4], the pressure rise across a blade row is made up of two parts. One part is the pressure rise the compressor would see in steady uniform flow at the local flow condition. The second part is an unsteady correction to account for the deceleration and acceleration of the flow in the blade row as the blade row moves through the non-uniform flow. At any operating point, a formal linear stability analysis is used to determine stability.

Reference [3] described the method and the results of initial calculations. In reference [5], the work was extended to include, among other topics, the stability of a compressor

subjected to a rotating inlet distortion. The calculations showed the stability to be strongly dependent on rotation speed of the distortion for the particular compressor examined. Figure 1-3, taken from [5], shows the calculated variation in compressor performance with rotation rate. The calculated stability trends are seen to be in quantitative agreement with the above-mentioned experimental trends.

A operating point of a compressor will be unstable if any small unsteady perturbation grows in time, and other recent experimental work on this topic has been directed towards understanding the wave structure in the flow field just prior to inception of rotating stall. Recently, Garnier [6] showed the existence of stall "precursors", i.e. waves that travel around the compressor at some fraction of wheel speed before the inception of stall. While this is in accord with the analysis of Hynes and Greitzer, the physics of the unsteady flow field is not well understood. Understanding the flow field is important to assessing stability, and can also be applied to other applications, such as active stall controls.

The aim of this project was to experimentally measure compressor performance in the presence of rotating inlet distortions and compare these results to model predictions so that an assessment of the model's accuracy may be made. Another aim is to experimentally examine the unsteady flow field to provide further insight into the stall inception process.

Chapter 2 Purpose of Test and Proposed Test Plan

2.1 Purpose of Test

The experimental data reviewed in Chapter 1 show significant effects of rotating inlet distortions. Although the theoretical model predicted trends which had similar trends to the experimental results, no direct comparisons are possible due to insufficient data.

The primary purpose of the present test was to obtain experimental data on compressor performance with a rotating distortion so that a direct comparison to the theoretical model could be made. Obtaining speedlines for various distortion rotation rates was thus a first priority with flow field non-uniformities for various quantities a close second. Such profiles can not only be used to compare with the models, but can also serve to help diagnose the reasons for differences and shortcomings in the modelling.

An associated aspect of compressor performance is the stalling process. Previous investigations, mentioned earlier, have identified the presence of a pre-stall wave, but the phenomenon is not well understood, and general trends have not been established. Among the aspects to be confirmed are: do the waves always occur? How much time, in rotor revolutions, elapses between the precursor signal and stall inception? Does the wave signal always look the same? A part of this investigation was thus to gain additional information on the process of stall inception.

2.2 Proposed Test Plan

The test plan for the experiment at GE went through several iterations. A rough draft was sent to GE in February of 1988 and was discussed at GE in the spring of 1988. An updated version of the test program was written in January of 1989 after a visit by John Longley. Longley [7] had done the instrumentation for similar measurements, and his input

was valuable in determining the final version. This program was sent to GE, and it is listed in appendix A. An explanation of the goals of the various items in the plan is given below.

2.2.1 Undistorted Flow Compressor Characteristic

In order to do any calculations, of distorted flow stability and performance, it was necessary to obtain the undistorted flow characteristic, which is used to predict the distorted performance. For pre-test calculations (done primarily to help design the experiment), we used a characteristic we believed similar to the test compressor. We planned to obtain this characteristic in part 1 of the test plan although this was not laid out in any detail, because this information would be routinely obtained.

2.2.2 Distorted Flow Compressor Characteristic

Part 2 of the test was to determine the overall distorted compressor performance, total to static pressure rise versus flow coefficient for different rotation speeds. A time mean bellmouth pressure drop is used to determine the mass flow. The spatial static pressure variation was thus examined to see the effects of the distortion screen, and simple potential field calculations indicated that the resulting mass flow error should be less than one percent.

2.2.3 Flow Field Measurements

The mean exit static pressure was obviously necessary to determine the performance of the compressor. The time resolved exit static pressure was desired to see the variations in static pressure around the circumference due to the rotating distortion. Total pressure at the inlet was necessary to determine performance, and also as input to the calculations. Two element cross hot wires were proposed to measure the axial and circumferential velocities at the compressor inlet and exit. The time resolved static pressure at IGV inlet and throughout the compressor was also wanted. The model assumes little circumferential redistribution and these static pressure measurements would help determine how valid that assumption was.

2.2.4 Nature of Compressor Flow Field Unsteadiness

In parts 3 and 4 of the experiment, we planned to examine the nature of the compressor flow field unsteadiness. All of the performance instrumentation from part 2 was maintained, and, in addition, we added a ring of 8 hot wires placed at midspan about 0.7 radii upstream of the IGV's to examine any precursors to stall onset. This was done for both clean flow and steady distorted flow.

Chapter 3 Experiment Design

3.1 Distortion Choice

The majority of the experimental investigation was defined primarily to examine the effects of a rotating distortion, generated by an upstream screen. There were two basic parts in the process of selecting this screen; selection of the distortion (magnitude and extent), and then actual screen design.

To make these selections, calculations were run, using data based on the compressor characteristic in reference [8]. Square wave total pressure distortions were used as input for the calculations. Details of the calculations and inputs will be discussed in Chapter 6, and here we will only discuss some of the results that were used to guide the design of the distortion.

3.1.1 Distortion Sector

The first distortion consideration was the sector angle. Above a certain sector size, increasing the extent of the distortion has only a slight effect on the pressure rise at instability, as shown experimentally in reference [9]. Computed results for the test compressor can be seen in figure 3-1 for three total pressure distortion magnitudes. The so-called "critical sector" is about 90 degrees. The compressor characteristic used to do these calculations is the clean flow characteristic shown in figure 3-2. We chose the value of 120 degrees as one that would have a strong impact on performance, and one in which some experience had been gained [10].

3.1.2 Distortion Magnitude

To set the distortion magnitude, there are several constraints. We wanted a distortion that would yield measurable effects experimentally without being large enough to produce excessive swirl angles and hence separation at the inlet guide vanes. Longley [10] used two different distortion magnitudes. One had a DC(60)=0.36. The other had a DC(60)=1.0 where

$$DC(60) = \frac{P_t|_{\text{over } 360} - P_t|_{\text{worst } 60}}{\frac{1}{2}\rho U^2}$$

and a magnitude in this range seemed reasonable. Figure 3-2 shows the distorted characteristics and neutral stability point for a stationary square wave distortion of 120 degrees and several distortion magnitudes. The largest distortion, $0.12\rho U^2$, had a DC(60)=0.83.

3.2 Parametric Studies

To calculate the compressor performance with inlet distortion, we need to know the compressor characteristic with uniform flow. As mentioned earlier, reference [8] was used to get data for the high flow side of the characteristic, and a parabola with its peak at the neutral stability point was used to fit the data. However, it was not clear how the behavior of the low flow side of the characteristic would affect the overall performance.

Longley [10] was able to experimentally find the low flow side of the axisymmetric characteristic by using mismatched downstream stages to stabilize the upstream test stage. No similar data was available for the low flow side of the GE compressor characteristic, and to examine the effect of this uncertainty, three additional low flow characteristics were used. These can be seen in figure 3-3. They were felt to envelope the possibilities. The neutral stability point and distorted characteristic were calculated for a stationary, 120 degree extent, $.12\rho U^2$ total pressure distortion for all four compressor characteristics, and the results are shown in figure 3-4. Clearly, each clean flow characteristic produced a different result, but they all had significant effects. Regardless of what the axisymmetric characteristic looked like, we felt that we would be able to see an appreciable impact due to the distortion.

The symmetric clean flow characteristic was then used with the 120 degree extent $.12\rho U^2$ total pressure distortion to calculate distorted characteristics and neutral stability points for several different distortion rotation speeds. The results are shown in figure 3-5.

3.3 Screen Design Methodology

After determining the desired distortion, the screen parameters of loss coefficient and extent necessary to get this distortion were determined and the type of screen chosen.

3.3.1 Screen Parameters

In determining the screen parameters, the analytic solution suggested by Koo and James [11] for flow through a normal screen was used. It will be briefly summarized here. Figure 3-6 defines the variables used in the analysis. The figure represents one-half of the unwrapped upstream channel because of symmetry. The velocity field is divided into two regions: region I outside the wake and region II inside. Streamline AC separates the two regions, and there is a step change in velocity across AC.

The fluid is assumed inviscid in both regions except in the immediate vicinity of the screen. Therefore, total pressure is conserved except across the screen itself. The far upstream flow is uniform and region I is irrotational. The equation for the streamfunction in region I is given by

$$\nabla^2\psi_I=0\,.$$

The screen is viewed as a continuous distribution of sources, and the method of images is used to find the upstream potential field generated by the screen. In the wake, the flow will generally be rotational. Therefore, in region II the streamfunction is given by

$$\nabla^2\psi_{II}= f(\psi_{II})\,,$$

where the unknown function, f, represents the vorticity generated by the screen. The solution for the overall flow can be expressed in terms of two unknown functions which are found using two matching conditions at the screen. The first matching condition is the requirement

that the velocity normal to the screen be continuous through the screen. For any point on the screen,

$$V_I(h) = V_{II}(h) ,$$

where V is the normal velocity in the subscripted region, and h is the vertical coordinate along the screen.

The other matching condition is given in terms of the screen pressure drop. The screen pressure drop coefficient, K, is a measure of the screen solidity and is defined by

$$K = \frac{\Delta P}{\frac{1}{2}\rho V^2} ,$$

where Δp is the change in static pressure across the screen. For a screen normal to the upstream flow, with negligible tangential velocities, total pressure and static pressure changes would be the same and either could be used in defining K. Therefore, the matching condition becomes

$$KV^2 = u_2^2 - u_3^2 .$$

where the notation is given in the figure.

For a screen normal to the flow, if the tangential velocities are neglected, the source strength can be shown to be uniform along the length of the screen. Given K and L, the extent of the screen (figure 3-6), the source strength parameter may then be found from an approximate relationship derived from the second matching condition.

$$K = \frac{2DK+(DK)^2}{(1+DK)^2}\left[1+\frac{DK}{2(1+L)}\right] ,$$

where D is the source parameter. Reference [11], which develops all of these equations, shows that this is a good approximation for the range of present interest.

The three velocities in figure 3-6 are all denoted in regions far from the screen; u_1 is the uniform far upstream velocity, and u_2 and u_3 are taken far enough downstream such that the streamlines are parallel. u_2 is in the high total pressure region, and u_3 is in the low total pressure region. These velocities can be found by differentiating the streamfunction, and the results can be written in terms of the known constants to give the following relationships:

$$u_1 = 1 - \frac{LDK}{2+DK},$$

$$u_2 = 1 + \frac{LDK}{2+DK},$$

$$u_3 = \frac{1}{1+DK}\left[1 + \frac{LDK}{2+DK}\right].$$

The velocity expressions are all dimensionless values, and since all the constants are positive, u_1 will be less than 1.

In addition to the uniform source distribution equation shown earlier, two more equations are needed to solve for the three unknown screen constants K, D, and L. Continuity is one equation, and can be written

$$u_2 Y + u_3(1-Y) = u_1,$$

where Y is the unspoiled sector of the downstream flow field as shown in figure 3-6. The final equation comes from the total pressure difference between the two downstream flow fields, the magnitude of the distortion. Since the downstream static pressure is uniform,

$$\Delta P_t = \frac{1}{2}\rho(u_2^2 - u_3^2) .$$

To solve these equations we must specify the magnitude and extent of the desired total pressure distortion. An example calculation is done here for a 120 degree extent and $.12\rho U^2$ magnitude distortion, where U is the mean wheel speed. Setting Y = 2/3 in the continuity equation gives a 120 degree distorted sector downstream of the screen and satisfies our first

criterion. If we substitute for the velocity relationships and rearrange terms, the equation becomes

$$L=\frac{2+DK}{6+5DK} .$$

For the total pressure distortion magnitude specified in this example,

$$\frac{\Delta P_t}{\rho U^2}=\frac{u_2^2-u_3^2}{2U^2}=0.12 .$$

The total pressure difference across the screen is equal to the total pressure difference between the downstream flow fields. Dividing both sides by the square of the upstream velocity and rearranging terms, we get

$$\frac{u_2^2-u_3^2}{u_1^2}=\frac{0.24}{\phi^2} ,$$

where ϕ is the mean axial flow coefficient. Based on mean wheel speed, the design point flow coefficient, ϕ, from [8] was approximately 0.44, which yields

$$\frac{u_2^2-u_3^2}{u_1^2}=1.24 .$$

Substituting for the velocity relationships and solving, we find

$$L=.264 \quad K=2.74 \quad D=.482 .$$

This value of L corresponds to roughly a 95 degree sector for the screen.

Values of L, K, and D were calculated for a range of total pressure distortion magnitudes, and figure 3-7 shows, for a range of distortion magnitudes, the variation in screen sector required to provide a 120 degree distorted sector downstream. Figure 3-8 shows how the required K varies with desired distortion magnitude for the same 120 degree downstream sector.

3.3.2 Screen Type and Other Considerations

A perforated plate was chosen for the screen because it would be more rigid and possibly more uniform then a round wire screen. In the situation of interest to us, the compressor would tend to narrow the distortion, so that based on "engineering judgement", we chose a 120 degree perforated plate (rather than 95 degrees).

After we knew the desired loss coefficient, the work of Cornell [12] was used to select the solidity of the screen. With his data, shown in figure 3-9, it was possible to go from a screen loss coefficient to a screen solidity. Selecting the solidity of the actual device, however, was not completely straightforward. The design of the mechanism that rotates the screen required that cylindrical struts be used to support the screen. The cylinders extended radially into the flow field just behind the screen. We considered just using the cylinders to generate the distortion. Because the necessary solidity of the cylinders was high, however, there was concern over non-uniformities in the downstream flow, and this was not done. Instead, the cylinders were placed every ten degrees with the screen wired onto the upstream side. It was not clear just how much additional loss (over the screen value) would be caused by the cylinders, but an upper bound was felt to be the total frontal area of the cylinders simply added to that of the screen to give an effective solidity. A lower bound would be to ignore the cylinders completely. We chose a compromise between these two giving a screen solidity of 0.42.

For the compressor characteristic we were using in our pretest work, the design mean flow coefficient was approximately 0.44. The design goal of

$$\frac{\Delta P_t}{\rho U^2} = 0.12$$

was thus equivalent to

$$\frac{\Delta P_t}{\rho V_m^2} = 0.62 \ .$$

Chapter 4 Experiment Hardware

4.1 Compressor

The experiment was conducted at the General Electric Aerodynamic Research Laboratory in Evendale, Ohio on the General Electric Low Speed Research Compressor. This compressor is extremely versatile and has been used to test many different types of rotor and stator blading. As built, the compressor had 4 identical stages of 54 rotor blades, 74 stator blades, and 53 IGV's. The mean values of stagger angle and chord length were 43 degrees and 4.3 inches for the rotors, 18 degrees and 3.2 inches for the stators, and 3.6 degrees and 3.3 inches for the IGV's. The compressor had a tip diameter of 5 feet, and a hub to tip ratio of 0.85. A drawing of half of the compressor is shown in figure 4-1. Except when stated to the contrary, the compressor was run at 500 rpm throughout the experiment.

4.2 Screen

Three different screen arrangements were used during the experiment. The original or standard distortion was created by a 120 degree sector 0.42 solidity perforated plate. A heavier distortion was created by attaching a 120 degree extent round wire screen to the upstream side of this plate. The round wire screen had .018" diameter wires, 12 wires per inch, and therefore an open area of 60.8%. The third configuration used only the original perforated plate, but cut into two 60 degree sectors placed 180 degrees apart. Except when stated to the contrary, the standard screen was used to generate the distortion.

4.3 Screen Installation

The rotating mechanism and support ring was designed by T. Khera of GE. An aluminum support ring of 5 foot inner diameter and 5.5 foot outer diameter was used to hold the screens. This ring was placed in a housing and held in place by retainer bearings. It was tapped every 10 degrees to allow insertion of support cylinders which extended radially inward

toward the center of the ring. The screen was safety wired to these cylinders. The 120 degree sector screens were wired to 13 evenly spaced support cylinders and each of the 60 degree sector screens was wired to 7 support cylinders. The wiring was done at 3 radial positions for the inner cylinders and at 5 radial locations for the 2 outer edge cylinders. The screen and support cylinders were weighed, and an equal mass of sheet metal was screwed into the inside edge of the ring 180 degrees away from the center of the screen to balance the ring. Based on the time resolved static pressure measurements to be discussed later, the counterbalance didn't seem to affect the flow field (only the effect of the screen can be seen).

4.4 Rotating Ring Control

The aluminum support ring was driven by a drive pulley $20^{7}/_{8}$ inches in diameter. The outer edge of the pulley was rubber, and contact friction was adequate to drive the aluminum ring. The drive pulley was attached to a 3 HP Reliance Electric motor. An Allen-Bradley AC motor drive regulated the power supplied to the electric motor. A Fenner M-Trim with an Ametek photo detector was chosen to sense and control the speed of the screen.

The original plan was to use this photo detector to sense the passing of a piece of reflective tape and to trigger data taking or at least give a position trigger. However, this was not possible due to reflections from the aluminum ring. Spray painting the edge of the ring black was tried, but the drive wheel rubbed the paint off in places. Because no sensitivity adjustment was possible, a filter was used over the sensor; this seemed to eliminate extraneous signals. An accurate speed reading required at least 100 signals per minute, and because we planned to run the screen at speeds lower than 100 rpm, three additional evenly spaced strips of tape were used.

This arrangement worked well for speeds up to about 50 rpm, but above that, the readings became erratic. A different speed sensor was thus used, IRD Mechanalysis model

245 automatic balancer. This did not work well for low speeds (less than 50 rpm) but it did work for all higher speeds we tried. Between the two sensors, we were able to measure all the screen speeds to within 1%.

4.5 Steady Instrumentation

The compressor, upstream and downstream ducting, and bellmouth are configured for steady state data taking, and no additional instrumentation was necessary for any of the requested steady data. The mean bellmouth pressure drop is measured at plane .1, as shown in figure 4-1 by 11 static pressure taps on the bellmouth and 11 more on the nose cone. Each of these sets of 11 lines feed into a single chamber and these two values are averaged to give the mean static pressure. The mean static pressure at the compressor inlet and exit were measured by a similar arrangement. The steady static pressure measurement at the compressor inlet is actually taken between the IGV row and the first rotor at plane 1.0. The IGV's had from 5 to 8 degrees of turning, however, so there was little change in the static pressure across them.

4.6 Dynamic Instrumentation

All the dynamic instrumentation was installed specifically for the present test. Not all of the instrumentation we requested was possible. The location and type of each of the dynamic probes that was used, are shown in figures 4-1. The single element hot films were TSI model 1210-20. The hot film signal passed through a TSI IFA-100 signal conditioner before going into a Kinetic Systems model 1502 Camac Crate. This performed an analog to digital conversion and stored the data in memory briefly before transferring the data to a file on a Microvax II. This temporary storage allowed a greater data retrieval rate because the Camac Crate can store data much more quickly than the Microvax. The two dimensional sensors were TSI model 1240-20 platinum hot films and the same conditioning and storage method was used for them.

Endevco series 8510b-2 high response piezoresistive pressure transducers were used to measure the unsteady static pressures. The signal passed through a Transamerica model PSC 8015-1 signal conditioner before going into the Kinetic Systems model 1502 Camac Crate. This data was then transferred to a file on the Microvax II. Unsteady total pressures were measured with Kulite Semiconductor model XB-1-187-2 G high response pressure transducers. The total pressure signals were conditioned and stored in the same manner as the static pressure signals. All of the dynamic data was stored on TK50 tapes for transfer to the GTL Microvax.

Chapter 5 Experiment and Results

5.1 Introduction

Due to time constraints on the Aerodynamic Research Laboratory facility, most of the actual compressor data were gathered in only two days of testing. Because of this, there was insufficient time to verify that all of the instrumentation was working properly, and as a result, some data we hoped to obtain was not gathered. However, considerable new information was obtained, and the main goal, the comparison with theory, could be carried out.

5.2 Rotating Stall Precursor

In this part of the experiment, we were looking for the structure of disturbances occurring prior to stall. The data were recorded by 8 evenly spaced single element hot films located at plane 0.4, (0.7 radii upstream of IGV's). The procedure was to set the compressor throttle at a position very close to stall, and then begin logging data, with the goal to have the compressor stall while data were being recorded. It was also important to take data at a point far from stall, to verify that what was seen near stall was indeed present *only* near stall.

Data reduction was straight forward, but involved several steps. Calibration data were first used to convert the raw data voltages into velocities, and a moving average was calculated for each of these traces. The moving average meant that every 5 points was averaged, and the average value replaced the middle point. In other words, each axial velocity value was replaced by one fifth the sum of itself, the two values immediately before, and the two values immediately after. The sampling frequency was 100 Hz, and since only 5 points were used in the moving average, only frequencies above 20 Hz would be smoothed. The precursor frequency is typically over 50% less than rotor passing frequency (8.33 Hz), so none of the precursor wave was eliminated.

It was obvious from the steady data that there were differences between the probes and calibrations, because the measured steady velocities differed by several percent. These differences in velocity were of the same magnitude as the precursor, and the mean velocity was thus subtracted from each trace to eliminate the differences. All of the probes thus had zero as their mean value, however, some were more sensitive than others. To correct this problem, the RMS value for each trace was calculated,

$$\sigma_j^2 = \frac{1}{N}\sum_{n=1}^{N}(v_j(n)-\overline{v_j})^2.$$

The subscript,"j", indicates which probe is being used, and the overbar indicates a mean value. The RMS of the RMS values was then calculated as follows:

$$\sigma^* = \sqrt{\sum_{j=1}^{8}\sigma_j^2}\ ,$$

and used to give all of the traces the same RMS value so that it would be possible to spot a precursor. This normalization technique was necessary to remove differences between probes, but it did not change any of the data. To look for a precursor, the technique that Garnier [6] used was repeated here. At each point in time, an FFT was done on the 8 signals,

$$C_k = \frac{1}{8}\sum_{j=1}^{8} V_j \exp\left[\frac{-2ijk\pi}{8}\right]$$

and the magnitude and phase of the first harmonic plotted against rotor revolutions. In figure 5-1, the growth of the amplitude of the first harmonic is shown. Rotating stall can be seen clearly towards the end of the trace where the magnitude is much larger. (The oscillations reflect a variation in probe sensitivity that was not eliminated by the normalization. The magnitude of the first harmonic, while in rotating stall, should be constant.) There is also a "bump" at about 17 revolutions and 2 smaller "bumps" between 20 and 30 revolutions. These represent a coherent first harmonic signal that we can identify.

More can be learned by examining the phase angle in figure 5-2. In the early part of the trace, up to about 8 compressor revolutions, the data points have no clear pattern. However, from just beyond 10 revolutions to 30 revolutions, a rough pattern exists in that a wave appears to be travelling around the annulus at about 20% of rotor speed. At the end of the trace, when the compressor is in rotating stall, it is clear that a wave is travelling around the annulus at roughly 45% of rotor speed.

To determine the frequency present in the first harmonic data trace shown in figure 5-1, a power spectral density analysis was used. This technique, which was used by Garnier [6], shows the strengths of the frequencies present in a signal. In figure 5-3, the PSD of the first harmonic is shown. The data sample for this PSD calculation included several revolutions of the compressor while it was operating in rotating stall. The frequency of the highest peak is 3.71 Hz, corresponding to a stall cell angular velocity of about 45% of rotor rotation.

In figure 5-4, we examined the signal for a shorter data sample that did not include rotating stall. The time interval brackets the bump that occurs around 17 revolutions in figure 5-1. Two peaks can be identified in figure 5-4. The 8.59 Hz peak represents the frequency of the rotor, and the highest peak is at a frequency of 1.56 Hz. This corresponds to a travelling disturbance at 18% of rotor speed, which is consistent with observations of the phase angle plot in figure 5-2. Figure 5-5 shows the interval from about 21 to 31.5 compressor revolutions. No frequency seems dominant here, but this is not surprising since the bump in figure 5-1 is not very large. The data show that a wave travels around the annulus prior to stall, although the signal to noise level is not adequate for further definition. The connection between the wave and the rotating stall is not clear, but the existence of the travelling waves is of interest by itself, for possible use as a stall warning.

Another aspect of wave behavior prior to stall is the influence of the distortion on the waveform. The qualitative behavior was predicted in reference [3], where it was suggested that the amplitude of the fluctuating wave would increase (with θ) in the low velocity region and decay in the undistorted region. The wave shape thus gives another point of reference with the modelling, and we can examine distorted inlet flow data to investigate this idea.

The distortion was stationary for all of these measurements. The recording procedure was identical to the one described above; we record a data trace that included unstalled as well as stalled data and examine the regime not in rotating stall. The velocity signals were processed for this portion of the analysis in the same manner as described earlier. The time average velocity for each probe is plotted in figure 5-6 as a triangle. Also shown are calculated velocity profiles for a stationary distortion at the same measurement plane and at the compressor inlet.

With reference to figure 5-6, consider the data in figure 5-7 which shows the maximum cross correlation for each set of adjacent wires. The cross correlation was obtained by first subtracting out the mean velocity from each trace. The resulting velocity fluctuations for adjacent wires were then multiplied together using different time delays. These were summed along the length of the data trace and then divided by the total number of points in the data trace. During this portion of the test, the sampling frequency was 100 Hz. Which is quite coarse, but the overall trend is clear. The cross correlations were done for time delays of .01 to .04 seconds. The time delay yielding the maximum cross correlation varied, but in the region of greatest interest (circumferentially close to 90 degrees), the maximum occurred at a time delay of .03 seconds The maximum cross correlation for that range is plotted at the circumferential point corresponding to the midpoint of the two probes that were used to do the correlation. For example, the maximum cross correlation between the probe at 90 degrees and the probe at 135 degrees is plotted at 112.5 degrees, half way between the probes. The calculated line is the square of the fluctuation of the most unstable eigenmode predicted by the

model adjusted so that theory and data would have the same peak. The agreement between the two plots is very good. As predicted by the theory, the maximum cross correlation occurs in the unspoiled region after growing in the spoiled region.

5.3 Data from Steady State Instrumentation

All of the performance data was measured with GE's existing instrumentation at the measuring planes shown earlier in figure 4-1. We use the mean wheel speed, U, to nondimensionalize velocities and the density times the square of the mean wheel speed, ρU^2, to nondimensionalize pressures.

5.3.1 Effect of Screen Rotation on Stall Points

To determine the stall points, the screen was brought up to the desired rotation speed with the compressor running at a stable throttle position. The compressor was then slowly throttled until stall occurred, and throttle position was then recorded. This was typically done at least twice. Stall could normally be clearly detected by ear, but the exit static pressure (which dropped considerably when rotating stall occurred) was also monitored. No other instrumentation was necessary.

With the standard distortion, this was done for a range of rotation speeds and three different compressor speeds, 500, 350, and 275 rpm. Choosing the lower speeds of 350 and 275 rpm enabled us to run at higher fractions of compressor speed without raising the actual speed of the distortion beyond 350 rpm, the ring rotation speed limit given to us by the designer. The resulting flow coefficient vs. rotation speed curves can be seen plotted in figure 5-8. Some calculated results are also shown here, although those will be discussed in Chapter 6.

Figure 5-8 demonstrates the dependence of the instability point on rotation speed. The compressor is most stable for negative distortion rotation rates. The flow coefficient at instability increases steadily with positive rotation until the smallest stable flow range is reached at about 30% of compressor speed, and then drops with further increase in screen rotation rate. A smaller increase in instability flow also appears at a rotation rate of about 70% of compressor speed.

In addition to the runs with the nominal distortion, stall points for the other 2 distortions (the 120 degree heavy distortion and the 2-60 degree sectors) were also found at a 500 rpm compressor speed. These are shown plotted together with the (500 rpm) results for the nominal distortion in figure 5-9. Similar trends can be seen with all three distortions.

5.3.2 Speedlines

Several speedlines were also recorded. As mentioned in Chapter 4, for the performance data, the pressure at plane 1.0 (upstream of rotor 1) was used as the inlet pressure. The total to static pressure rise was obtained by assuming the swirl downstream of the IGV's was negligible and subtracting the dynamic pressure based on the mean flow coefficient from the static to static pressure rise. The resulting speedlines are shown in figure 5-10 (static to static pressure rise), and figure 5-11 (total to static pressure rise). There is not much change in pressure rise, due to distortion, in contrast to the differences in stall flow.

The overall shape of the speedlines compared to the clean flow is thus quite similar. The speedline data is plotted in figure 5-12 as a performance loss coefficient against mean flow coefficient. The performance loss coefficient is defined as

$$PC(\phi) = \frac{\text{distorted pressure rise} - \bar{\psi}(\phi)}{\text{peak pressure rise in undistorted flow}}$$

This was used by Longley [10], and it will be discussed more in the next chapter when we compare measured and calculated results. However, even with this parameter which will amplify the effect of changes in pressure rise, one still sees little difference.

5.4 Flow Field Nonuniformity

For this portion of the test, the dynamic instrumentation was used. The flow field is steady in the frame of the distortion, and the figures will all be in this frame. They are plotted so that direction of increasing circumferential position, θ, corresponds to the direction of rotor rotation. (Note that for positive distortion rotations, this meant that the order of the points is reversed from the way in which the data was taken.) The sampling frequency used varied depending on the screen rotation rate but was chosen so that several revolutions of the screen could be recorded in each case. (For the stationary distortion case, the screen was rotated at about -3% of rotor speed.) Data traces were phase averaged to give a single average profile of a given quantity around the circumference. No screen position trigger was possible during the test, and this phase averaging was done by inspection of the traces, so that some of the different cases may be slightly out of phase relative to each other.

In figures 5-13 through 5-16, the static pressure profiles for plane .45 (.32 radii upstream of IGV's) are shown. A moving average has been used on the traces before the phase averaging was done. For clarity, positive and negative distortion rotations have been separated as well as the near stall and near design cases. Small differences emerge with changing rotation rate, but overall there is little variation between these profiles.

Since plane .45 is .32 radii upstream of the IGV's, the potential field of the compressor has decayed substantially there. The static pressures at plane 1.0 (upstream of rotor 1) have thus been plotted in figures 5-17 through 5-20. These profiles show a more pronounced variation with distortion rotation speed.

It was found that some of the X-film data was not within calibration range As a result, there is no velocity data for some of the cases for which the static pressure data was shown. The velocity profiles that were obtained are shown in figures 5-21 and 5-22. Bear in mind that the near stall velocity profiles have different mean flow coefficients because of the differences in their neutral stability points. The swirl angles for the same cases are shown in figures 5-23 and 5-24.

The total pressures are shown in figures 5-25 and 5-26. Total pressure measurements were unavailable, so these figures were actually obtained by combining the static pressure and dynamic pressure data, as discussed at length in Appendix B.

As was shown in figure 4-1, the static probes placed through the compressor were all at the same circumferential location. It was thus possible to see the evolution of the static pressure nonuniformity through the compressor, although the probe upstream of stage 4 was not working properly. Figures 5-27 through 5-42 show all available compressor outerwall static pressures. Further discussion of all of these measurements will be given in chapter 6 where direct comparisons to calculations can be made.

Chapter 6 Comparison of Calculated and Experimental Results

6.1 Calculation Input

One of the primary objectives of this project was to obtain experimental data on rotating inlet distortions to compare against model calculations. The calculations were performed with the method presented in [3] and [5], using the program written by John Longley. To run the model for comparison purposes, certain inputs were required, as described below.

6.1.1 Axisymmetric Characteristic

As mentioned earlier, the model requires a clean flow characteristic as input. Figure 6-1 shows the experimental data taken at GE with a parabola fitted through it. Because the low flow side of the characteristic is not known, the approach taken is to bracket the plausible low flow behaviors, and figure 6-2 shows the three characteristics that we have used. Unless stated otherwise, the symmetric characteristic is the characteristic used in the calculations.

6.1.2 Blade Geometry

Most of the necessary inputs were available from the blade geometry and other simple measurements of distances and volumes. Some of these appear in the equation for the compressor pressure rise with an unsteady inlet distortion,

$$\frac{P_2 - P_{t1}}{\rho U^2} = \psi(\phi) - (\lambda - \mu f)\frac{\partial \phi}{\partial \theta},$$

which was derived in [5]. The term, $\psi(\varphi)$, is the steady axisymmetric pressure rise characteristic. λ is the inertia parameter for the rotors, defined as follows:

$$\lambda \equiv \sum_{\text{rotors}} \frac{\text{axial chord}}{r\cos^2(\text{stagger})}.$$

The parameter μ is defined similarly, but includes the inertia of IGV's, stators, and rotors,

$$\lambda \equiv \sum_{\text{all blades}} \frac{\text{axial chord}}{r\cos^2(\text{stagger})}.$$

The variable, f, is actually a ratio of speeds and is defined as

$$f \equiv \frac{\omega_{\text{distortion}}}{\omega_{\text{compressor}}}.$$

Two other constants that come from the stability analysis are B and η [3]:

$$B \equiv \frac{U}{2a}\sqrt{\frac{V_{\text{plenum}}}{AL_{\text{Tot}}}},$$

and

$$\eta \equiv \frac{L_{\text{Tot}}}{r}.$$

The values used for these constants for both the pre-test calculations and the actual test compressor calculations, are tabulated below.

	pre-test	test conditions
λ	0.80	0.85
μ	1.40	1.45
B	0.024	0.024
η	6.7	6.7

6.1.3 Total Pressure and Screen Loss Assumption

In addition to the compressor geometry and characteristic described above, the total pressure distortion at compressor inlet is another required input to the calculation. As discussed in Appendix B, the total pressure profiles were generated from the static pressure and cross film data.

The model assumes that the total pressure profile used as input is the vortical, or far upstream total pressure. Therefore, only the total pressure profiles for the stationary distortion cases can be used directly as input. For a rotating distortion, the measured total pressure is made up of a vortical *and* a potential part. (The potential part comes from the unsteady

Bernoulli equation.) When doing the calculation for a rotating distortion, the model adds a calculated potential to the vortical total pressure used as input to determine the total pressure profile at the compressor inlet.

For the rotating case we have taken, as an initial assumption, the loss to be independent of rotation speed. As the speed of the screen rotation is increased, the flow relative to the screen is no longer normal, because the tangential component of velocity is nonzero, and this could change the loss coefficient. However, data show that the loss coefficient is not significantly affected for tangential velocities approaching the magnitude of the axial velocity, a 45 degree incidence angle [13]. A more serious concern is work done by the rotating screen on the flow, and we have not assessed this as yet.

The simple assumption was tested by running the model with a stationary distortion profile as input for various rotation speeds and comparing the measured and calculated total pressure profiles at station .45. The total pressure comparisons can be seen in figures 6-3 through 6-10.

Figures 6-5 and 6-9 are for the zero rotation cases, so we would expect the agreement there to be almost exact, as it is. For the f=0.3 and f=-0.3 rotation speeds, the agreement is quite good, but for the f=-0.6 cases, the agreement is not. The trends are similar, but the magnitude of the calculated distortion is greater than the measured distortion. As said, it is probable that the work done on the fluid by the rotating screen is significant, but we have not looked into this, and comparisons of the theoretical and experimental performance are made on the basis of the simple constant loss assumption.

6.2 Distorted Flow Compressor Performance

Figure 5-8 showed the calculated and measured neutral stability points for the standard

distortion. At high negative distortion rotations, the compressor is more stable. The stability decreases and seems to reach a minimum stability (maximum stalling flow coefficient) at about 0.3 experimentally and 0.5 theoretically. The calculated stalling flow coefficient becomes constant above about 70% of rotor speed. Similar results can be seen in figures 6-11 and 6-12 for the heavy distortion and the double distortion respectively.

The stalling flow coefficient, for increasingly high distortion rotation rates, is different for measurement and calculation. To examine whether this discrepancy might result from a poor representation of the low flow side of the axisymmetric characteristic, calculations were done to determine neutral stability points for the two other characteristics with different steepness. These results are shown in figure 6-13. Changing the low flow side does change the constant stall point for both large negative and, large positive rotation rates and may account for some of the difference, but this is clearly not all of the story. More importantly, it can not explain the differences in the high rotation rate values.

The measured data appears to asymptote to two different stall points. For large negative rotations, the value is approximately 0.425, but for large positive rotations, the value is higher, about 0.48. This change in the constant flow coefficient is not seen in the calculations. Regardless of which characteristic is used to do the calculations, the calculated stall point is the same for high and low rotations. Changing the characteristic changes the value of this constant, but it does not change the equality between high and low rotation speeds.

Figure 6-14 shows calculated speedlines for several distortion rotation rates. (The measured performance is shown in figure 5-11.) The performance loss coefficient is plotted against flow coefficient in figure 6-15 for the calculations and 5-12 for the measured results. The pressure rise is underestimated in all distorted cases, especially with the f=0.3 distortion rotation, but the trends with speed are the same for measurement and calculation. In order

from lowest to highest pressure rise at stall, the rotation speeds are 0.3, 0.0, -0.1, and -0.5 for both the measured and calculated results.

The results of Longley [10] were similar in that he also under predicted the pressure rise for a stationary distortion. Longley measured separation at the IGV's and postulated that the actual pressure rise might be higher because of the separation which created a more favorable incidence angle on the first rotor.

Another comparison of theoretical and experimental results can be made with the static pressure data. The static pressure profiles that were measured at plane 0.45 are shown in figures 5-13 through 5-16, with the mean of the measured values subtracted out. Direct comparisons of calculated and measured static pressure profiles are shown in figures 6-16a and 6-16b for near stall operating points, and 6-17a and 6-17b for near design operating points. No phase comparison is intended, but it is clear that the amplitudes do not agree.

A better examination of the static pressure data comes from examining the first harmonic. This is worthwhile because the model assumes that the low harmonics are the most important and Reid [9] showed that the low harmonics had the greatest affect on performance. The decay of the first harmonic through the compressor is shown in figures 6-18 and 6-19. In the figure, the measured and calculated data are centered on the rotation rate to which it corresponds. Note that some of the measured data does not "look" correct in spite of the fact that we have not found any errors in the data reduction process. Based on the known locations of the planes and the exponential decay of the static pressure nonuniformity away from the compressor face in either direction, the magnitude of the first harmonic should follow the trend of the calculations.

Chapter 7 Conclusions and Recommendations for Future Work

Sparse experimental evidence had shown that a compressor subjected to a rotating inlet distortion suffers a degradation of performance. General trends had been demonstrated experimentally and theoretically, but no direct comparisons between experiment and theory had been done.

Therefore, a stability assessment of a compressor with a rotating inlet distortion was carried out. The results, which were consistent with qualitative trends seen in earlier experimental work, gave a clearer quantitative picture of the phenomenon. There was a second bump at high positive rotation which was not shown in the earlier work. The Hynes-Greitzer model was able to predict the stability trends, but there are discrepancies, possibly indicating an aspect of flow field physics. At high positive rotation rates, the model predicts greater stability than what was seen experimentally.

The pre-stall flowfield investigation showed travelling waves at about 60% of stall cell speed, although more detailed experimental investigations are needed. The results of the experimental investigation of pre-stall travelling waves in distorted flow showed excellent agreement with the predictions of the Hynes-Greitzer model in that the travelling wave grew in the low velocity region and decayed in the high velocity region.

The total pressure loss prediction suggested in [11] was very helpful in designing the screen. The method was straightforward, and the agreement between prediction and experiment was very good. The decision to use the full 120 degree sector for the screen was a good choice.

It would have been nice to do the experiment iteratively. Problems like bad

connections, faulty probes and/or data channels and poor sampling frequencies can be eliminated if one can have a chance to examine the data. Other improvements are: A screen position trigger would help phase lock the data for different screen rotation cases. The measurements taken at plane .45 might have been done closer to the compressor face, say, one blade pitch upstream of the IGV's. (The decay of the compressor potential field was too large at plane .45.) The hot films used in the pre-stall flowfield investigation could also have been closer to the IGV's. In searching for the travelling wave, the ability to move the hot films radially might have been useful. (Measurements at the hub or tip might have revealed more about the wave.)

Although the experiment was done in a short time period, the rotating distortion results are complete. Trends were demonstrated, and model comparisons were made. Although the model matched stability trends qualitatively, there are some quantitative differences, especially for high rotation rates, and examinations might be pursued there. Further experimental investigation of the stall precursor would also be appropriate; understanding the unsteady flowfield prior to the inception of stall is an essential part of understanding and predicting compressor stability.

REFERENCES

1 Ludwig, G.R., Nenni, J.P. and Arendt, R.H. "Investigation of Rotating Stall in Axial Flow Compressors and the Development of a Prototype Stall Control System," Technical Report USAF-APL-TR-73-45, 1973.

2 Kozarev, L.A. and Federov, R.M., "Aspects of the Appearance and Elimination of Breakaway in an Axial-flow Compressor in the Presence of a Rotating Non-uniformity at the Inlet," *Izevstinya vuz Aviatsionnaya Tekhnika,* 1983, **26**(1), 33-37 (translated)

3 Hynes, T.P. and Greitzer, E.M. "A method for Assessing Effects of Inlet Distortion on Compressor Instabiity," *ASME J. Turbomachinery* 1987, **109**, 371-379.

4 Moore, F.K. "A Theory of Rotating Stall of Multistage Compressors," Parts I-III. *ASME J. Eng. Gas Turbines and Power* 1984, **106**, 313-336.

5 Chue, R., Hynes, T.P., Greitzer, E.M., Tan, C.S. and Longley, J.P., Calculations of Inlet Distortion Induced Compressor Flowfield Instability," *Int. J. Heat Transfer and Fluid Flow,* 1989, **10** No. 3, 211-223.

6 Garnier, V.H., "Experimental Investigation of Rotating Waves as a Rotating Stall Inception Indication in Compressors," GTL Report #198, June 1989.

7 Longley, J.P. personal communication, 1989.

8 Wisler, D.C.,"Loss Reductions in Axial-Flow Compressors Through Low Speed Model Testing," *ASME J,Eng.Gas Turbines and Power,* **107**, April 1985.

9 Reid, C., "The Response of Axial Flow Compressors to Intake Flow Distortion," ASME paper No. 69-GT-29.

10 Longley, J.P., "Inlet Distortion and Compressor Stability," Ph.D. Dissertation, Cambridge University Engineering Department, 1988.

11 Koo, J.-K. and James, D.F., "Fluid Flow Around and Through a Screen," *J. Fluid Mechanics,* **60**, part 3, 1973.

12 Cornell, W.G., "Losses in Flow Normal to Plane Screens," ASME Paper No 57-F19, 1957.

13 Schubauer, G.B., Spangenberg, W.G. and Klebanoff, P.S., "Aerodynamic Characteristics of Damping Screens," National Bureau of Standards, NACA TN 2001, January, 1950.

APPENDICES

Appendix A:

TEST PROGRAM FOR GE FOUR-STAGE COMPRESSOR

1. Assume that GE knows all relevant steady-state undistorted flow compressor performance parameters ($\psi(\phi)$, $\phi(\theta)$, etc.). Note: $\psi = (P_{out} - P_{t_{in}}) / \rho U^2_{mean}$

2. Distorted Compressor Performance (Compressor Characteristics)

The aim here is to measure the compressor performance when there is a rotating upstream inlet distortion. Those flowfield parameters which are measured are ones that are steady in the frame of reference of the inlet distortion.

Operating Conditions:

Screen rotation rate: $\omega_{distortion}/\omega_{rotor}$ = -1.0, -0.5, -0.25, 0.0 (or very slow), 0.1, 0.2, 0.3, 0.4, 0.5, 0.7, 1.0

Mass flow rate: between maximum possible to minimum unstalled

Total of 11 speedlines

Measurements:

Spatial & temporal mean bellmouth pressure drop
Spatial & temporal mean comp. exit static pressure

P_t(time)	IGV inlet, comp. exit	
ϕ(time)	IGV inlet, comp. exit	(cross hotwire)
v/U(time)	IGV inlet, comp. exit	(cross hotwire)
P_s(time)	IGV inlet, comp. exit	
P_s(time)	Casing statics through compressor (two per axial location)	

Note: Don't need to save cross wire data at all mass flows. Need it at near stall and near design condition. However, mean values of ϕ and pressures are required at all mass flows.

Measuring Procedure:

Digitally log (after anti-aliasing low pass filter) measurements at a frequency which will give ~100 points per one screen rotation with a screen position trigger. Record approximately 50-100 such traces and ensemble average.

The speedlines are the first priority. A very close second are the flow field measurements.

3. Nature of Compressor Flowfield Unsteadiness (Precursor)

The aim is to map, in detail, the flowfield instability boundary as a function of screen rotation speed, concentrating attention on the nature of the flowfield unsteadiness just prior to instability and during stall cell growth.

Operating Conditions:

Screen rotation rate: $\omega_{distortion}/\omega_{rotor}$ = -0.5, -0.25, 0.0 (very slow), 0.1, 0.2, 0.3, 0.4, 0.5
Mass flow rate: As near instability as possible so that stall occurs "almost naturally"

Measurements:

Spatial & temporal mean bellmouth pressure drop
Spatial & temporal mean comp. exit static pressure

P_t(time)	IGV inlet	
ϕ(time)	IGV inlet	(cross hotwire)
v/U(time)	IGV inlet	(cross hotwire)

Circumferential ring of 8 equally spaced hot wires aligned to measure axial velocity at mid span and mid axial station between screen and IGV (~1/2 radii ahead of compressor).

[If possible, a second ring midway between IGV's and above ring of wires ~1/4 radii ahead of compressor.]

Measuring Procedure:

Each ring of 8 wires must be simultaneously logged at a frequency which will resolve compressor rotation time scale (comp ~500 rpm? ~500-1000 Hz log).

Recorded data must include about 20-30 compressor revolutions prior to stalling event and early stall cell growth.

4. Nature of Compressor Flowfield Unsteadiness in Undistorted Flows
(A very short test program but a high priority item)

The requirement here is to determine the undistorted stall transients in flow.

Operating Conditions:

No inlet distortion screen
Compressor operation just before stall

Measurements:

Mean operating conditions
Circumferential ring of 8 equally spaced hot wires aligned to measure axial velocity

Different configurations:

(a) 8 wires at mid span ~1/2 radii ahead of compressor (same location as distorted flow measurements)

(b) 4 wires at tip (80% span) and 4 wires at hub (20% span), each equally spaced ~1/4 radii ahead of compressor

[If it is possible to get a ring of 16 equally spaced wires in the compressor, then use 8 at tip and 8 at hub.]

Measuring Procedure:

Same as in Section 3, i.e. simultaneously record data to resolve compressor rotation time scale for pre-stall event. Take 10 slow transients to stall.

5. Points

Range/sensitivity of high response data - adequate?
Do we need steady instrumentation to calibrate them?
Any other way of recording mean operating point?
Does GE have retrospective logging facility for stall?
Must phase log data to screen position (once per screen revolution and 100 per rev)

Note: We need the compressor mass flow with a rotating distortion - what is the easiest way to measure this?

6. Priorities

a. Speedline (in distorted flow)
b. Flow field measurements (in distorted flow)
c. Undistorted stall transients (stall cell precursor and evolution)
d. Rotating distortion stall transients (stall cell precursor and evolution)

Appendix B:

Generation of Total Pressure Profile for Input to Calculations

The total pressure profile is a necessary input to the calculations, however, the total pressure probes were not working during our test. We tried to generate the total pressure profile from the static and dynamic pressures, but the static pressure levels were not reasonable. The shapes of the profiles were believable, so we hoped that a constant factor error had been made in the calibrations. To test this possibility, we wanted to determine the effects of the compressor potential field. To do this, we examined the tangential velocity from the cross film data for a stationary distortion case.

For a stationary distortion, the tangential velocity results solely from the potential field generated by the compressor. This potential field would also be the sole cause of any static pressure nonuniformity. It is thus possible to take the tangential velocity profile and generate a static pressure profile. To do this, the measured tangential velocity was first decomposed into harmonics. Then according to the linearized treatment in [10], each harmonic is multiplied by

$$\frac{-\bar{\phi}n}{i|n|},$$

where n is the harmonic number, to give the harmonics of the static pressure profile. A plot of the resulting static pressure profile for the stationary standard distortion near design is shown in figure B-1. The measured static pressure was divided by 10 and plotted here as well, and the 2 profiles are similar, so the measured static pressure data is correct if it is divided by 10.

After obtaining a static pressure profile that we could trust, it was possible to determine the total pressure profile. At the same axial location as the upstream static pressure was measured, plane .45, the dynamic pressure was available from the absolute velocity measured by the cross hot film probe. The static pressure profile was phase shifted to account for the

screen rotation and the circumferential distance between the static probe and the cross hot film probe. A plot of the resultant total pressure profile for the stationary standard distortion near design is shown in figure B-2. Also shown in figure B-2 is the total pressure profile measured by GE after the experiment. To take this measurement, a kiel probe was used. The steady total pressure was measured every 10 degrees around the circumference with the ring rotated by hand between measurement points. This was done for both the standard and heavy distortions. For the heavy distortion, a comparison of the measured profile and the profile obtained by combining the static and dynamic pressures, as described above, is shown in figure B-3. The agreement in both cases is very good, so we have confidence in the reconstruction of the total pressure profiles.

A point of interest is the comparison between the predicted total pressure profile and the actual profile for the screen we designed. As discussed in Chapter 3, we aimed at a 120 degree square wave total pressure distortion with a magnitude of

$$\frac{\Delta P_t}{\rho V_m^2} = 0.62.$$

This has been plotted in figure B-4 along with the measured total pressure profile; the agreement between the two plots is good, and this supports the validity of the screen design methodology.

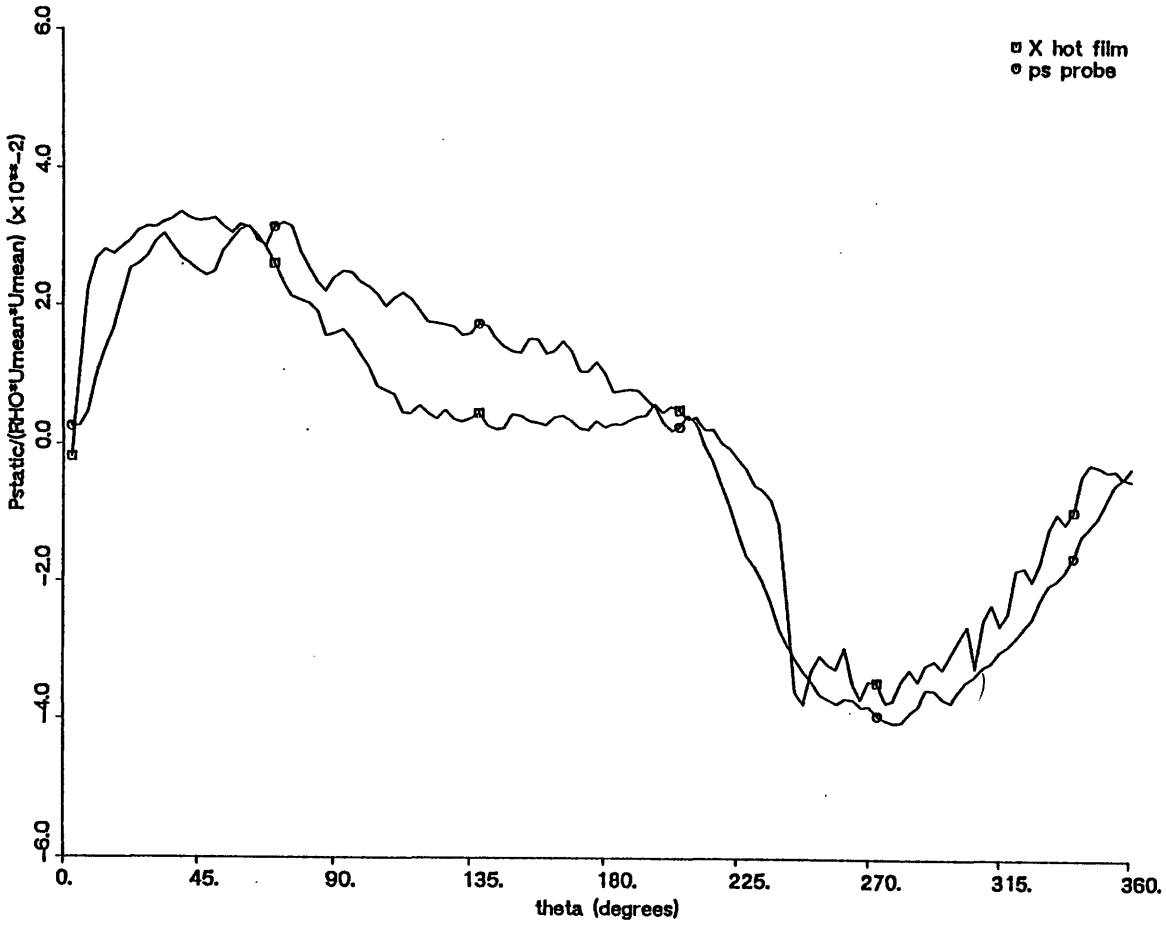

Figure B-1 Comparison of Static Pressures From Two Sources of Reduced Data, At Plane 0.45 (.32 radii upstream), f=0.0, Standard Distortion

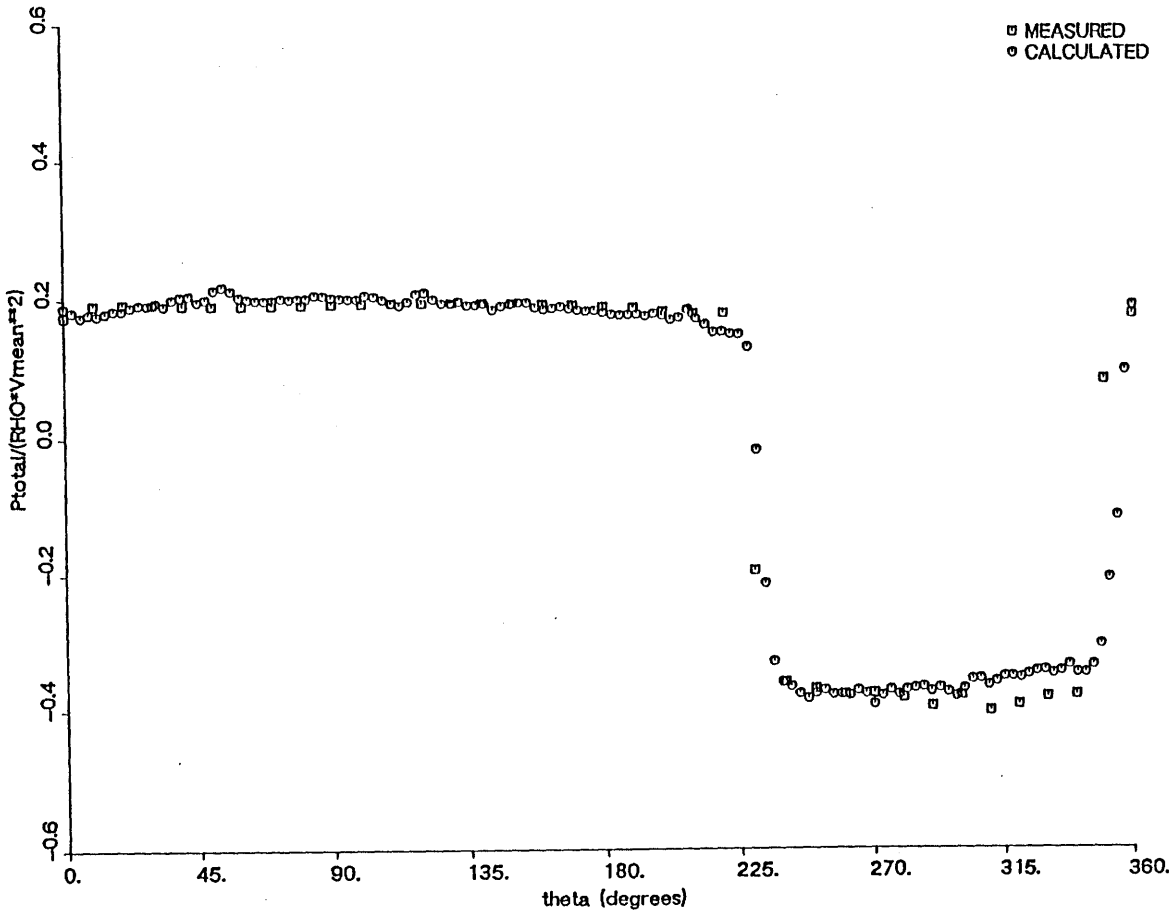

Figure B-2 Total Pressure Comparison: Post Test Kiel Probe Measurement Versus Static Probe and Cross Film Combination From Test, Standard Distortion

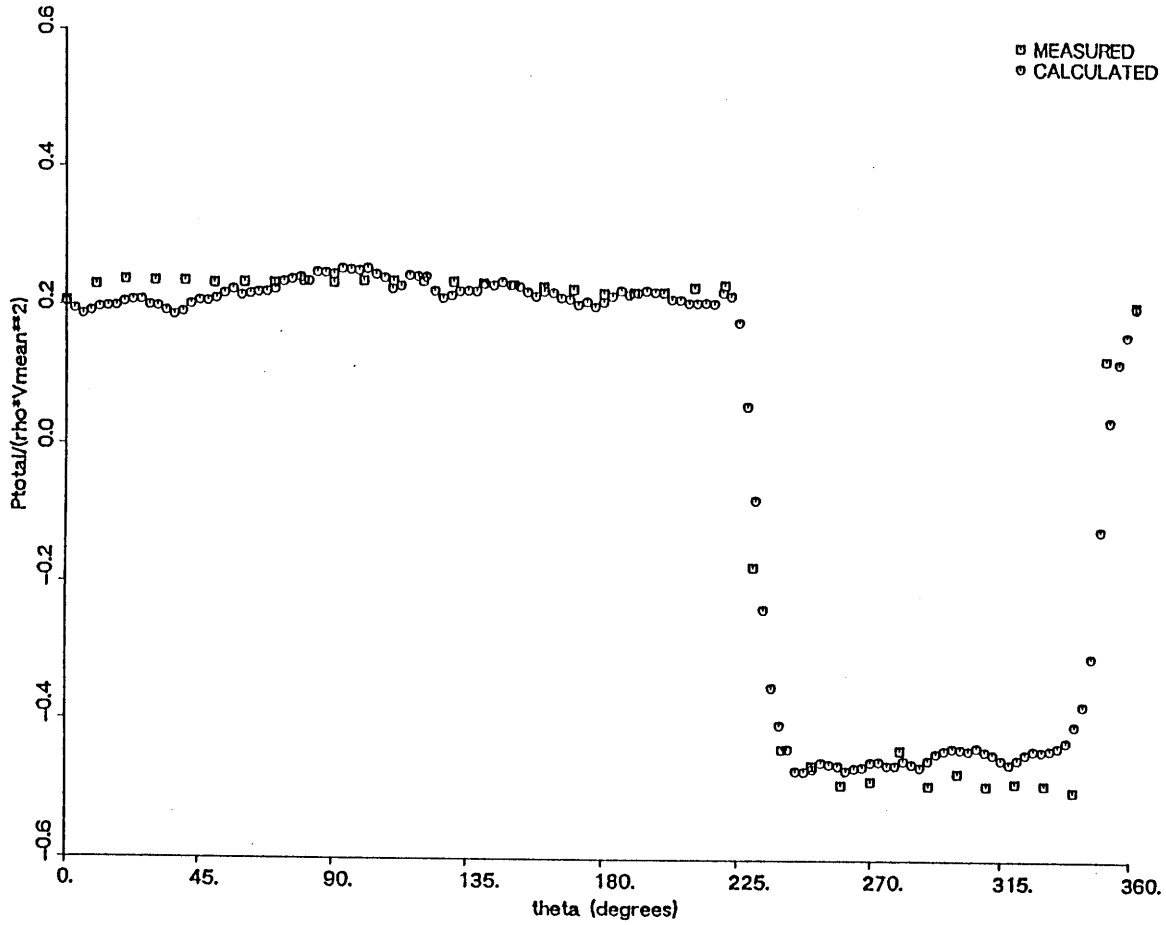

Figure B-3 Total Pressure Comparison: Post Test Kiel Probe Measurement Versus Static Probe and Cross Film Combination From Test, Heavy Distortion

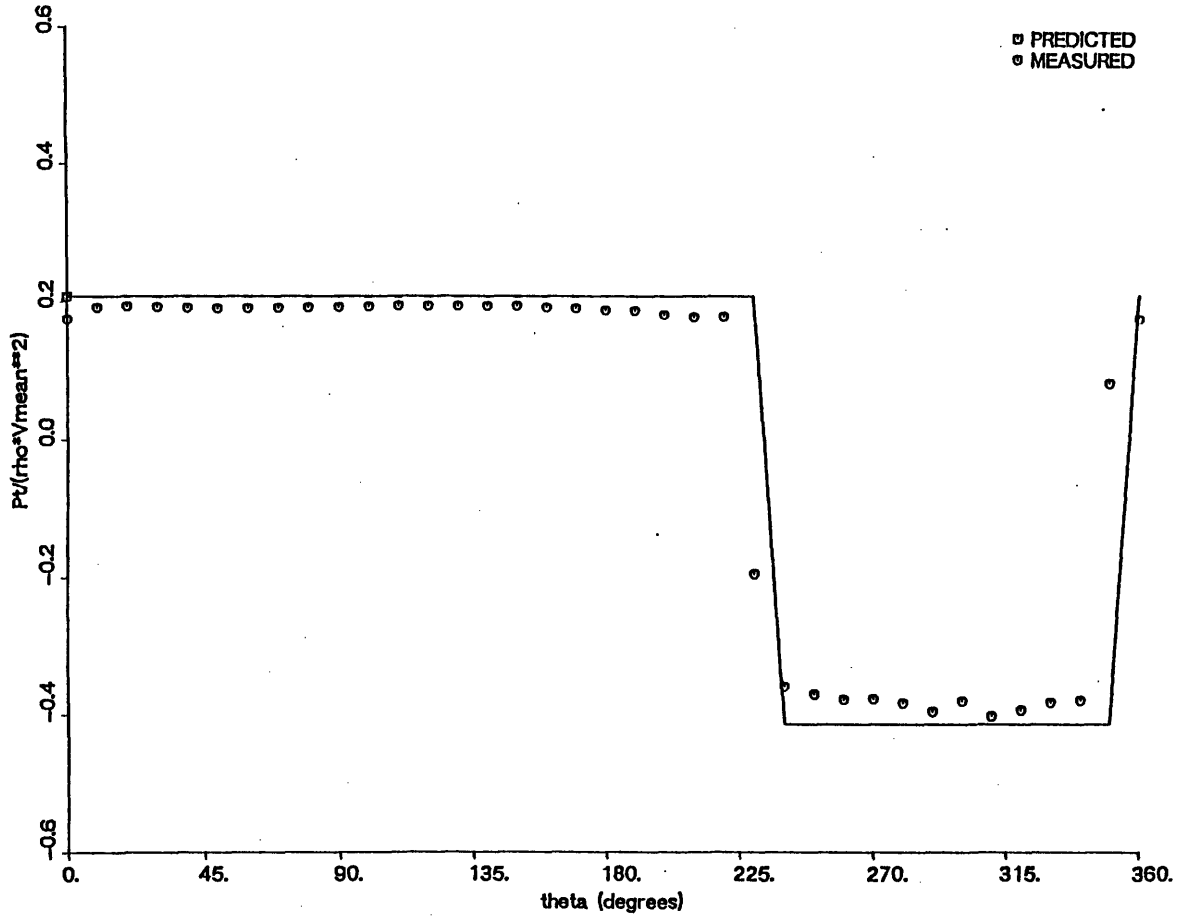

Figure B-4 Total Pressure Comparison: Post Test Kiel Probe Measurement Versus Distortion Screen Design Goal, Standard Distortion.

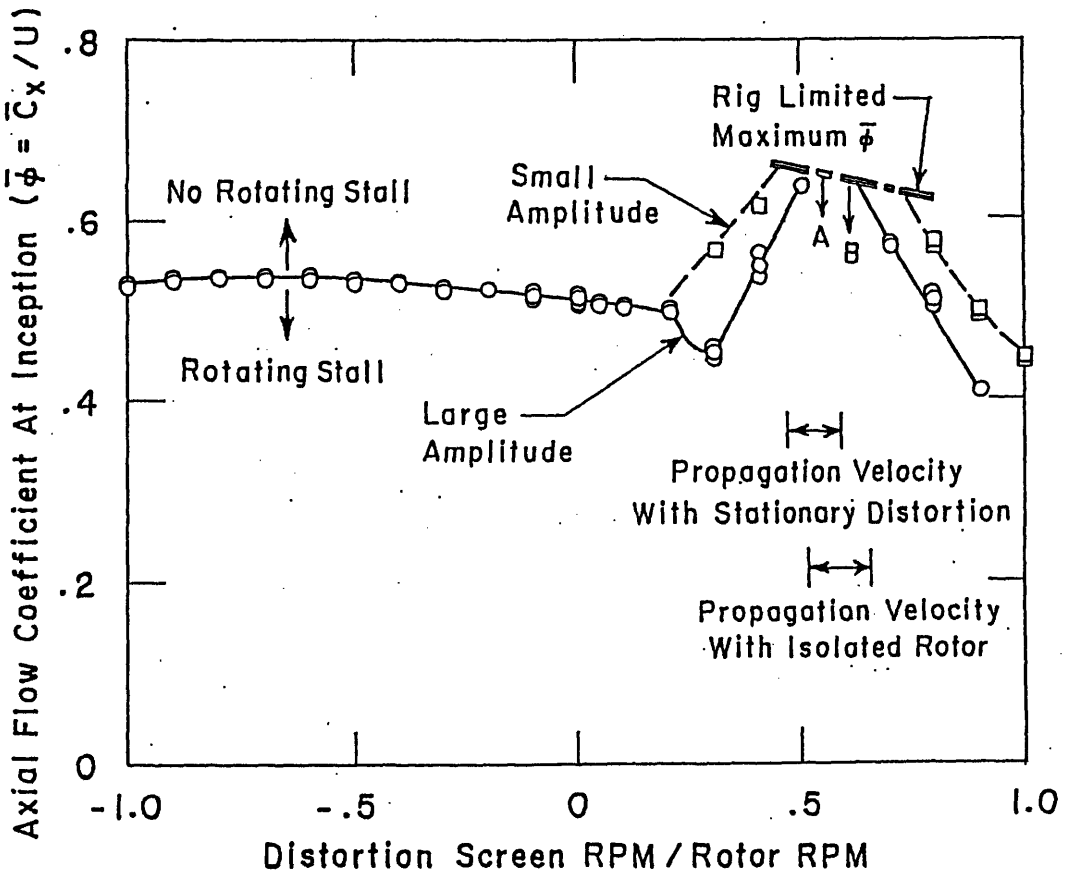

Figure 1-1 Measured Effect of Rotating Distortion on Compressor Stability, (Reference 1)

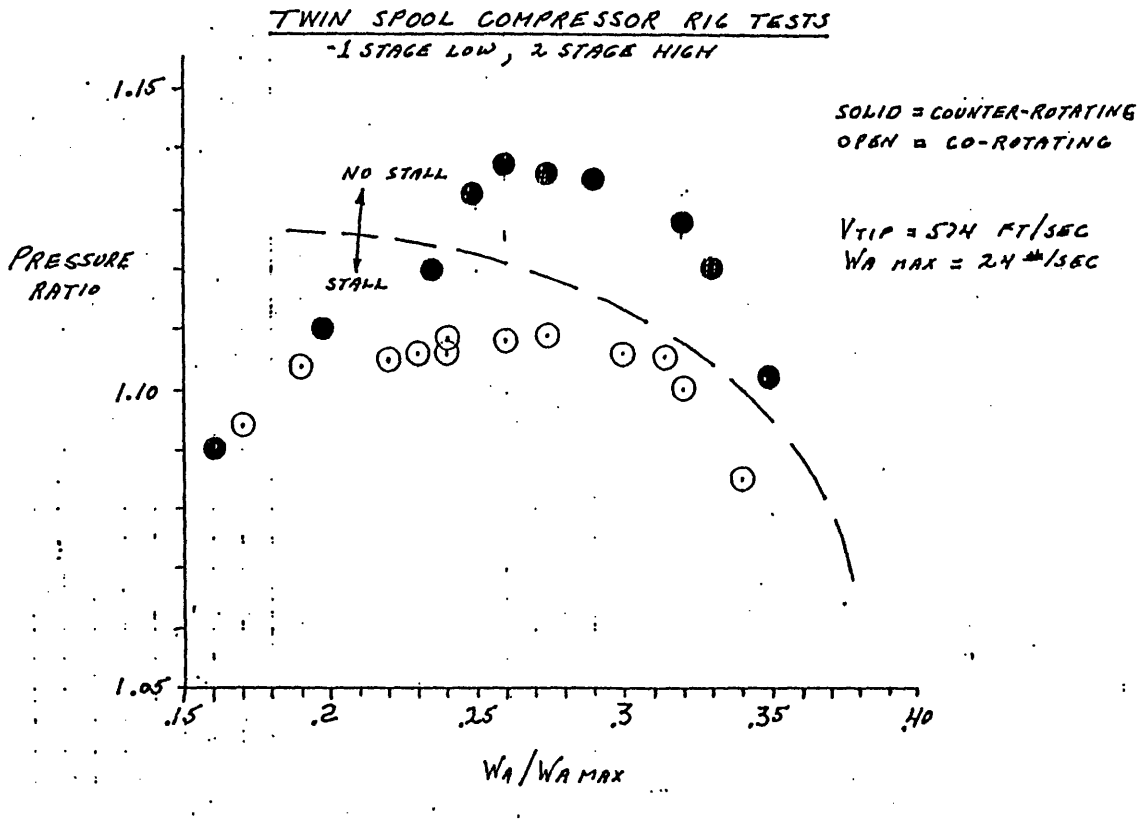

Figure 1-2 Measured Effect of Rotating Distortion on Performance, (Reference 2)

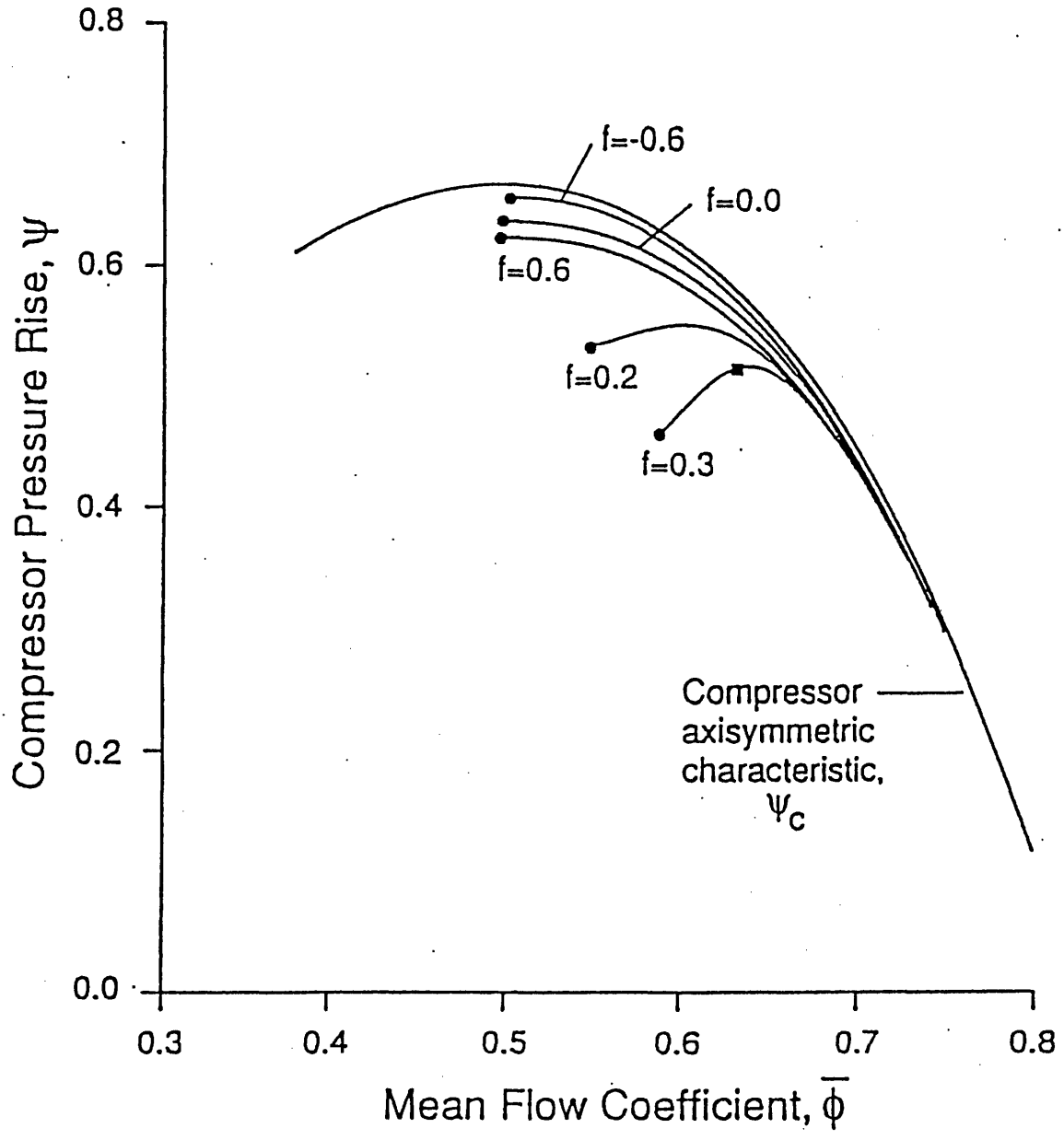

Figure 1-3 Calculated Effect of Rotating Distortion on Performance (Reference 3)

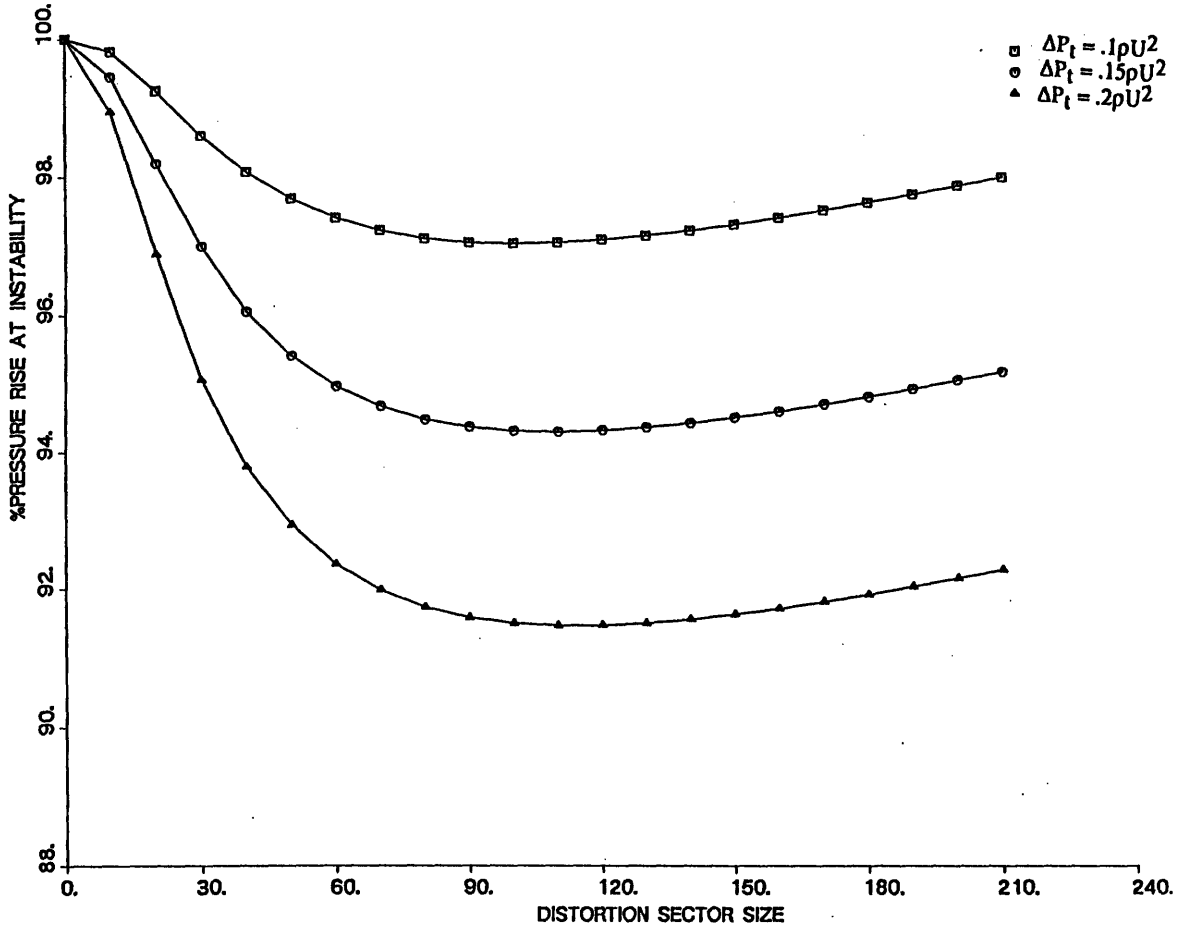

Figure 3-1 Effect of Circumferential Extent on Percent Pressure Rise at Neutral Stability

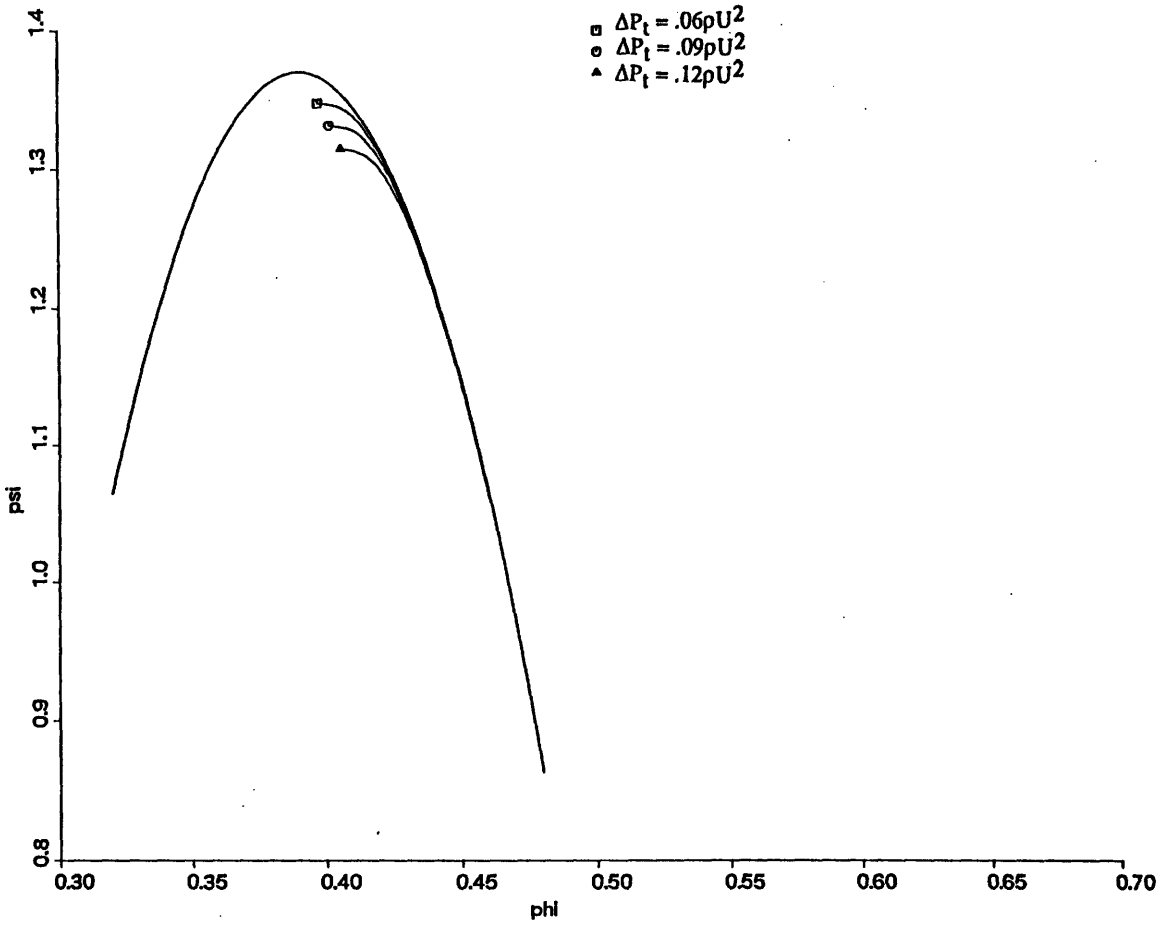

Figure 3-2 Effect of Distortion Magnitude on Distorted Compressor Performance. Stationary 120 Degree Total Pressure Distortion

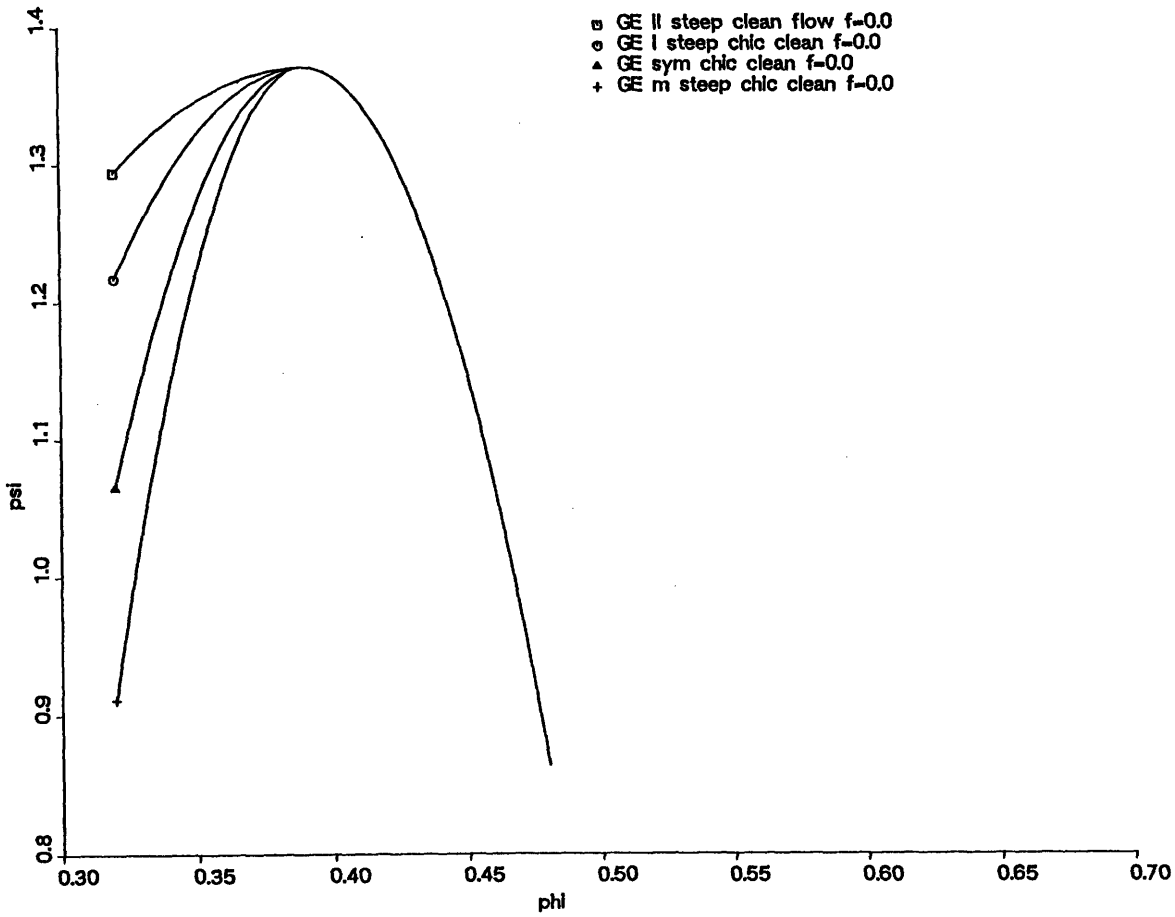

Figure 3-3 Variable Undistorted Flow Characteristics for Pre-test Calculations

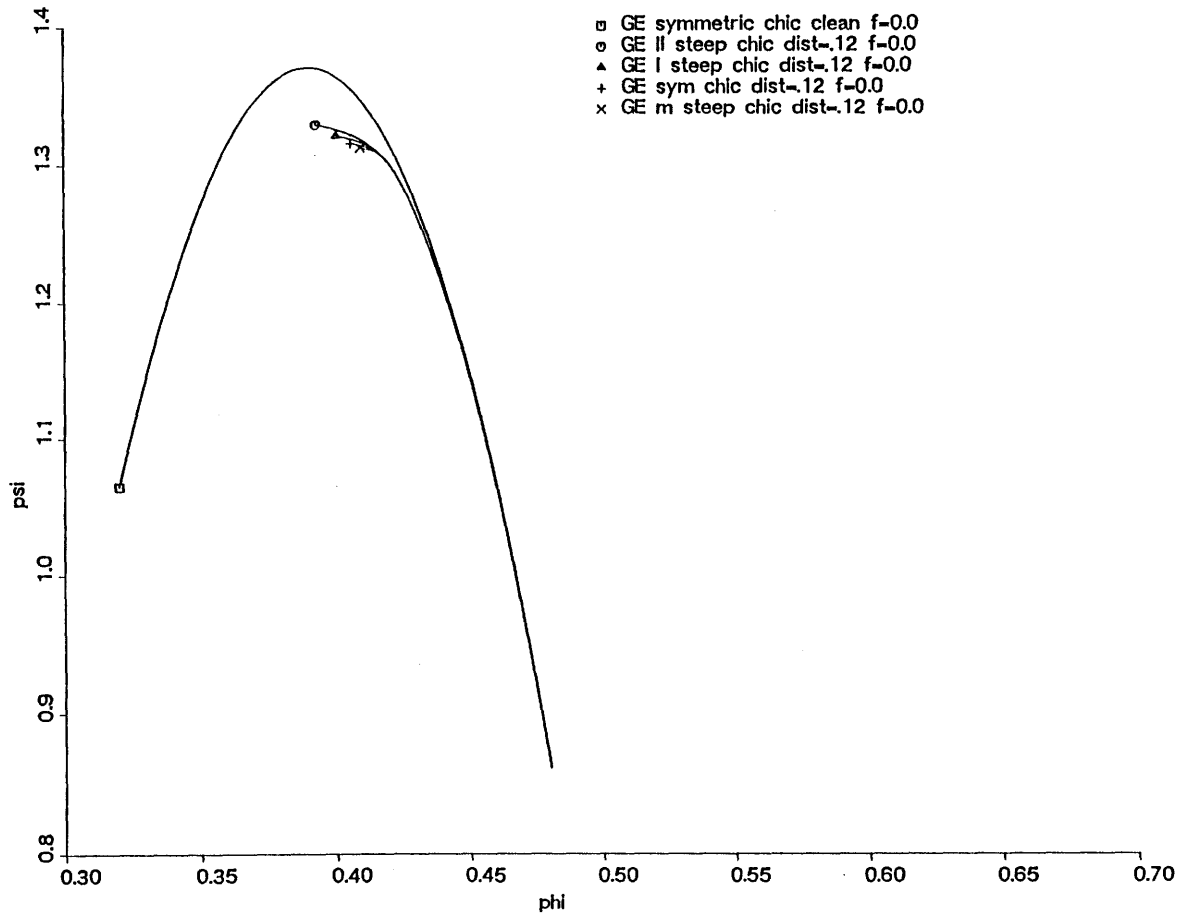

Figure 3-4 Effect of Low Flow Side of Undistorted Flow Characteristic on Compressor Performance. f=0.0 Distortion Magnitude = 0.12

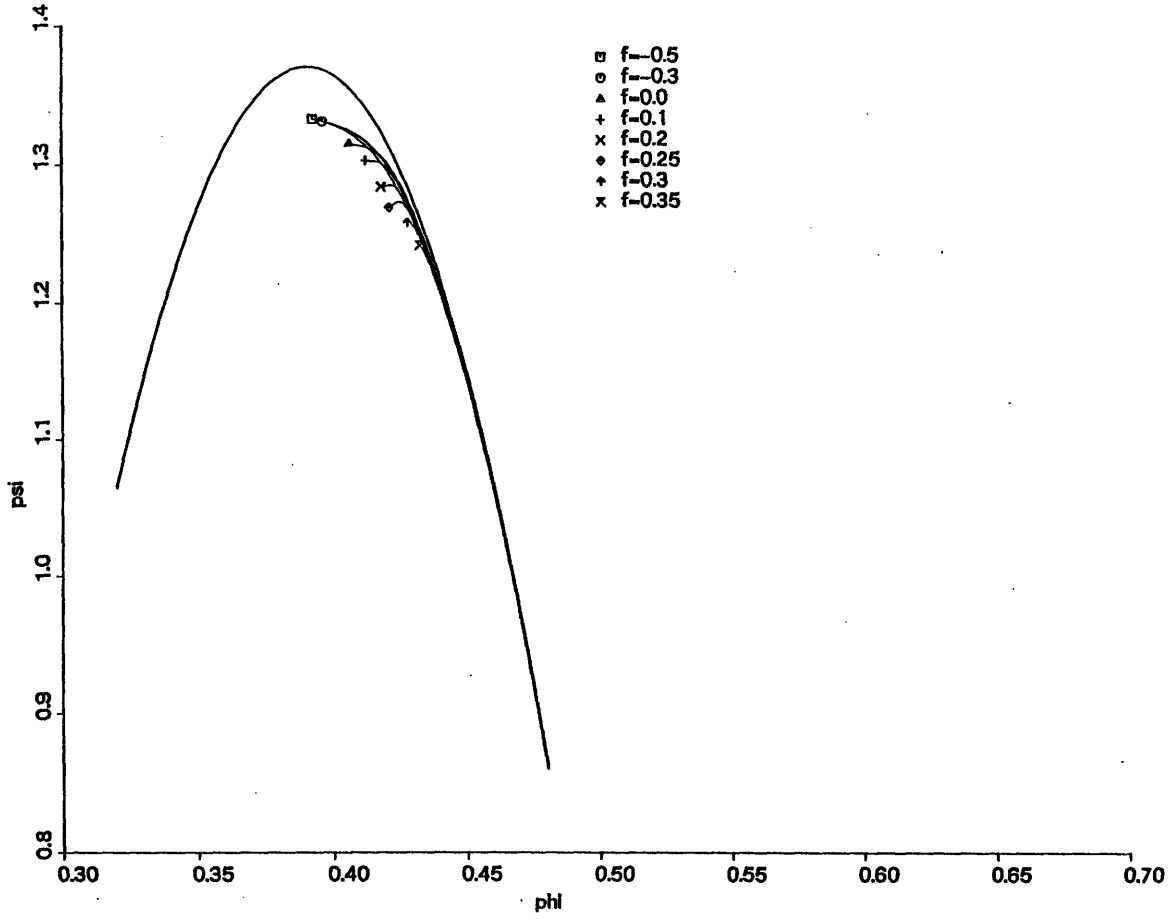

Figure 3-5 Effect of Distortion Rotation Rate on Compressor Performance.

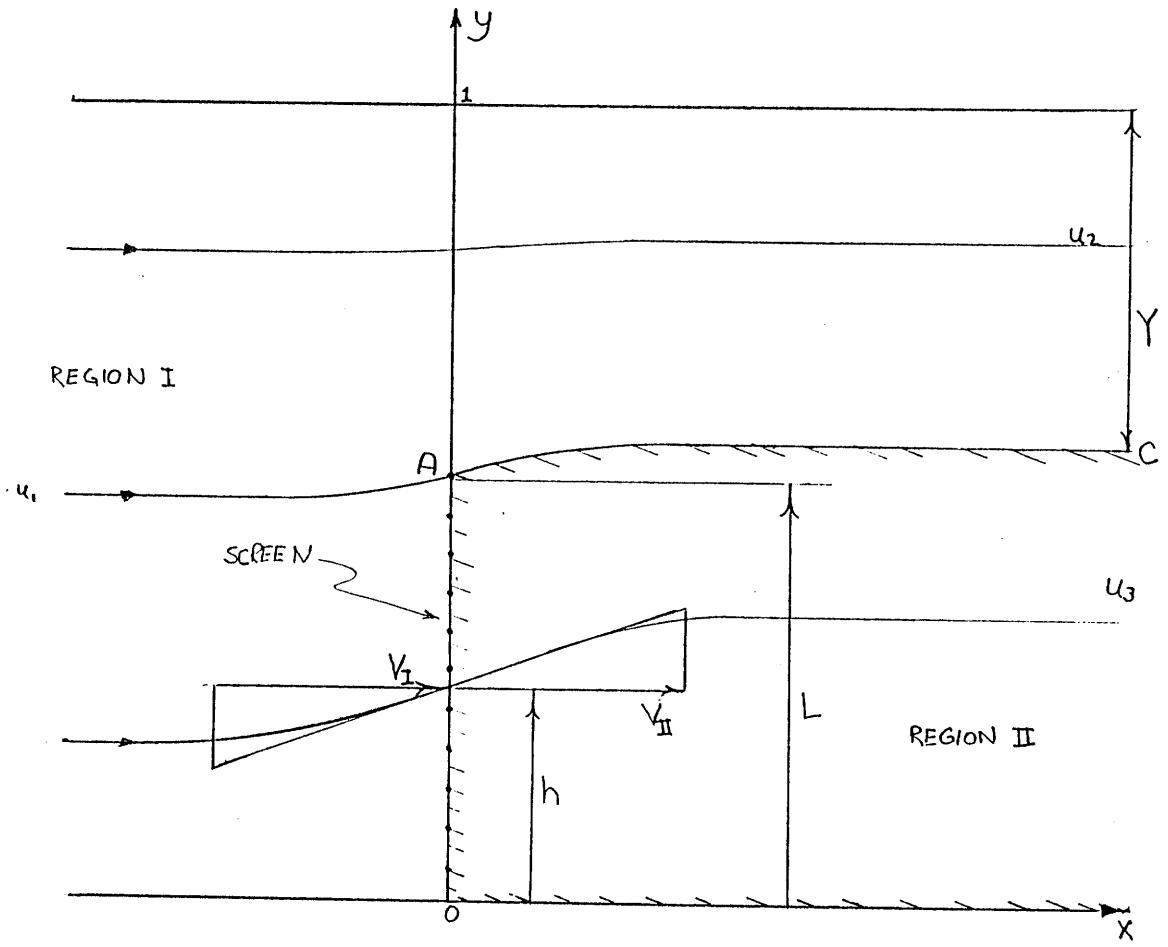

Figure 3-6 Diagram of Screen and Channel, Defines Variables Used in the Analysis

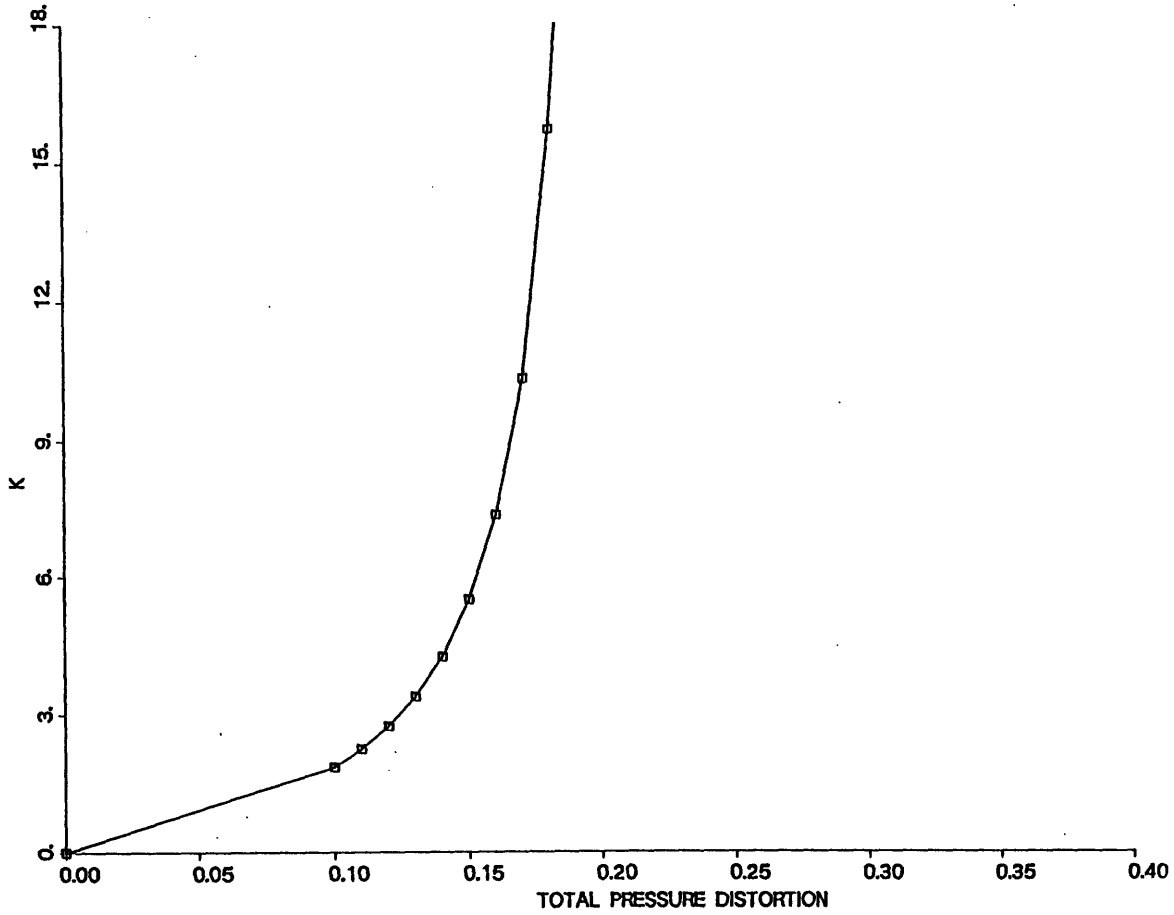

Figure 3-7 Effect of Desired Distortion Magnitude on Required Circumferential Extent of Screen for 120 Degree Downstream Distorted Sector.

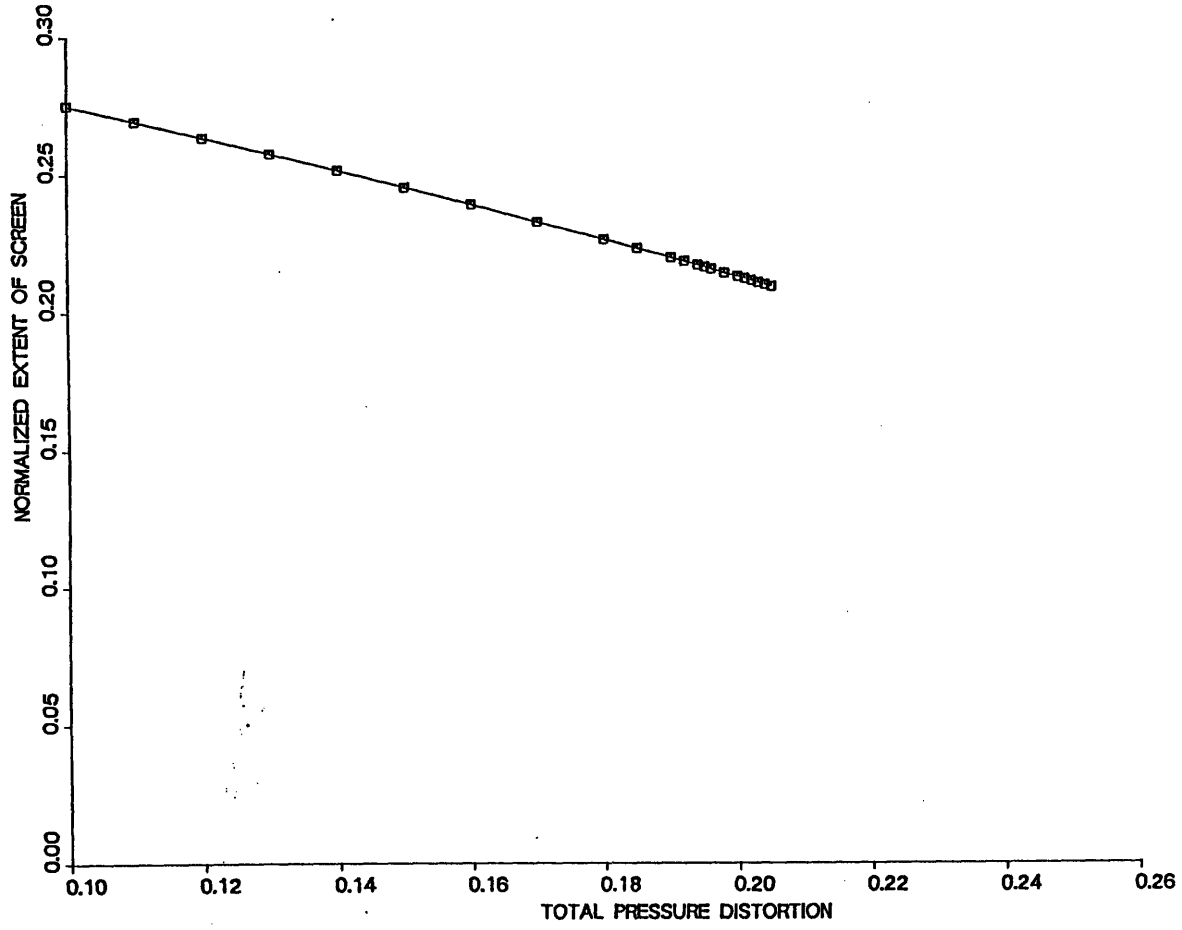

Figure 3-8 Effect of Desired Distortion Magnitude on Required Screen Loss Coefficient for 120 Degree Downstream Distorted Sector

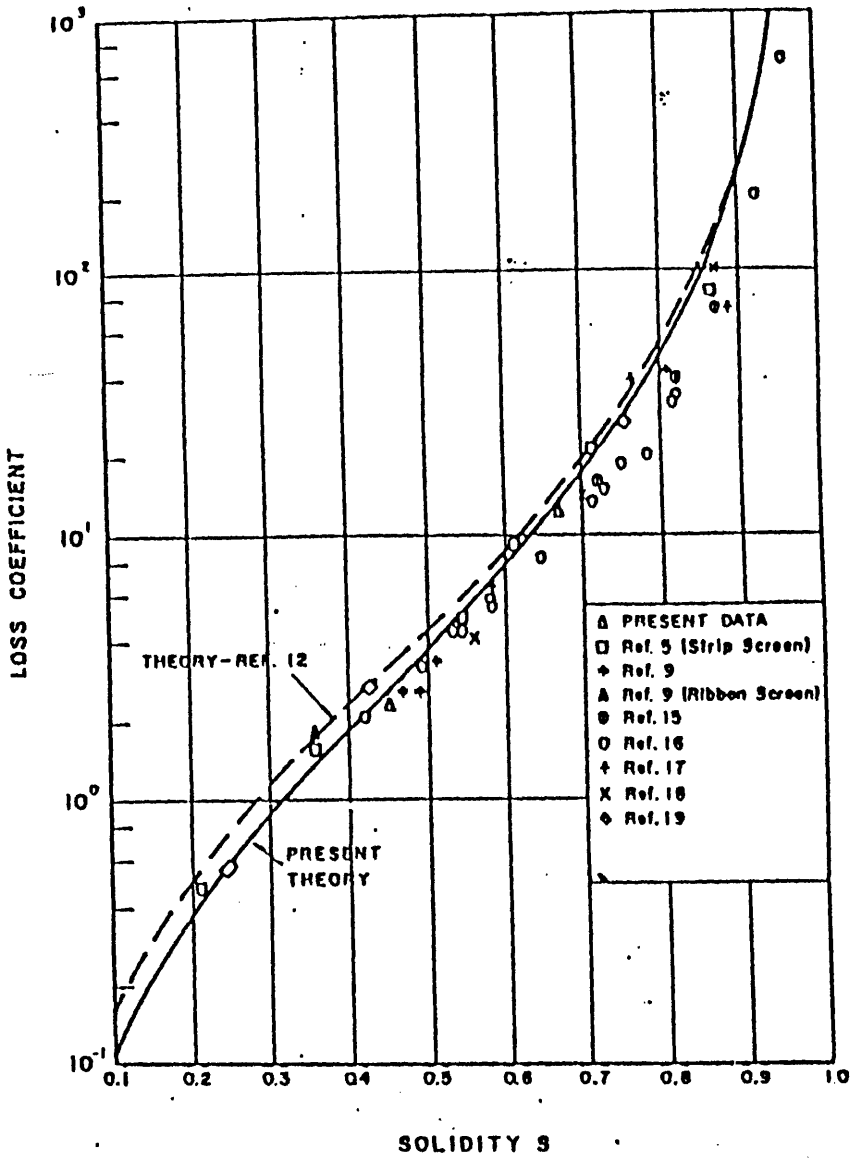

Figure 3-9 Effect of Perforated Plate Solidity on Loss Coefficient, (Reference 12)

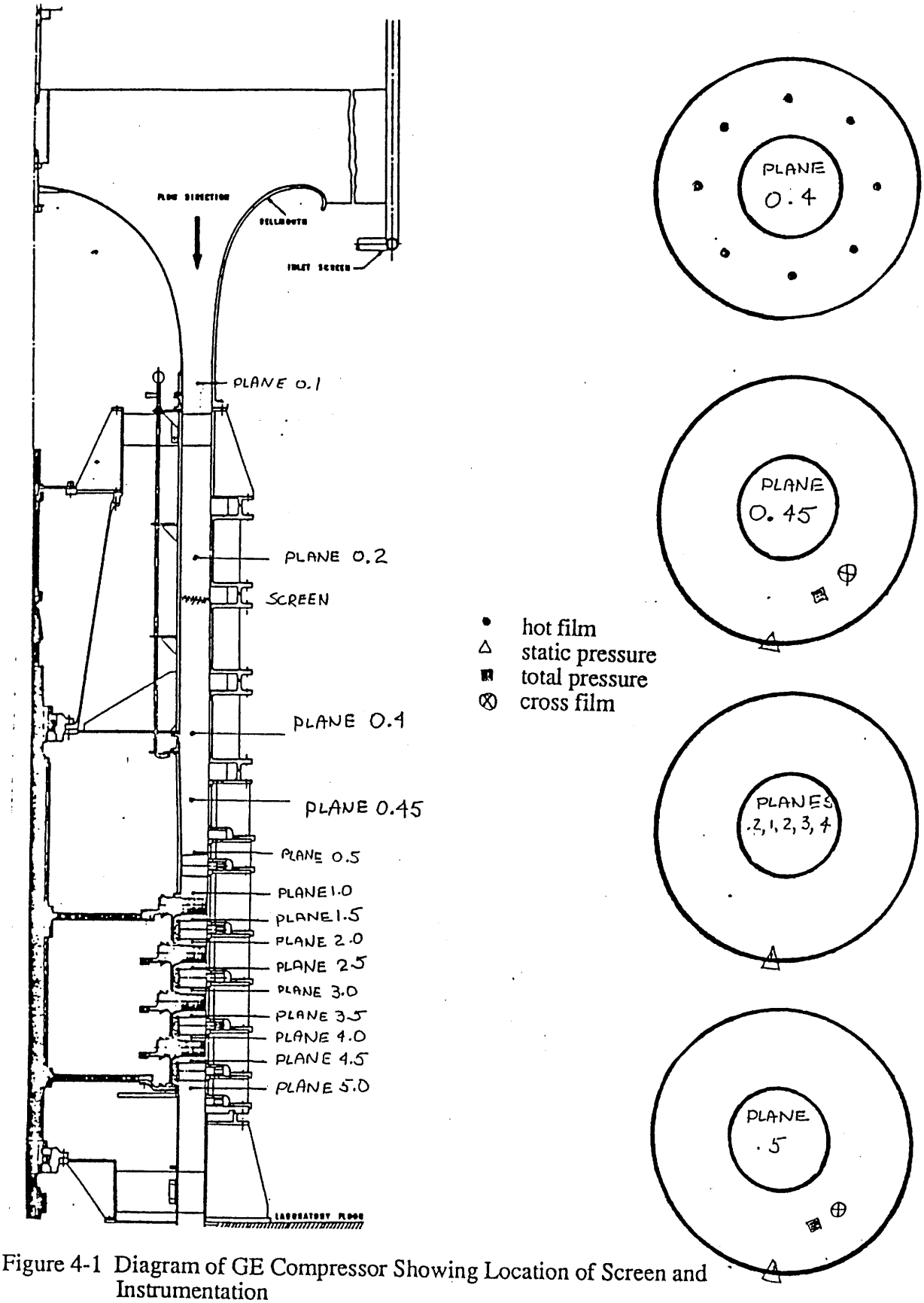

Figure 4-1 Diagram of GE Compressor Showing Location of Screen and Instrumentation

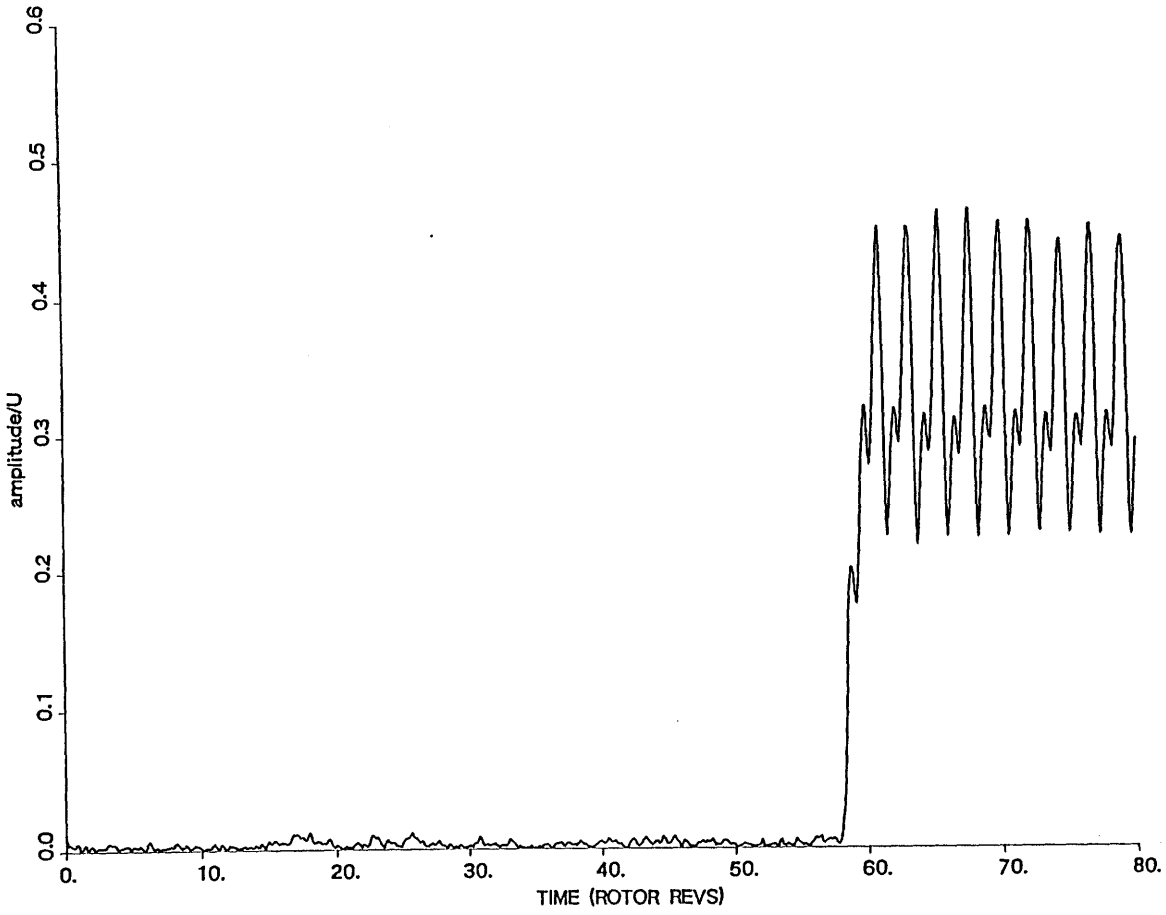

Figure 5-1 Growth of Amplitude of First Circumferential Harmonic, Undistorted Flow (Probe sensitivity differences are causing oscillation. In stall, actual amplitude is constant.)

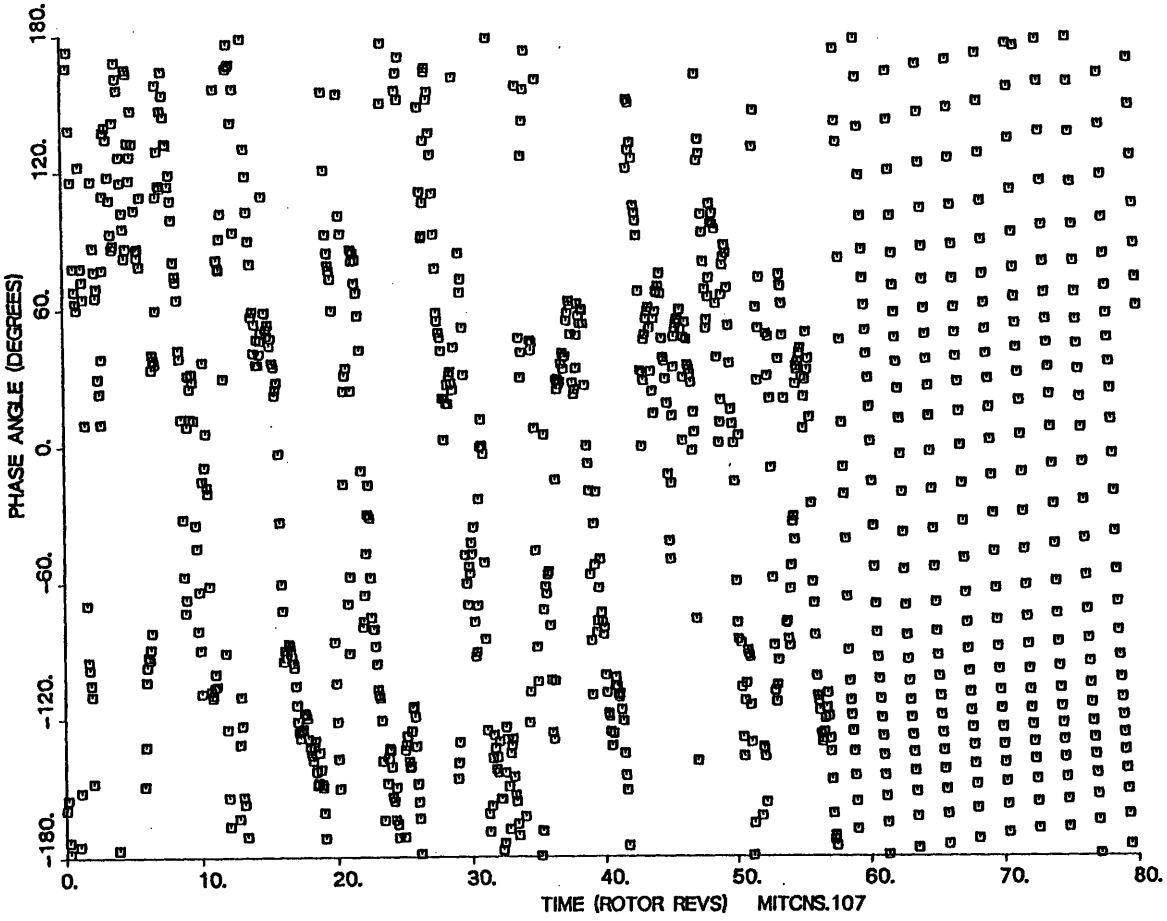

Figure 5-2 Change in Phase of First Circumferential Harmonic, Undistorted Flow.

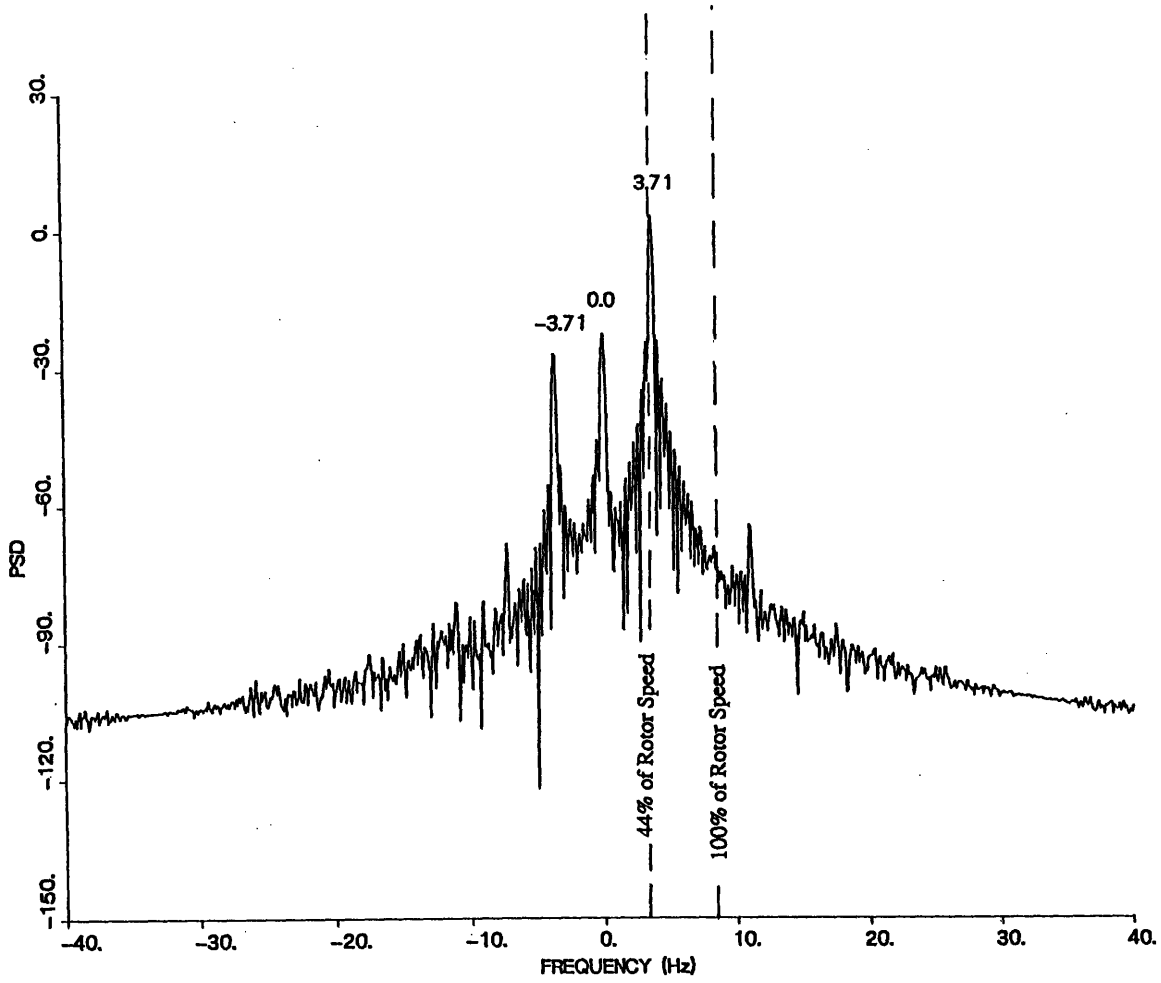

Figure 5-3 Power Spectral Density for First 85 Compressor Revolutions

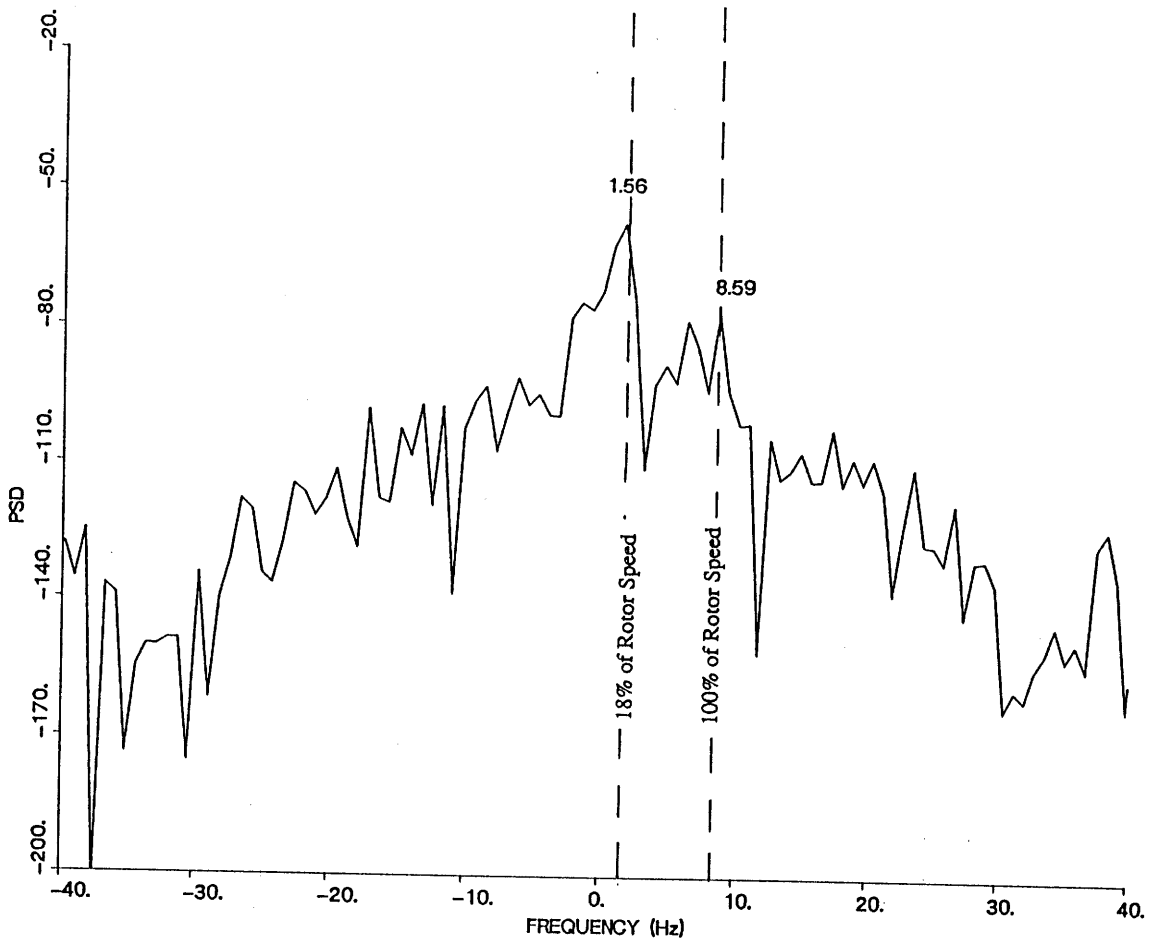

Figure 5-4 Power spectral Density for Range of 10.5 to 21 Compressor Revolutions.

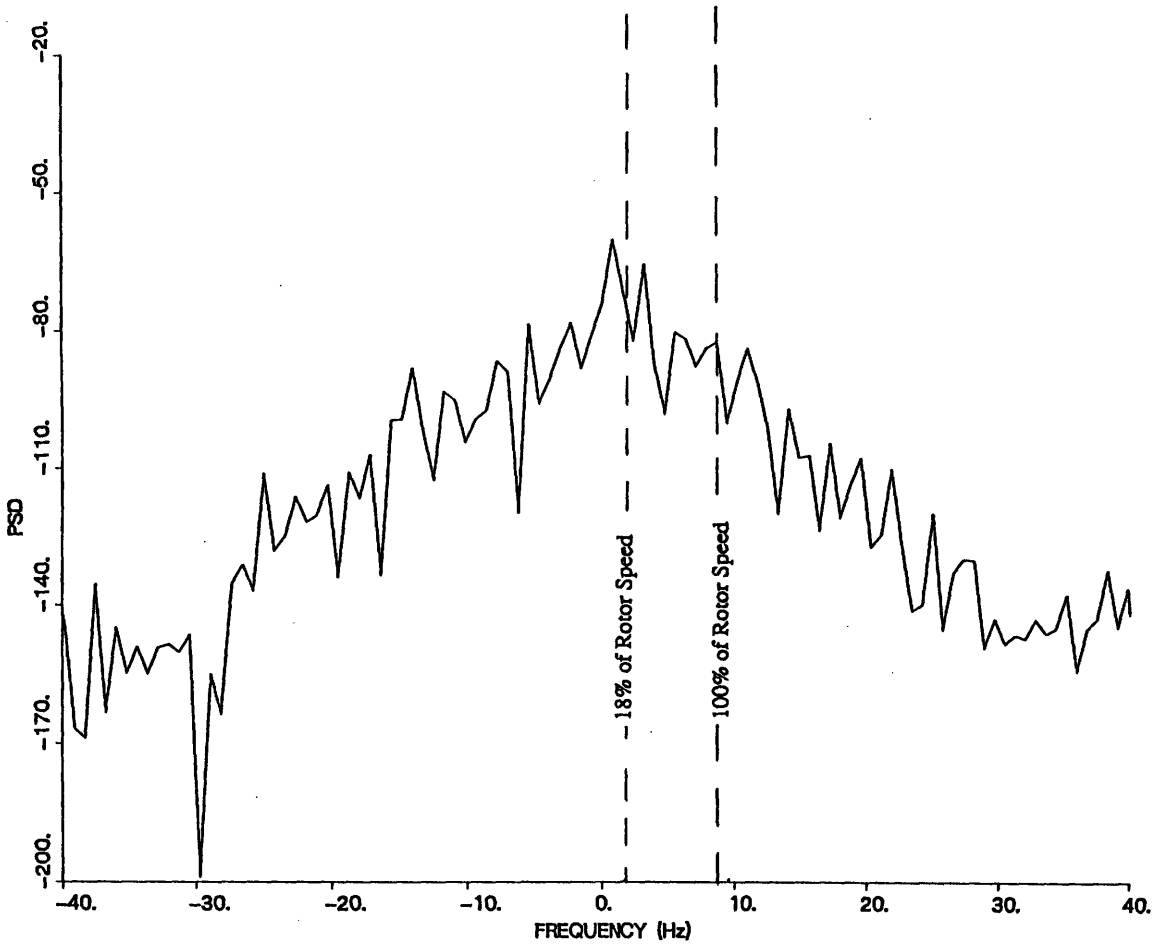

Figure 5-5 Power spectral Density for Range of 21 to 31.5 Compressor Revolutions.

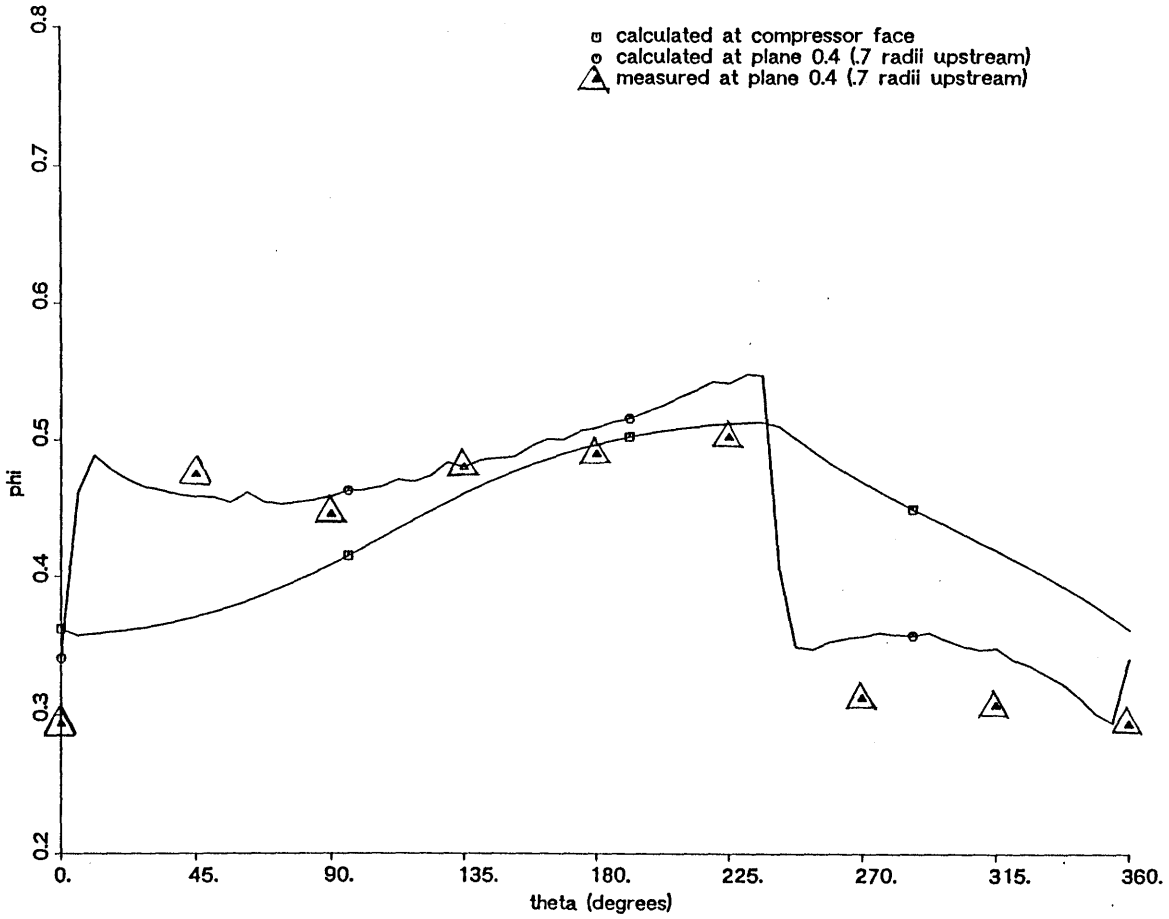

Figure 5-6 Phase Relationship for Calculated and Measured Velocity Profiles Used in Cross Correlation. Stationary Distortion

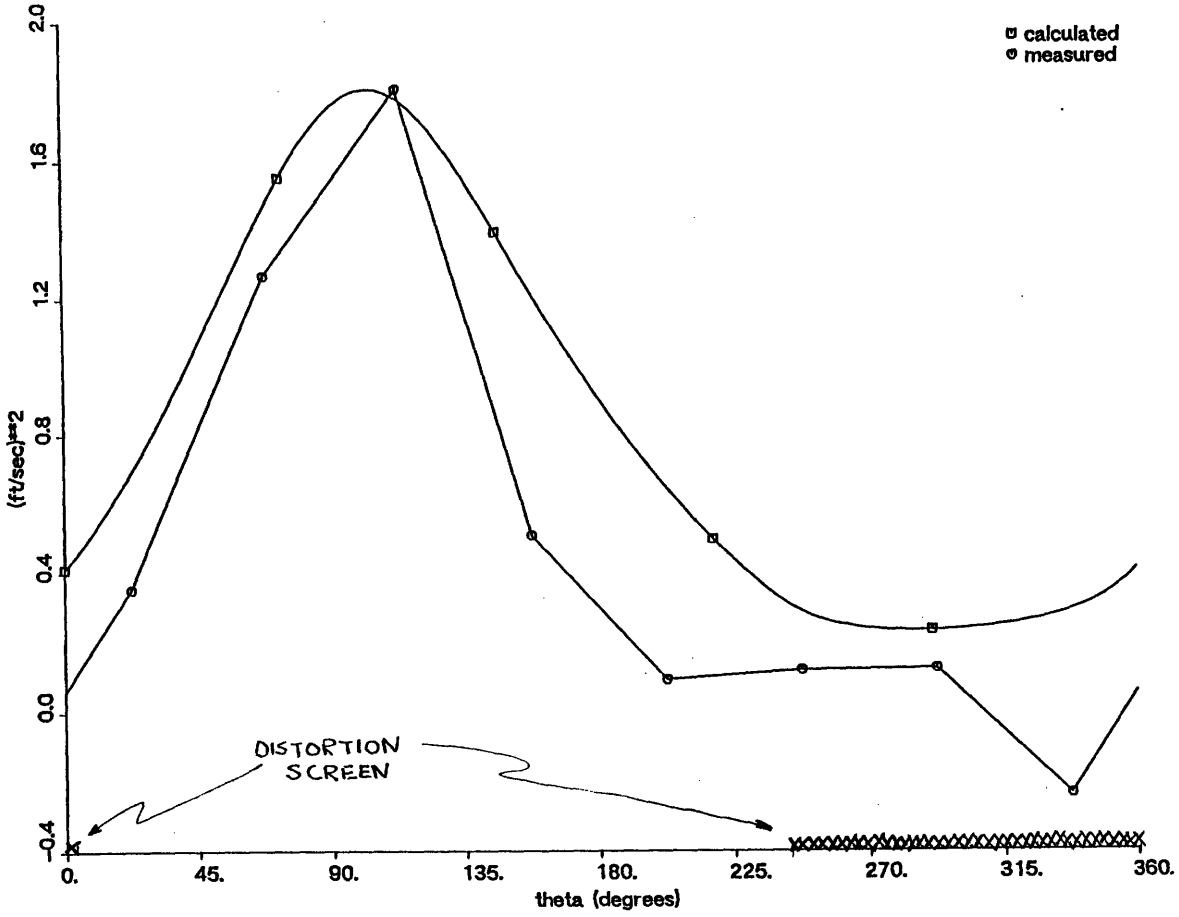

Figure 5-7 Calculated Square of Unsteadiness and Maximum Measured Cross Correlation for Stationary Distortion Near Stall

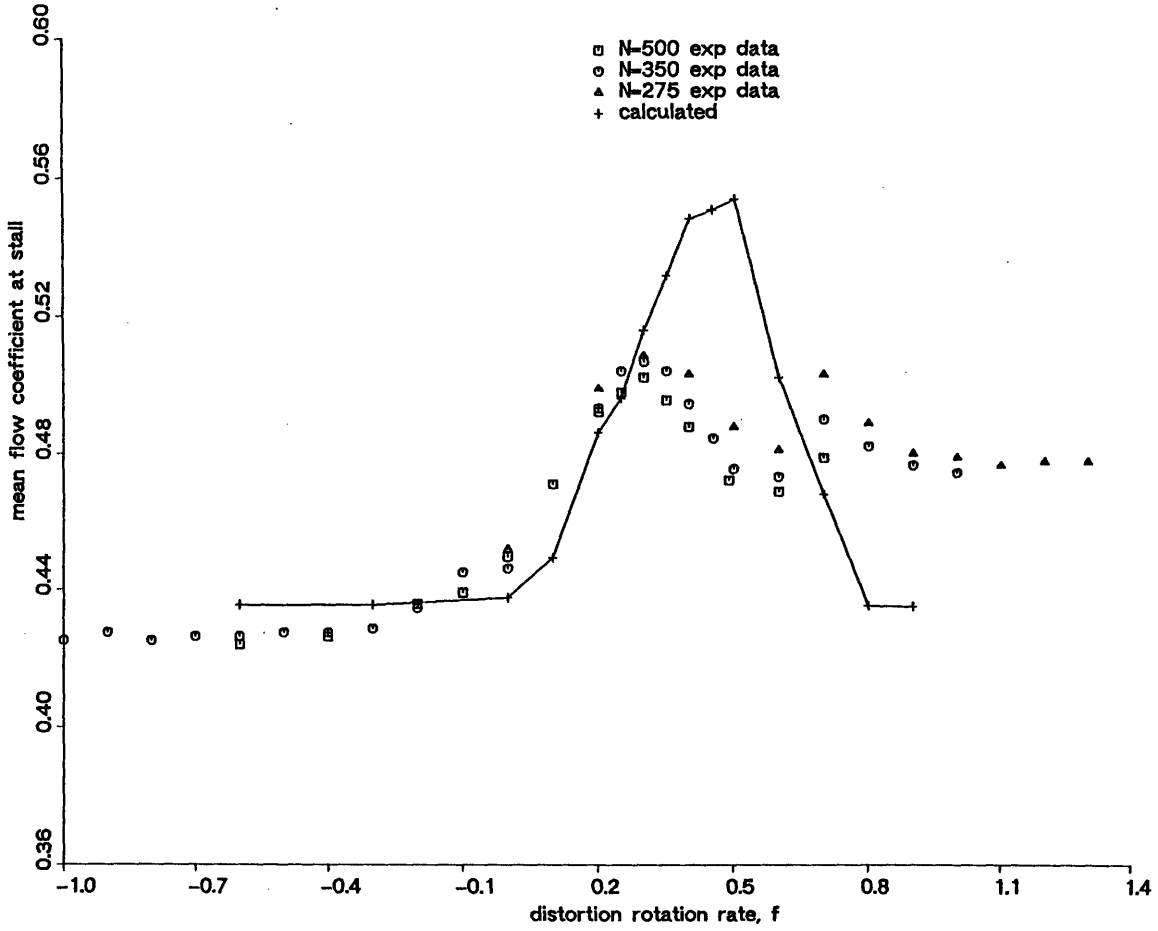

Figure 5-8 Calculated and Experimental Neutral Stability Flow Coefficients for Standard Distortion

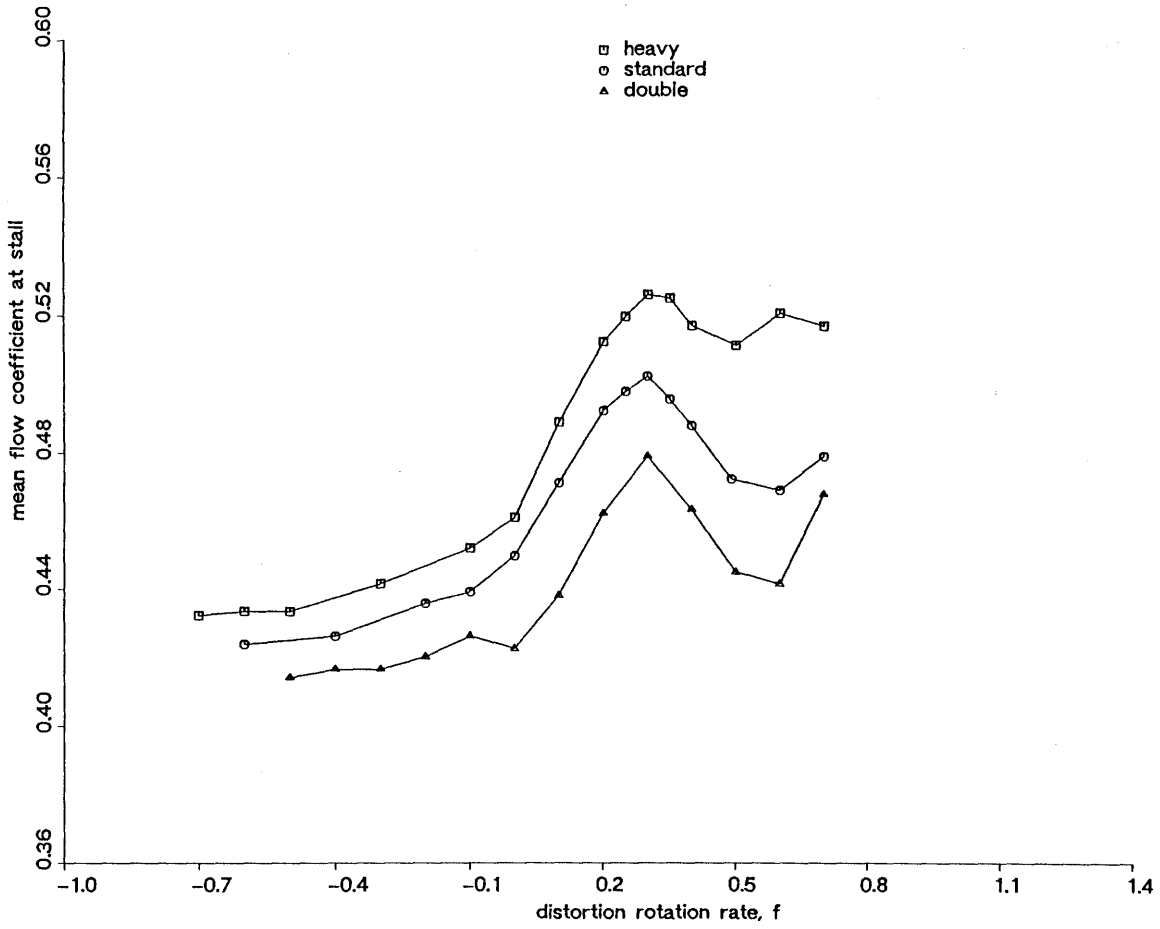

Figure 5-9 Experimental Neutral Stability Flow Coefficients for Three Distortion Magnitudes. Compressor at 500 rpm.

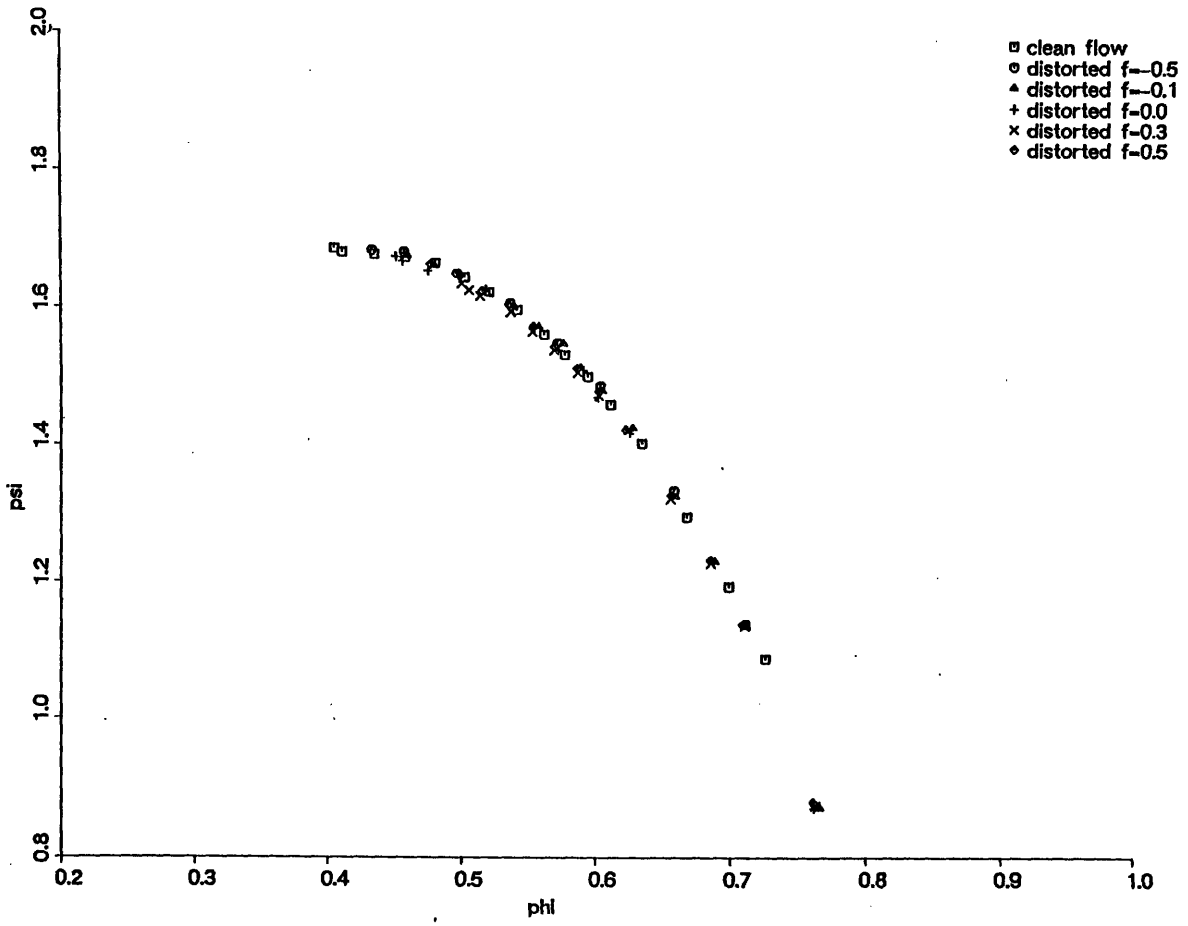

Figure 5-10 Compressor Characteristics for Undistorted Flow and Distorted Flow at Several Rotation Speeds. Static to Static Pressure Rise.

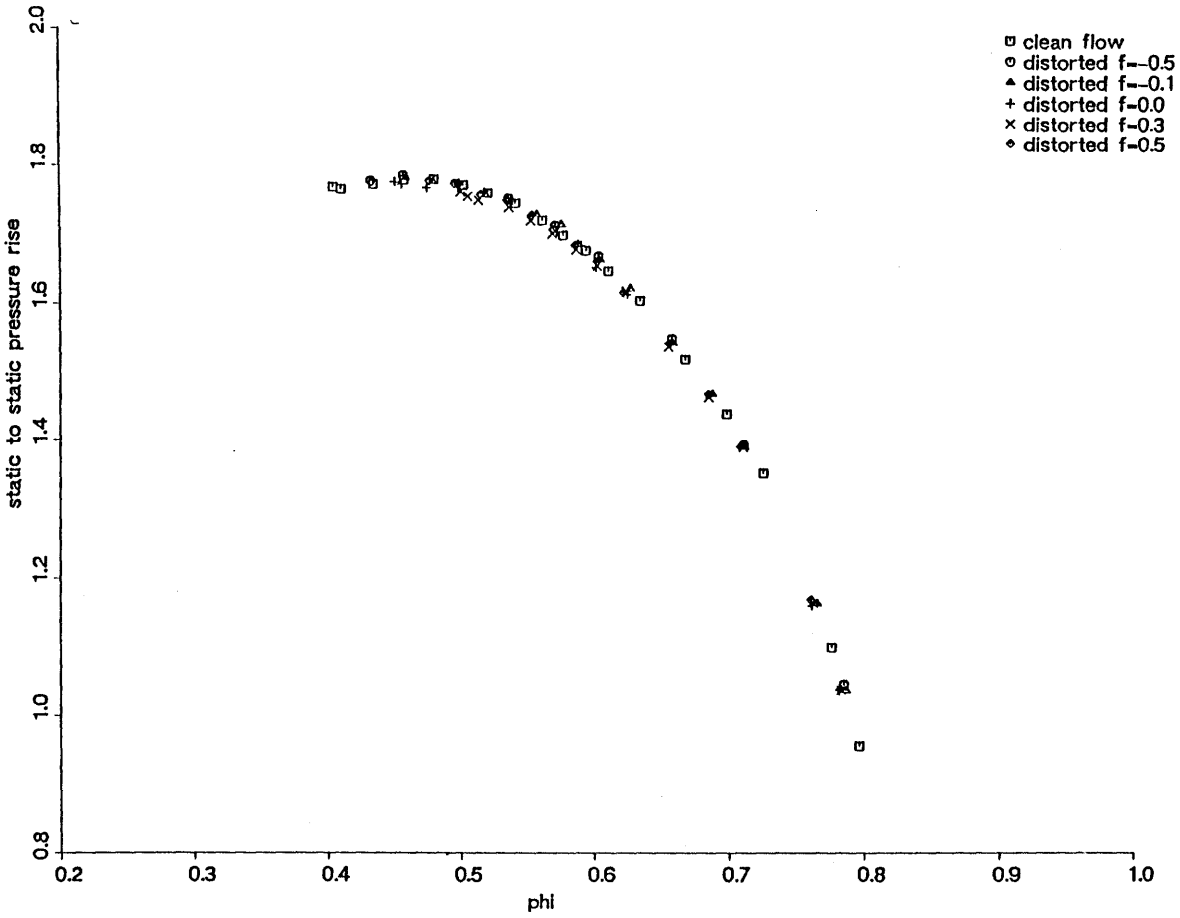

Figure 5-11 Compressor Characteristics for Undistorted Flow and Distorted Flow at Several Rotation Speeds. Total to Static Pressure Rise.

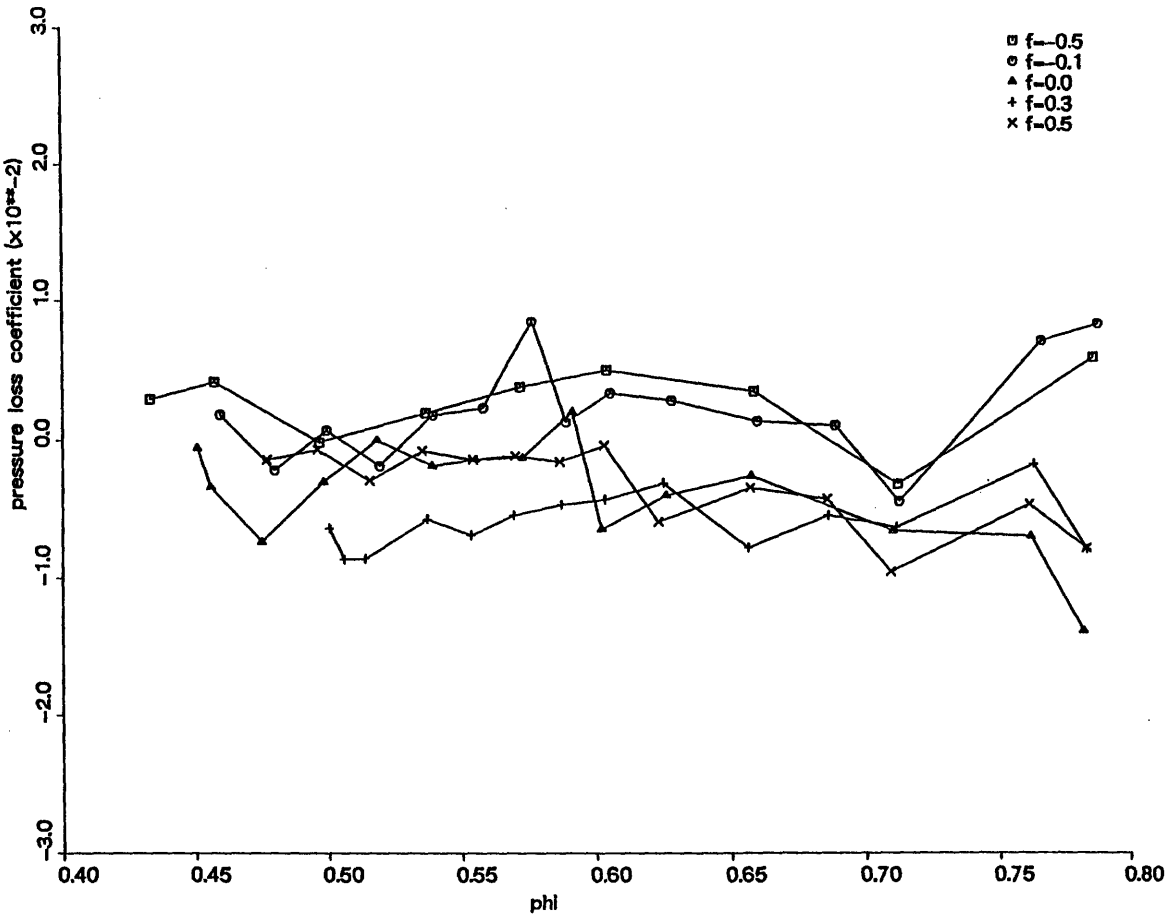

Figure 5-12 Effect of Distortion Rotation Rate on Pressure Loss Coefficient.

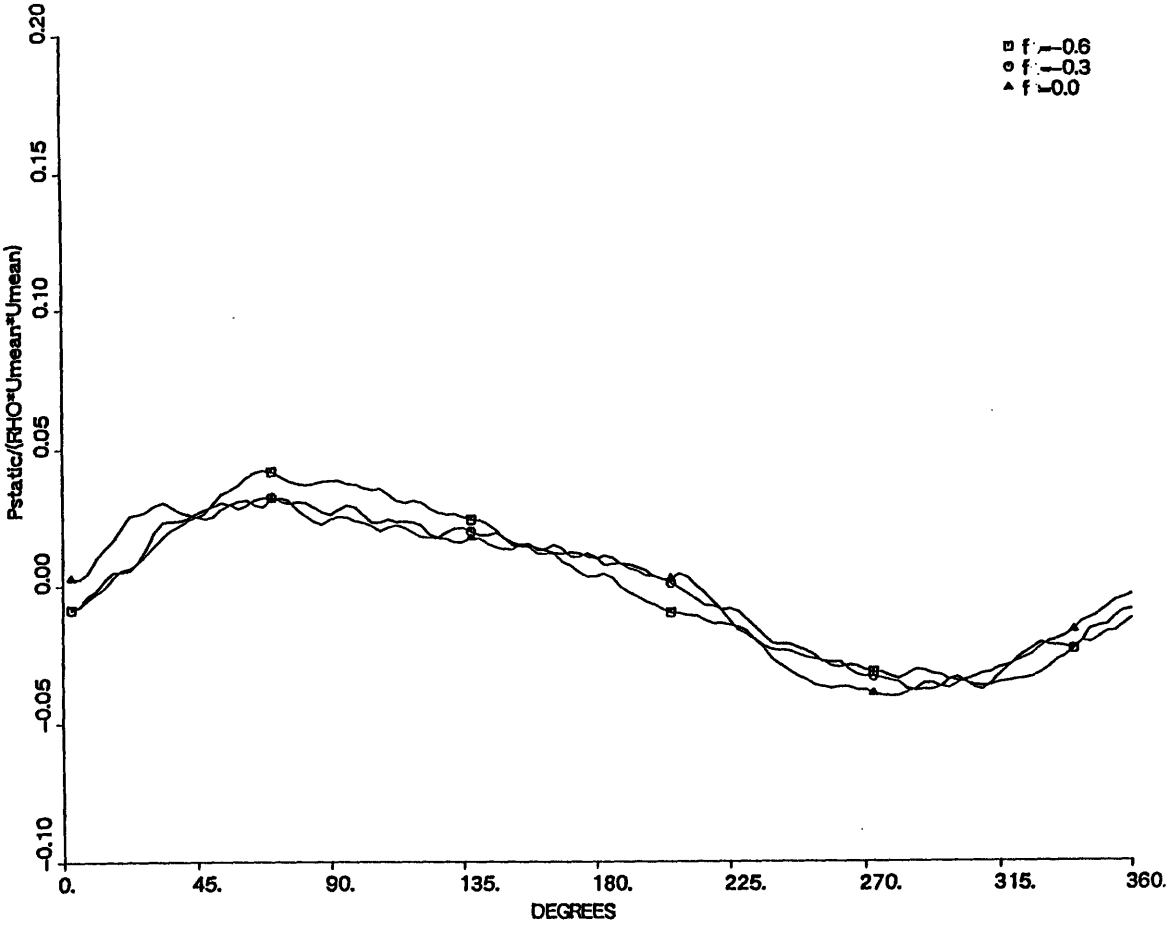

Figure 5-13 Static Pressure Profiles at Plane 0.45 (.32 radii upstream of IGV's) for Negative Rotation Rates, Compressor Operating Near Stall

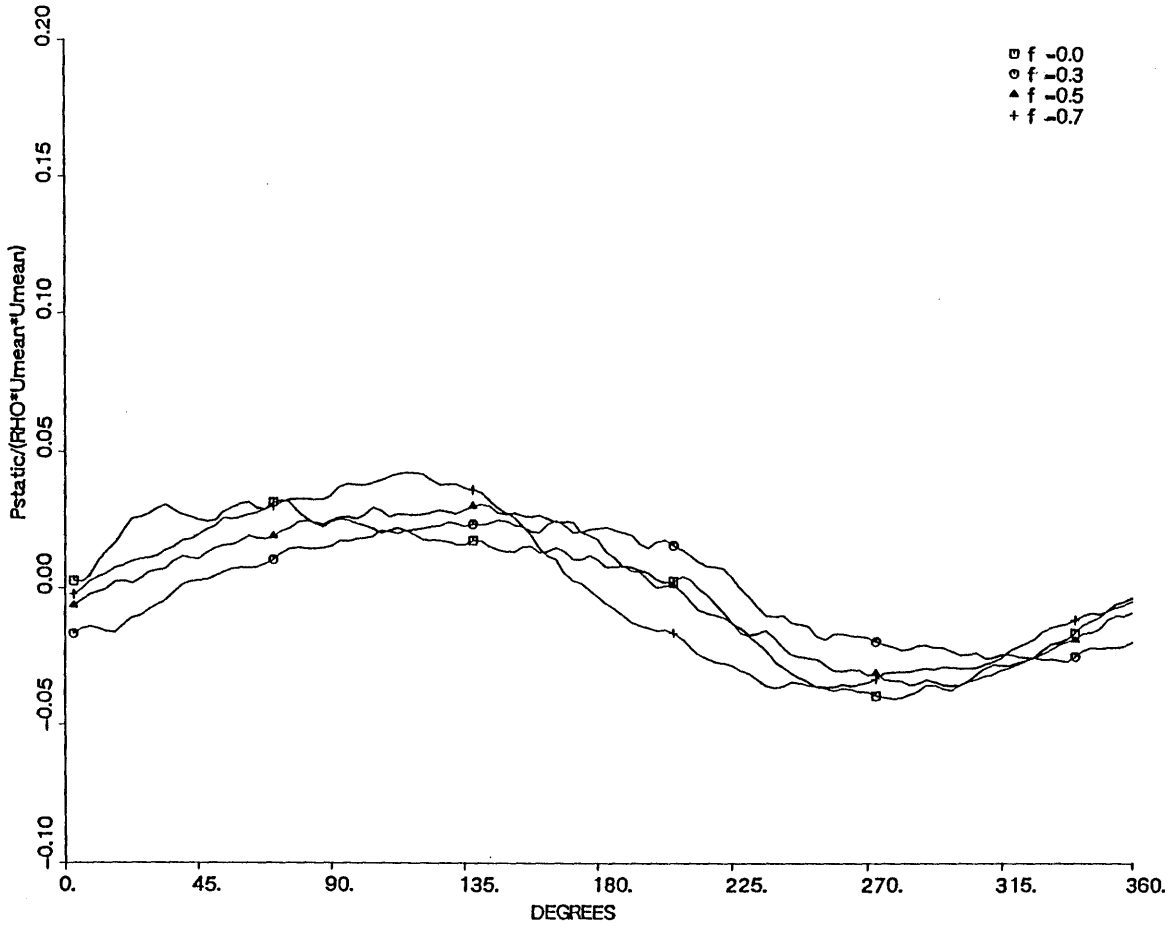

Figure 5-14 Static Pressure Profiles at Plane 0.45 (.32 radii upstream of IGV's) for Positive Rotation Rates, Compressor Operating Near Stall

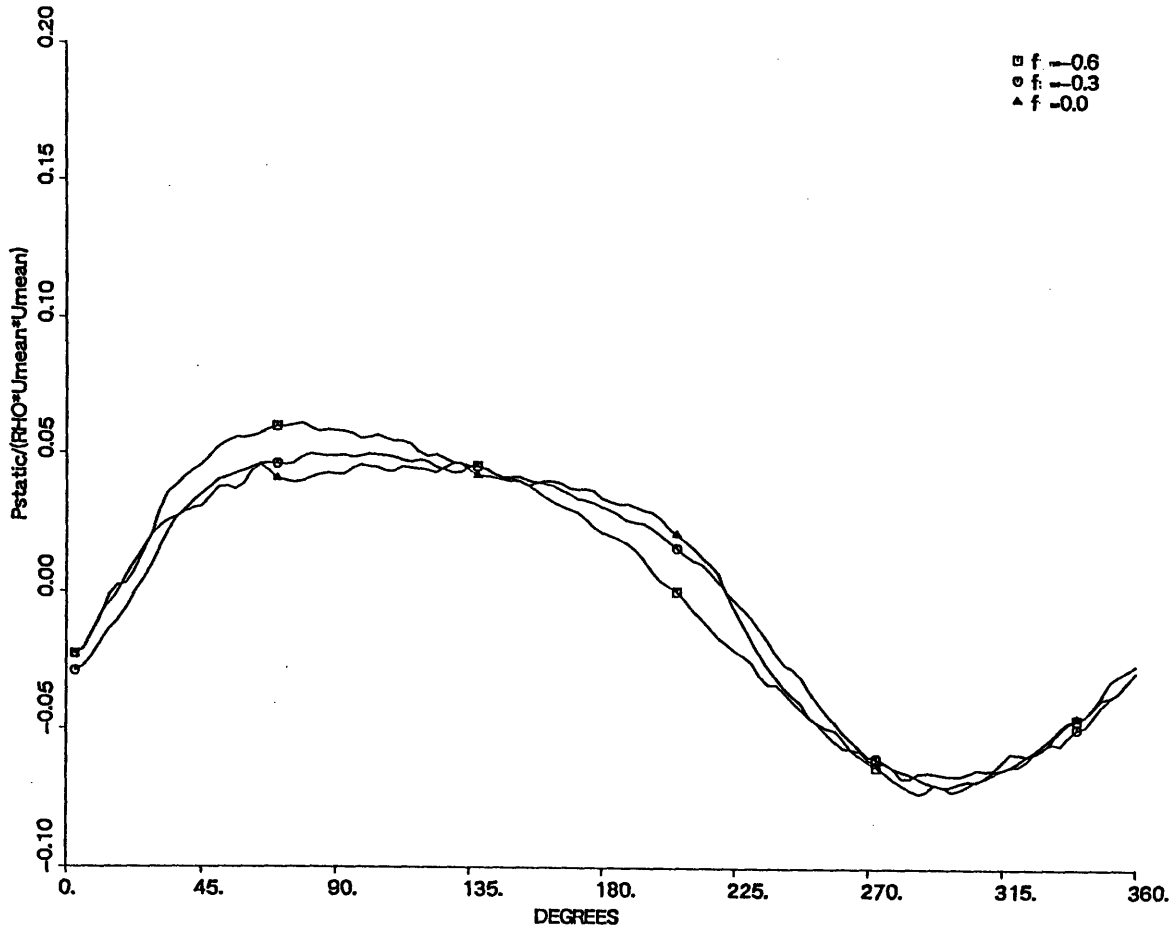

Figure 5-15 Static Pressure Profiles at Plane 0.45 (.32 radii upstream of IGV's) for Negative Rotation Rates, Compressor Operating Near Design

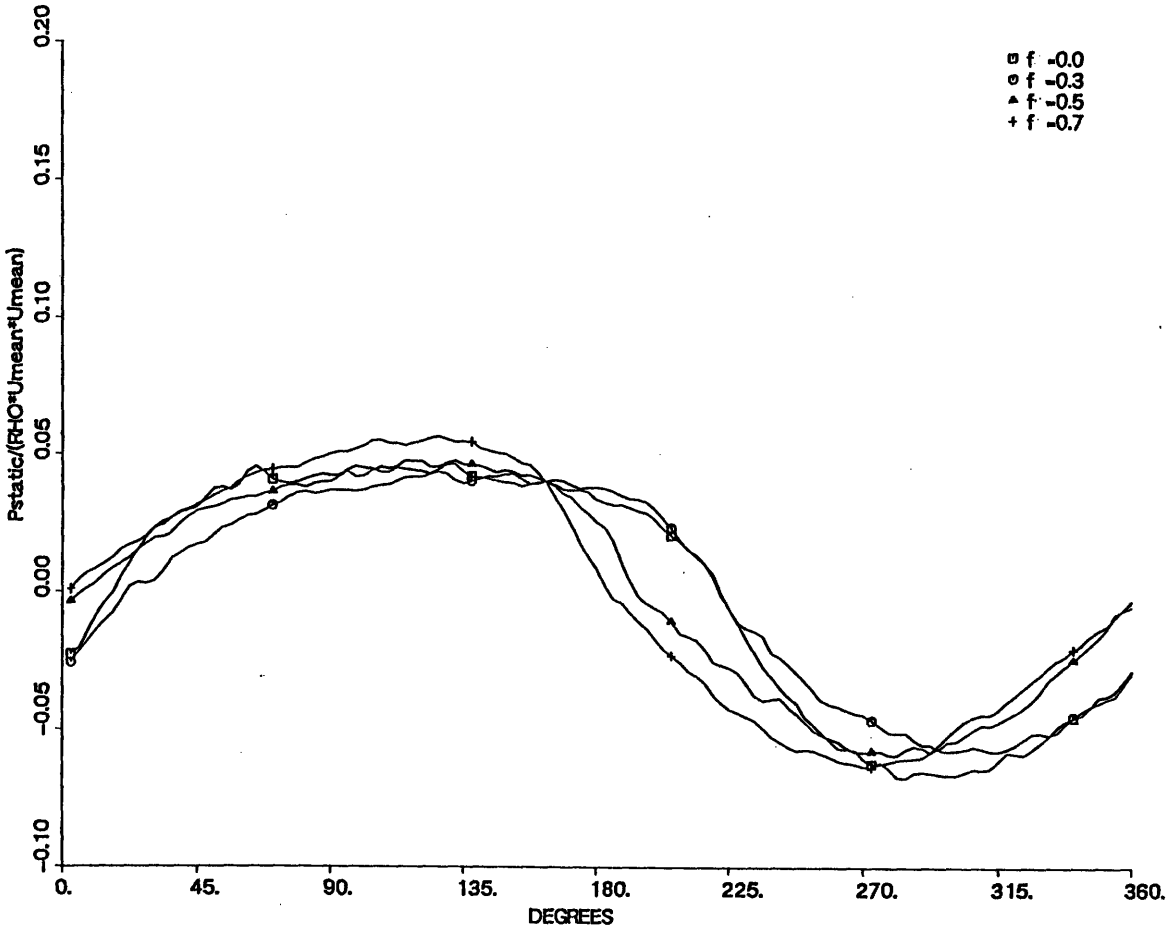

Figure 5-16 Static Pressure Profiles at Plane 0.45 (.32 radii upstream of IGV's) for Positive Rotation Rates, Compressor Operating Near Design

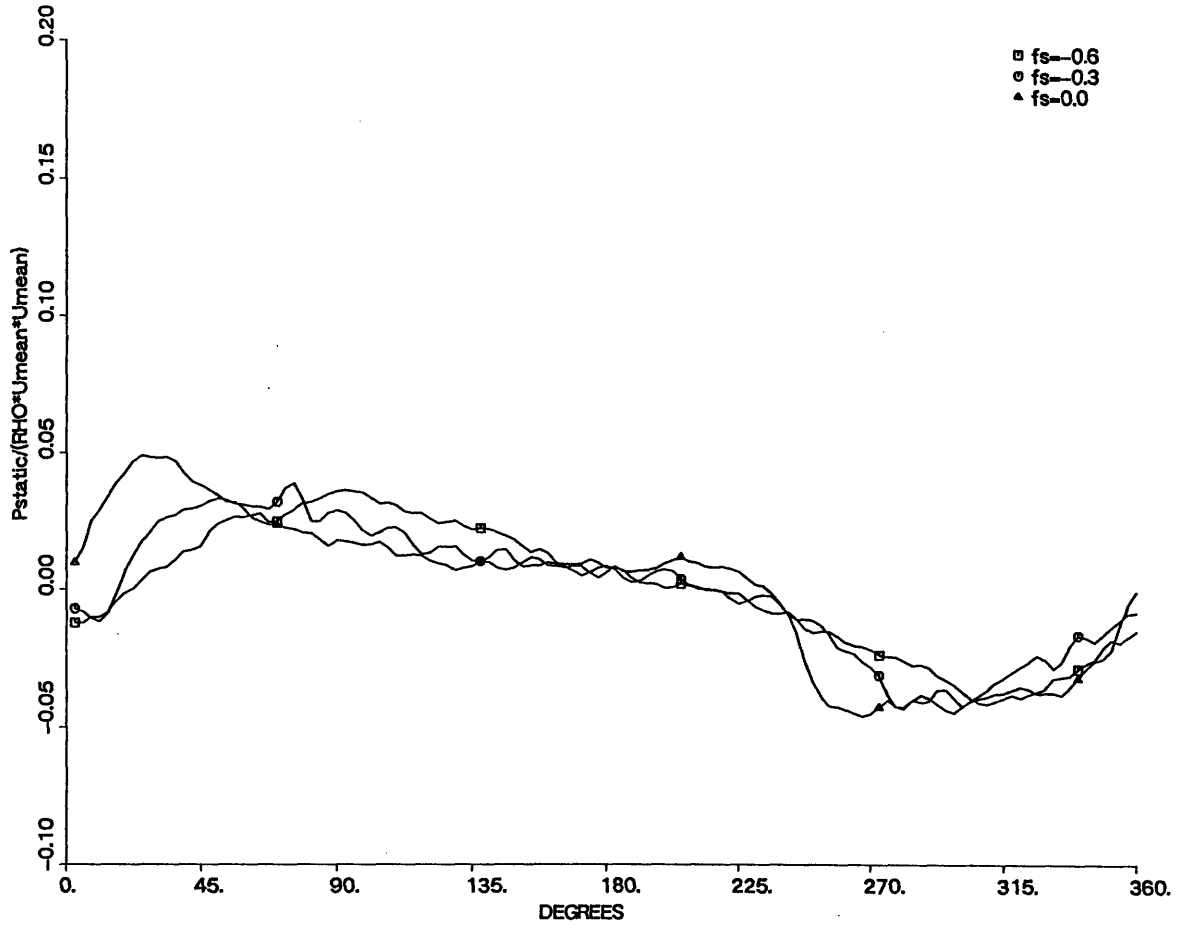

Figure 5-17 Static Pressure Profiles at Plane 1.0 (just downstream of IGV's) for Negative Rotation Rates, Compressor Operating Near Stall

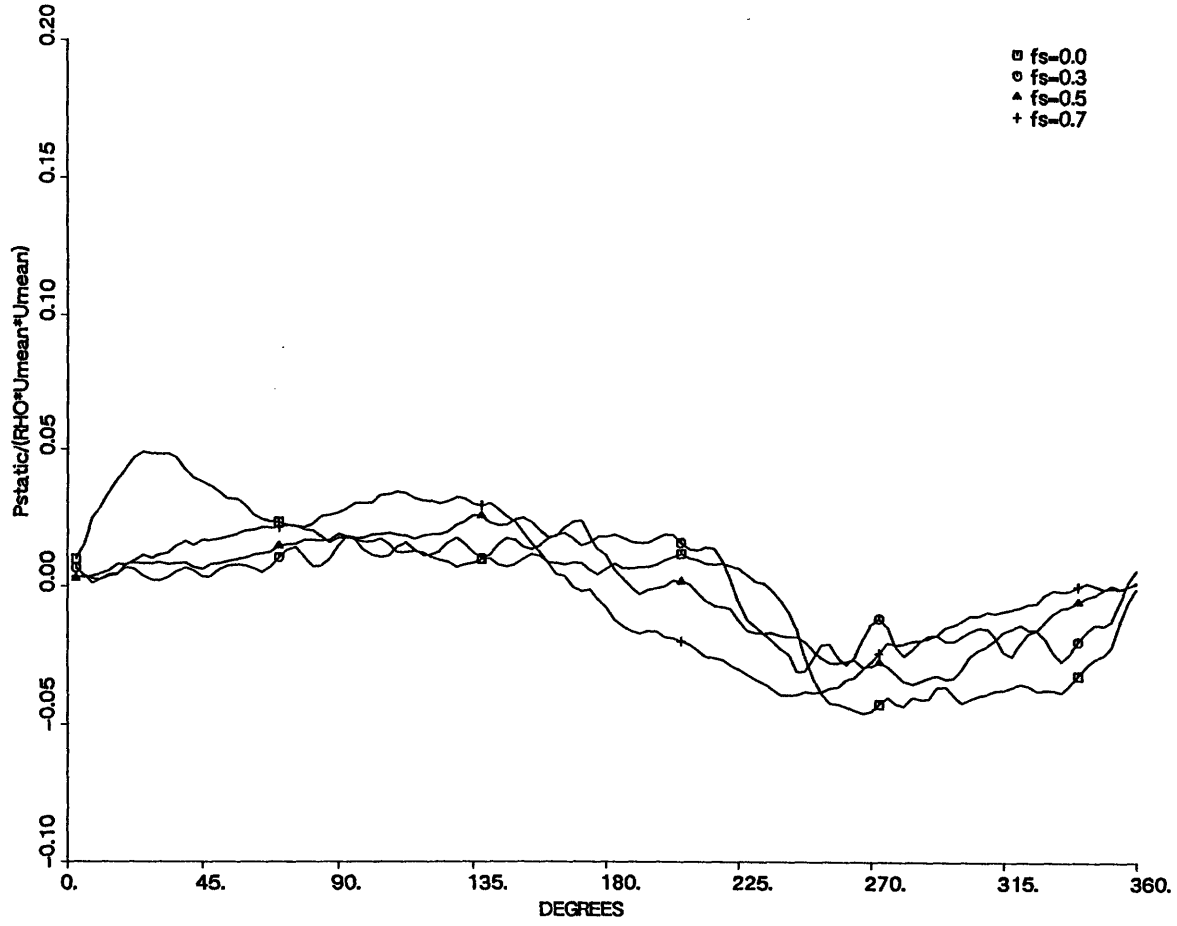

Figure 5-18 Static Pressure Profiles at Plane 1.0 (just downstream of IGV's) for Positive Rotation Rates, Compressor Operating Near Stall

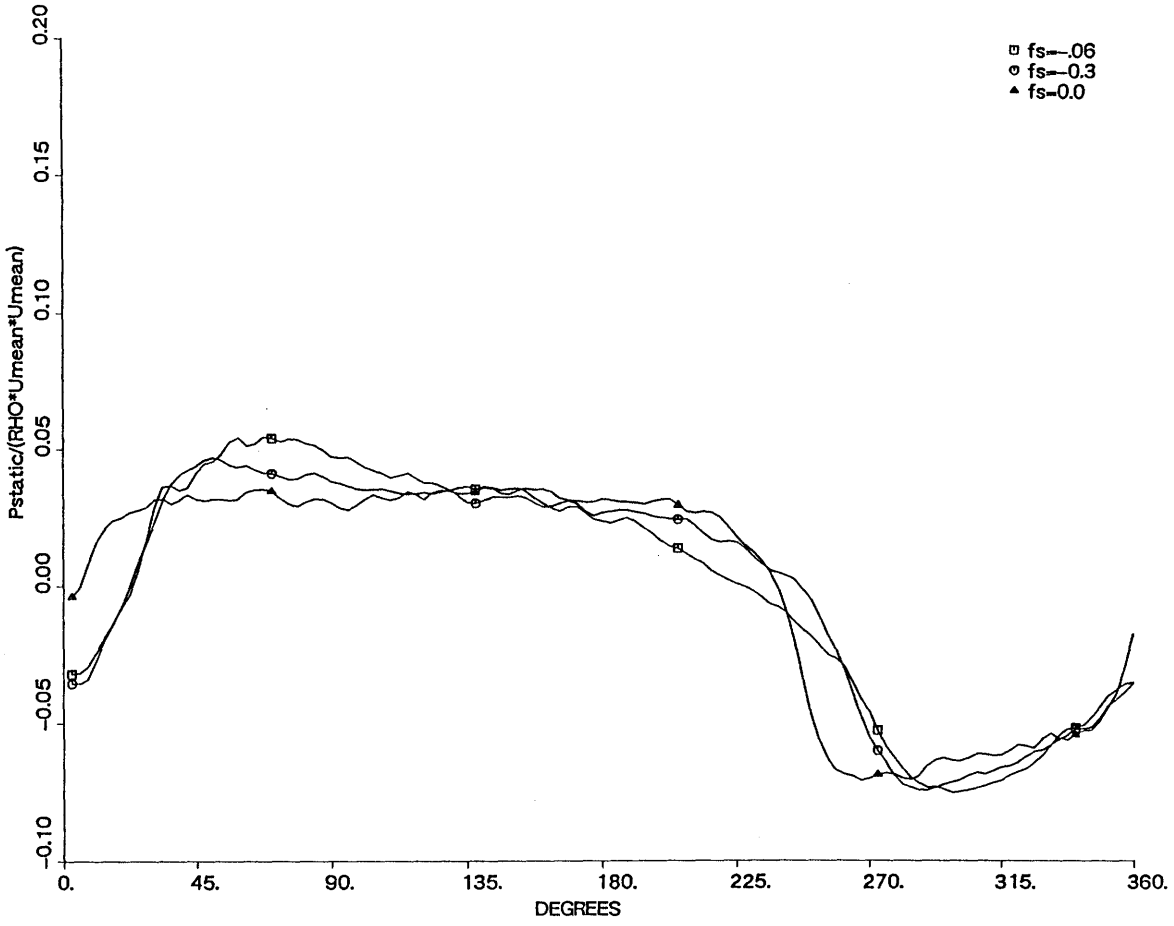

Figure 5-19 Static Pressure Profiles at Plane 1,0 (just downstream of IGV's) for Negative Rotation Rates, Compressor Operating Near Design

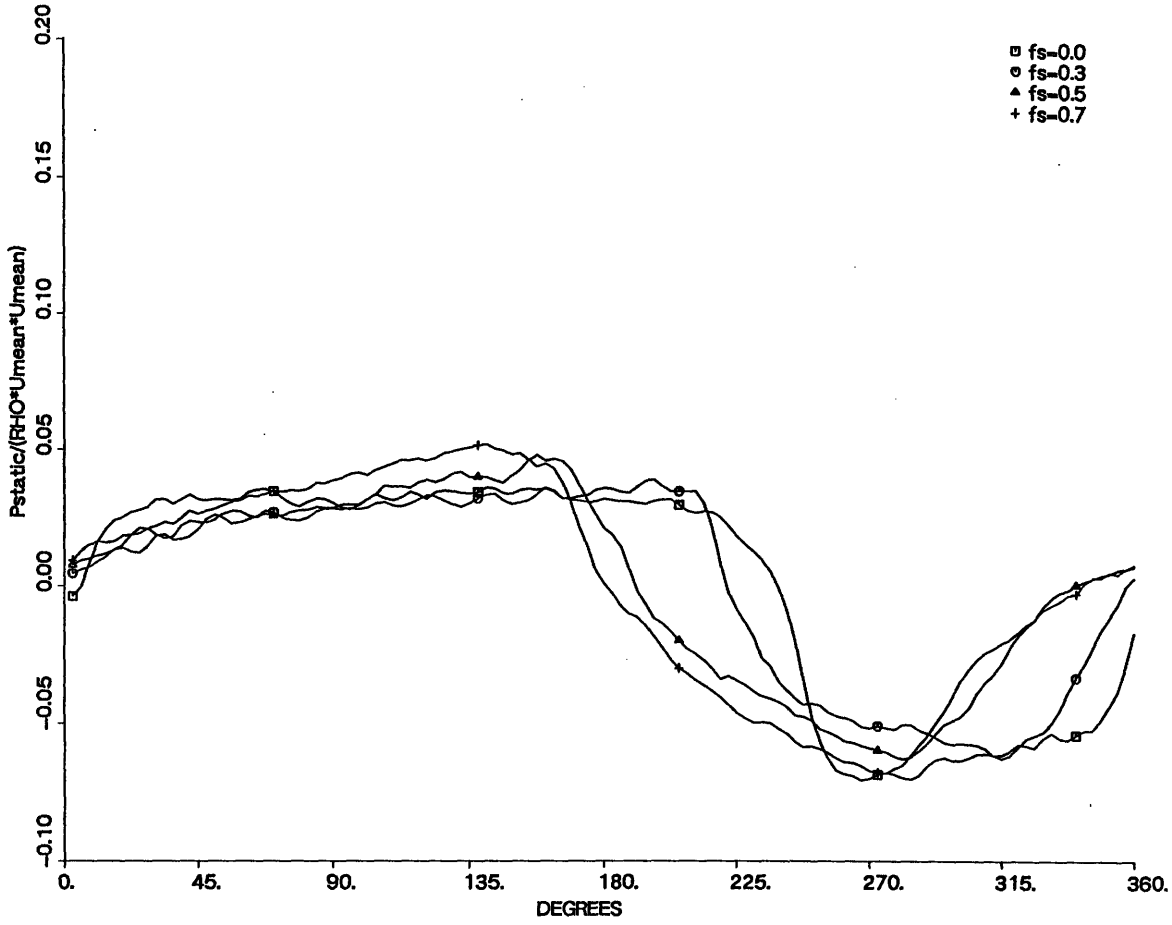

Figure 5-20 Static Pressure Profiles at Plane 1.0 (just downstream of IGV's) for Positive Rotation Rates, Compressor Operating Near Design

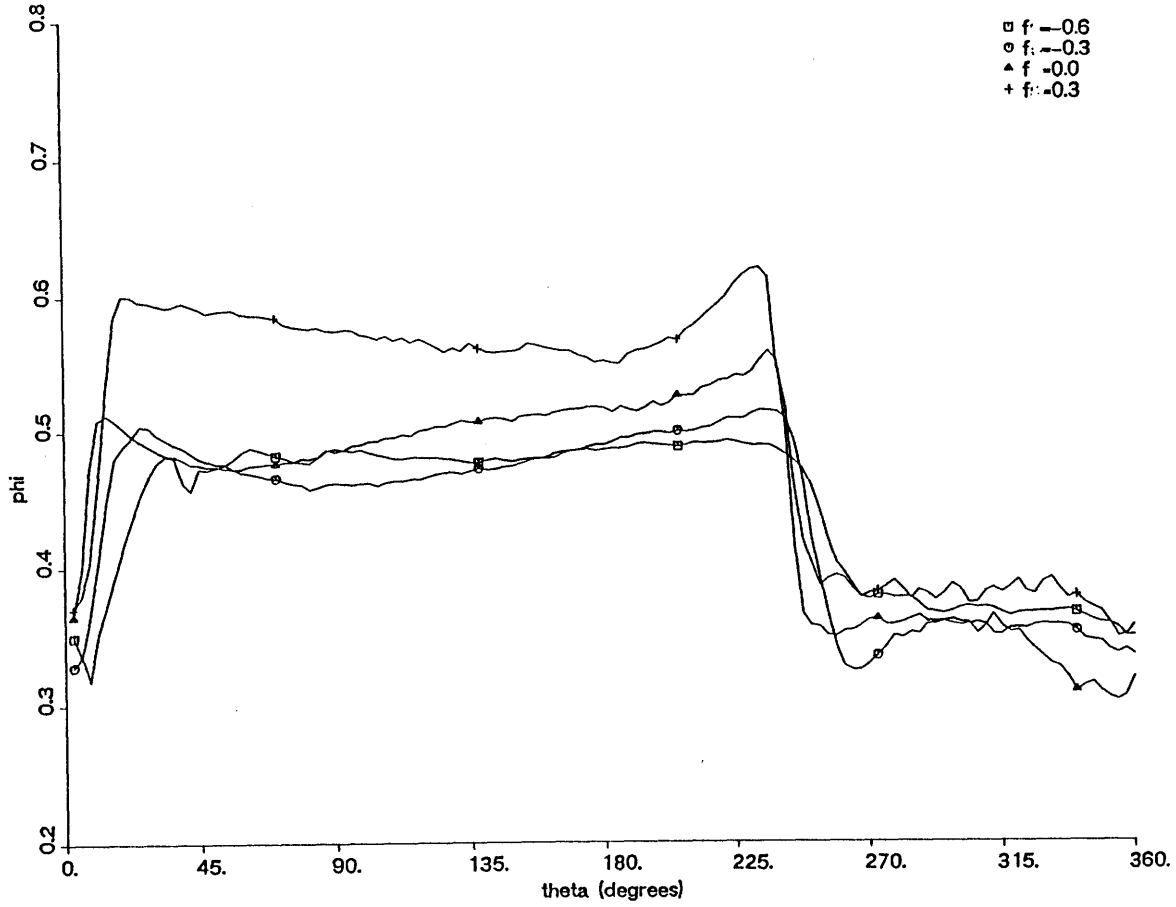

Figure 5-21 Axial Velocity Profiles at Plane 0.45 (.32 radii upstream of IGV's) for Variable Rotation Rates, Compressor Operating Near Stall

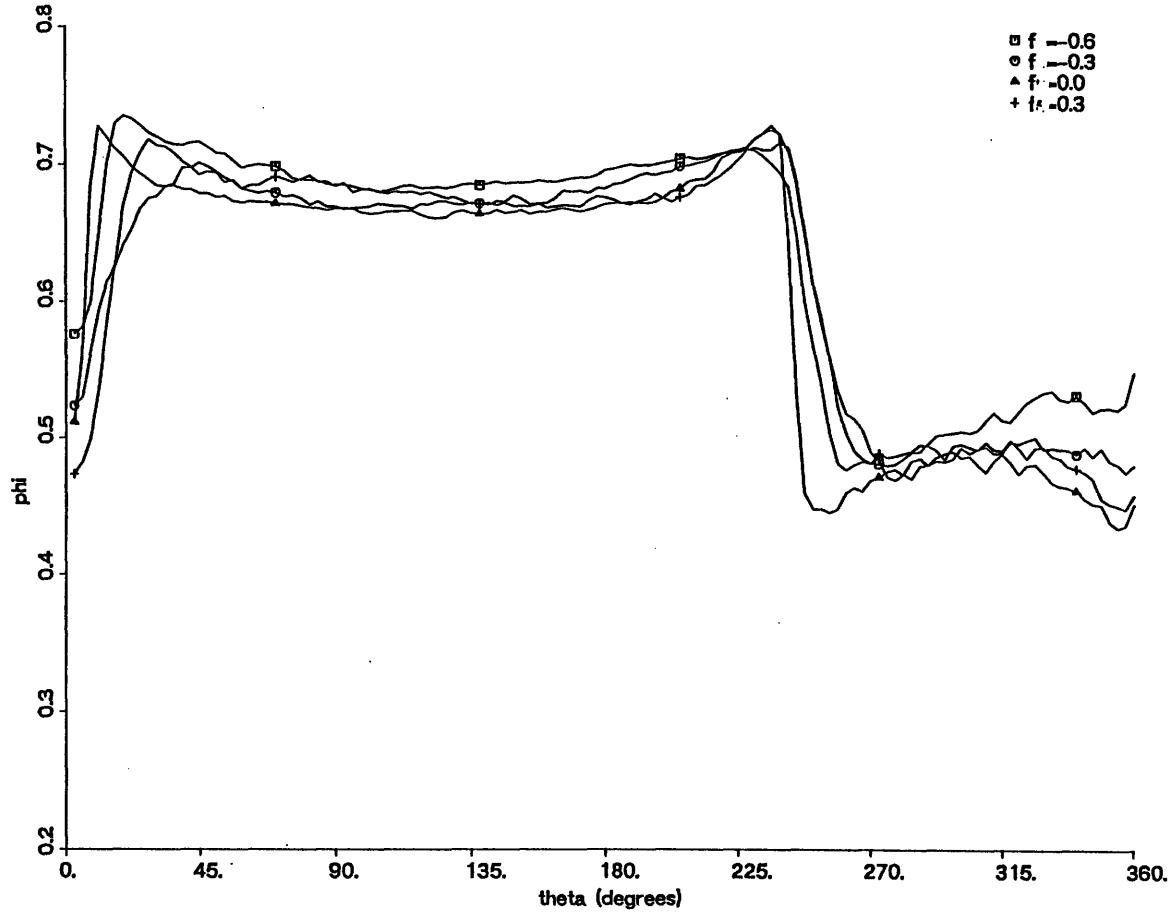

Figure 5-22 Axial Velocity Profiles at Plane 0.45 (.32 radii upstream of IGV's) for Variable Rotation Rates, Compressor Operating Near Design

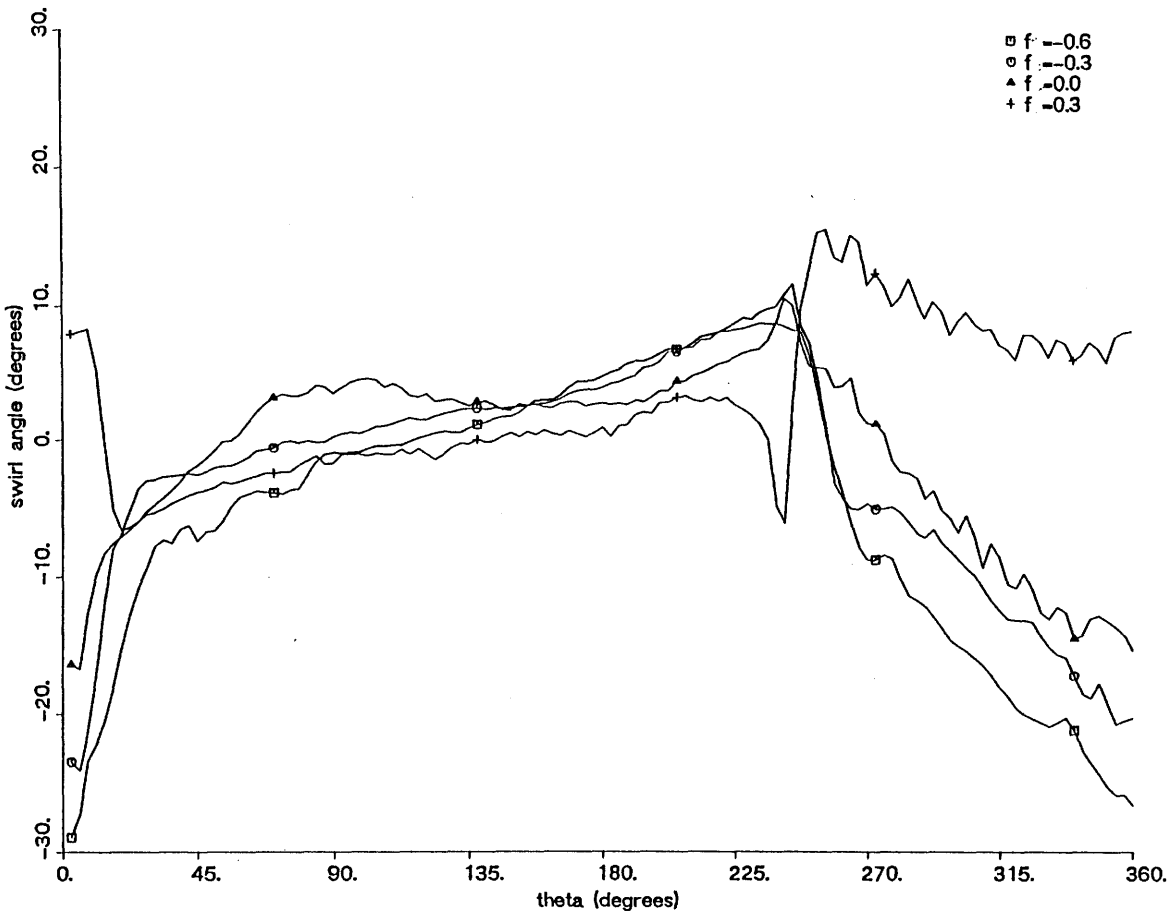

Figure 5-23 Swirl Angle Profiles at Plane 0.45 (.32 radii upstream of IGV's) for Variable Rotation Rates, Compressor Operating Near Stall

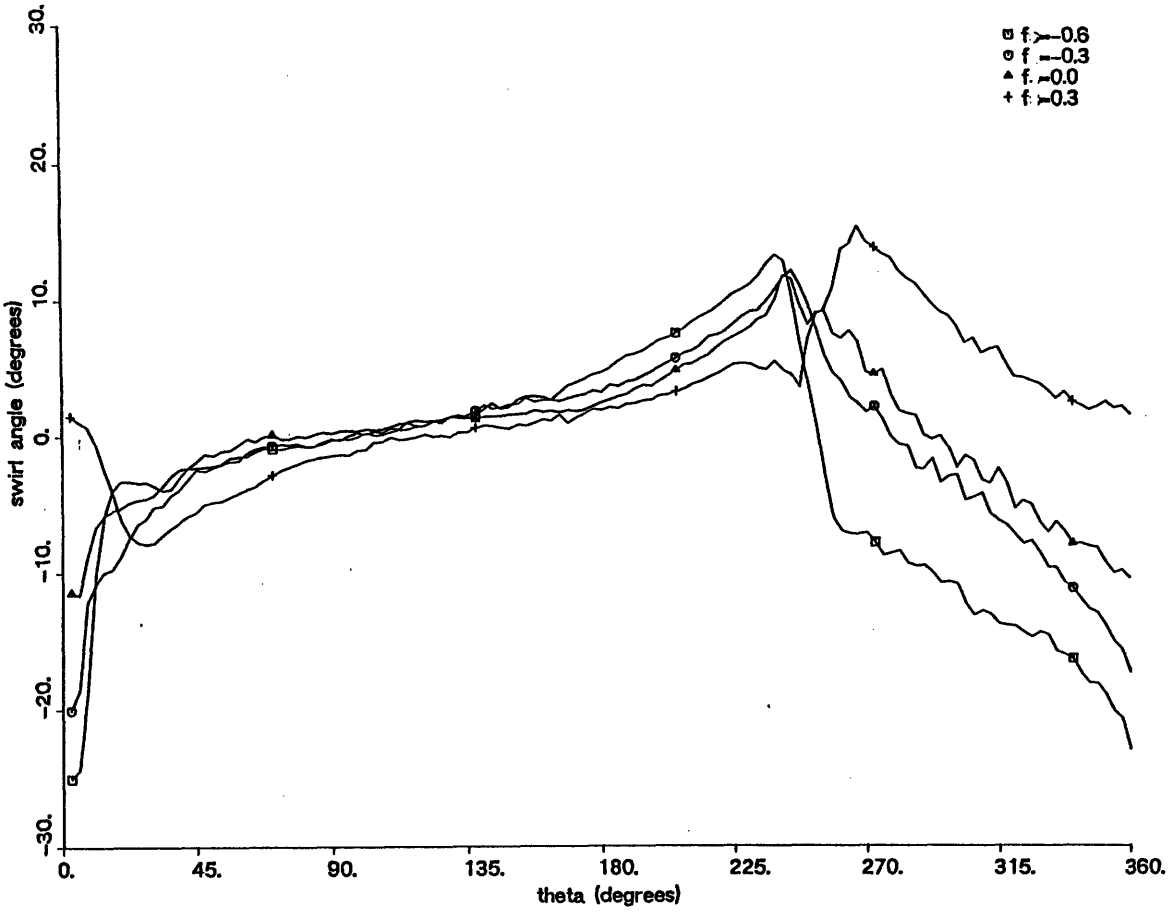

Figure 5-24 Swirl Angle Profiles at Plane 0.45 (.32 radii upstream of IGV's) for Variable Rotation Rates, Compressor Operating Near Design

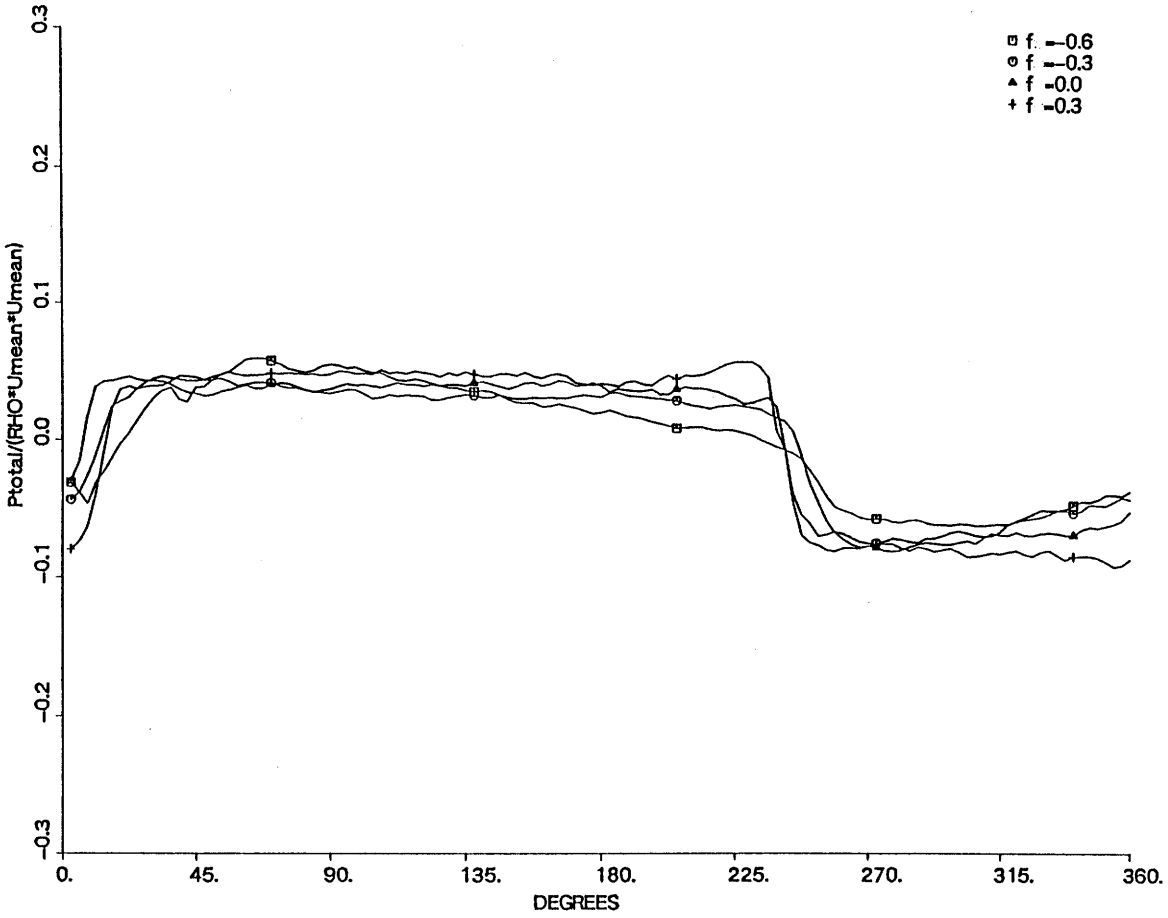

Figure 5-25 Total Pressure Profiles at Plane 0.45 (.32 radii upstream of IGV's) for Variable Rotation Rates, Compressor Operating Near Stall

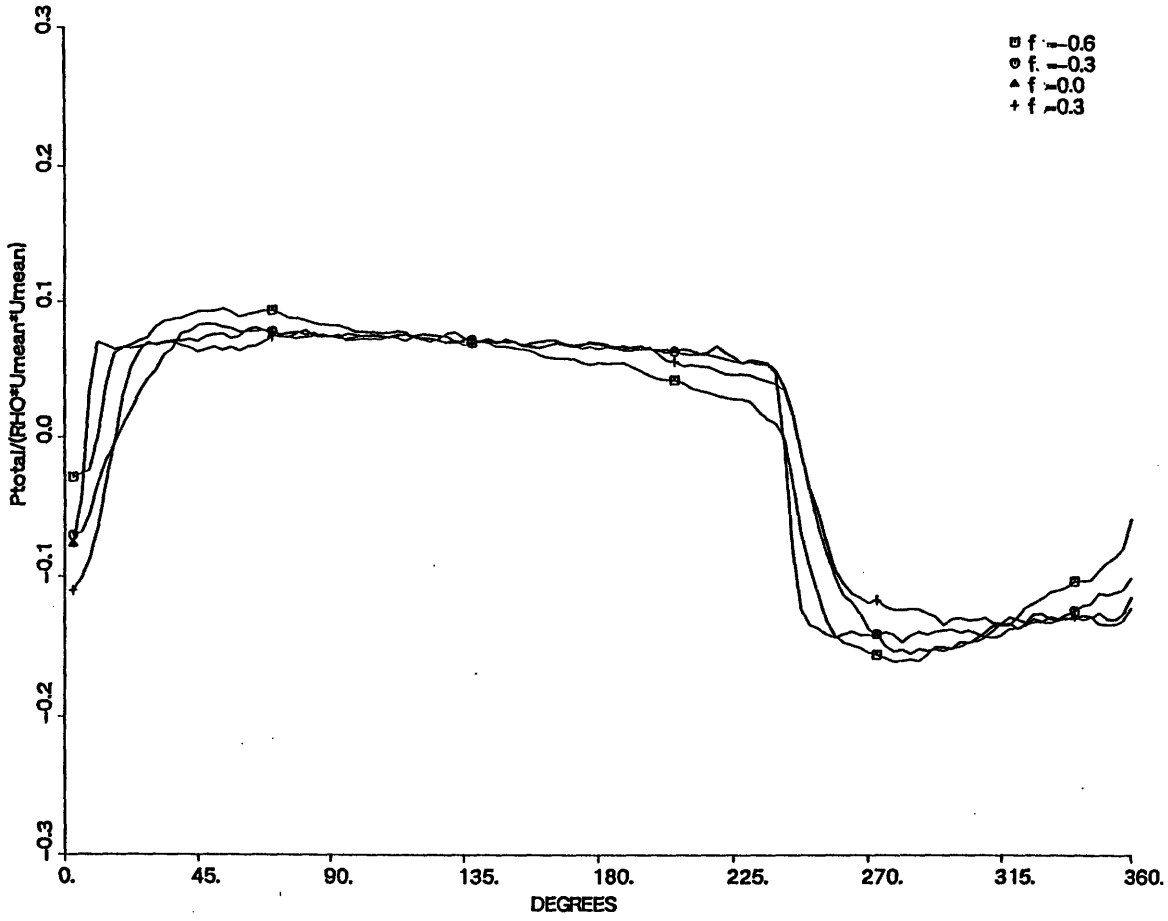

Figure 5-26 Total Pressure Profiles at Plane 0.45 (.32 radii upstream of IGV's) for Variable Rotation Rates, Compressor Operating Near Design

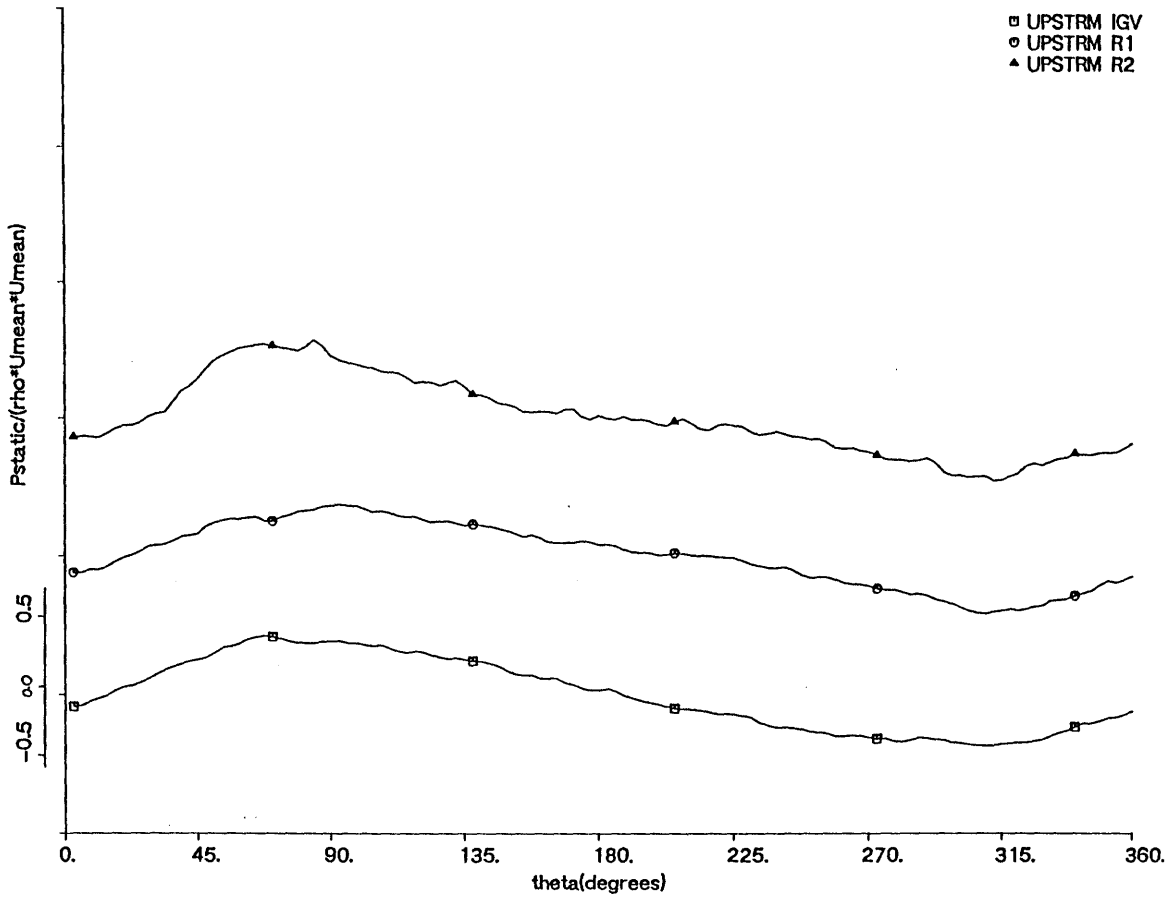

Figure 5-27 Static Pressure Profiles Throughout the Compressor, Standard Distortion, Near Stall, f=-0.6, Relative Scale Only.

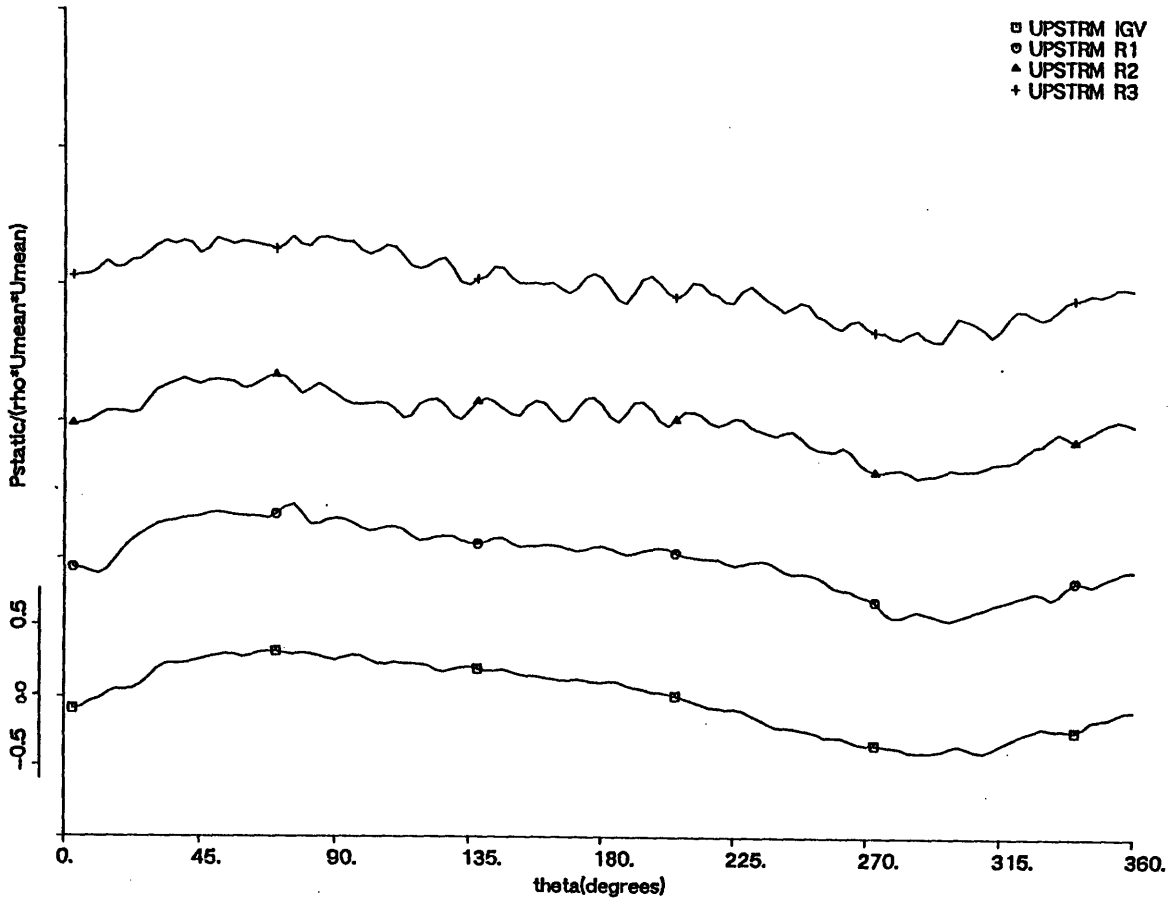

Figure 5-28 Static Pressure Profiles Throughout the Compressor, Standard Distortion, Near Stall, f=-0.3, Relative Scale Only.

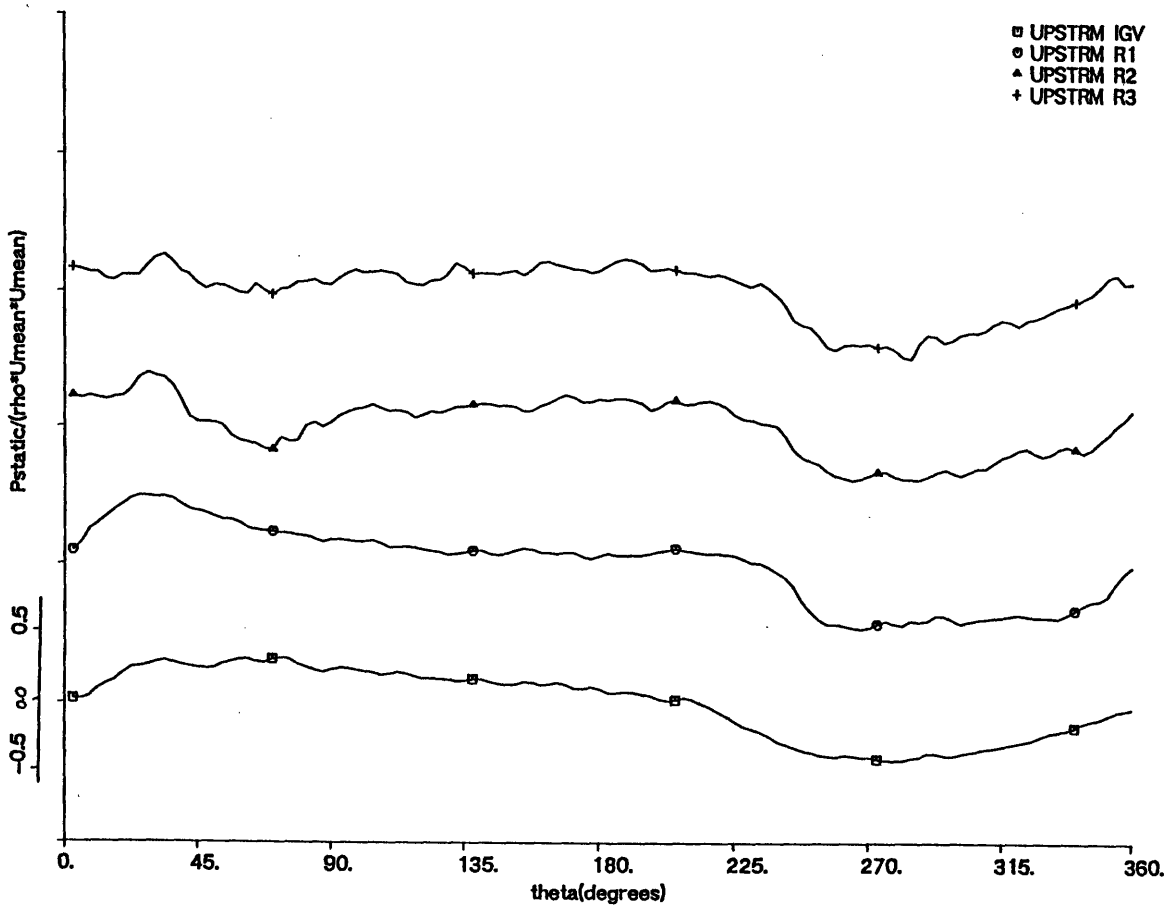

Figure 5-29 Static Pressure Profiles Throughout the Compressor, Standard Distortion, Near Stall, f=0.0, Relative Scale Only.

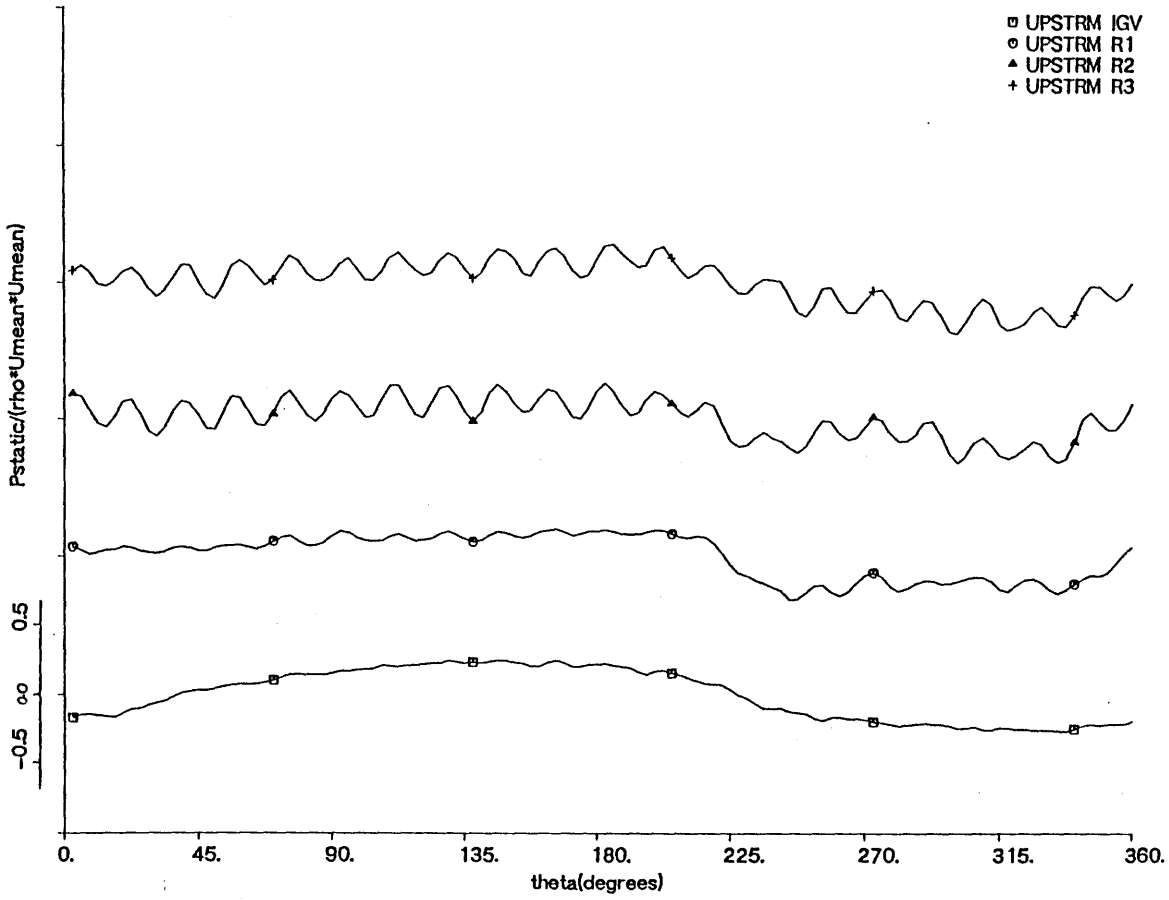

Figure 5-30 Static Pressure Profiles Throughout the Compressor, Standard Distortion, Near Stall, f=0.3, Relative Scale Only.

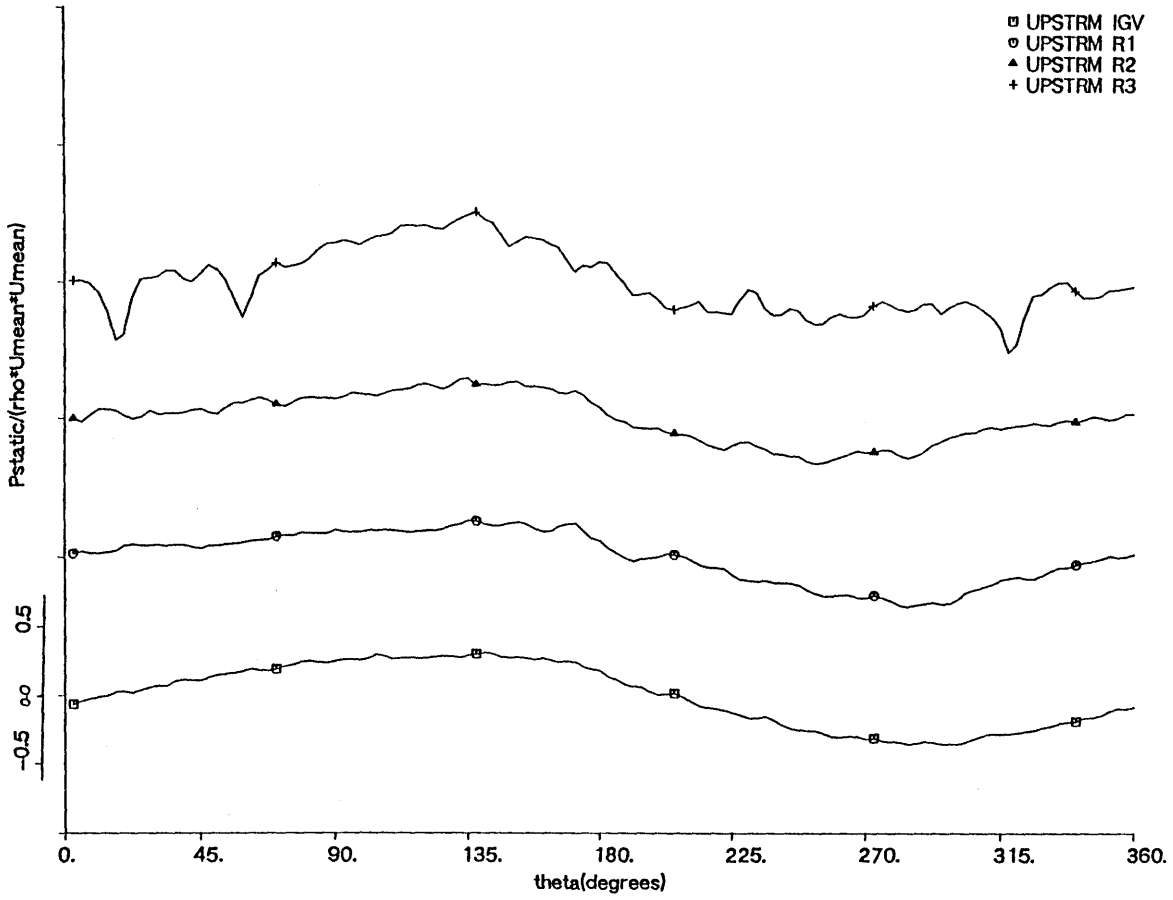

Figure 5-31 Static Pressure Profiles Throughout the Compressor, Standard Distortion, Near Stall, f=0.5, Relative Scale Only.

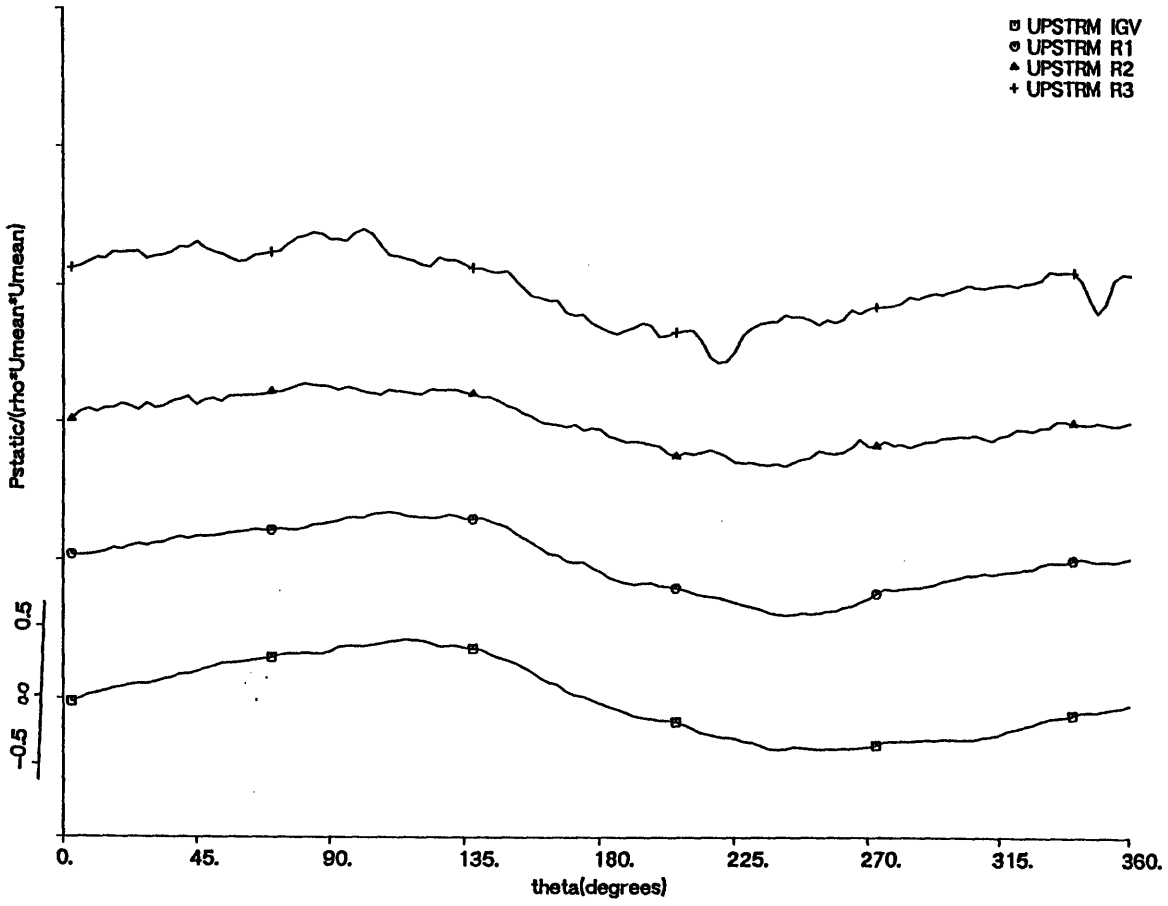

Figure 5-32 Static Pressure Profiles Throughout the Compressor, Standard Distortion, Near Stall, f=0.7 Relative Scale Only.

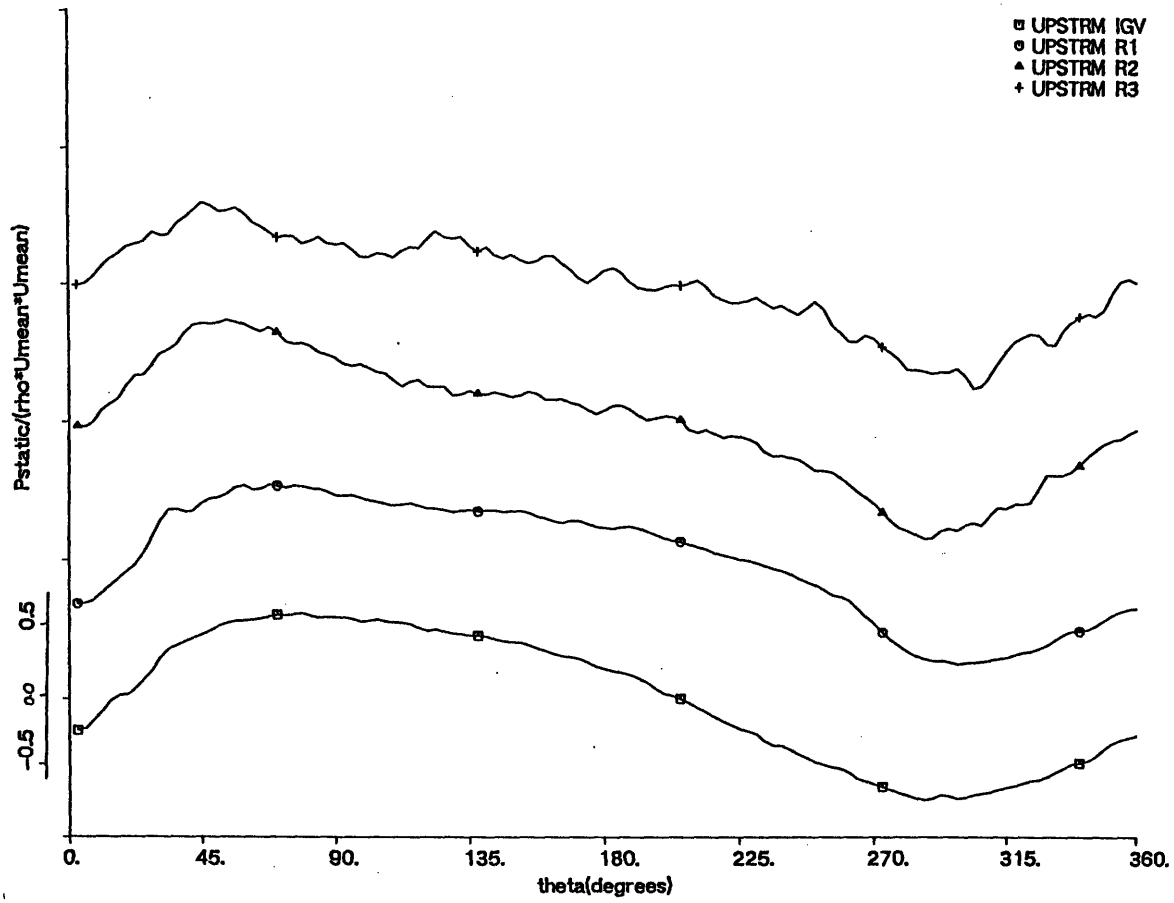

Figure 5-33 Static Pressure Profiles Throughout the Compressor, Standard Distortion, Near Design, f=-0.6, Relative Scale Only.

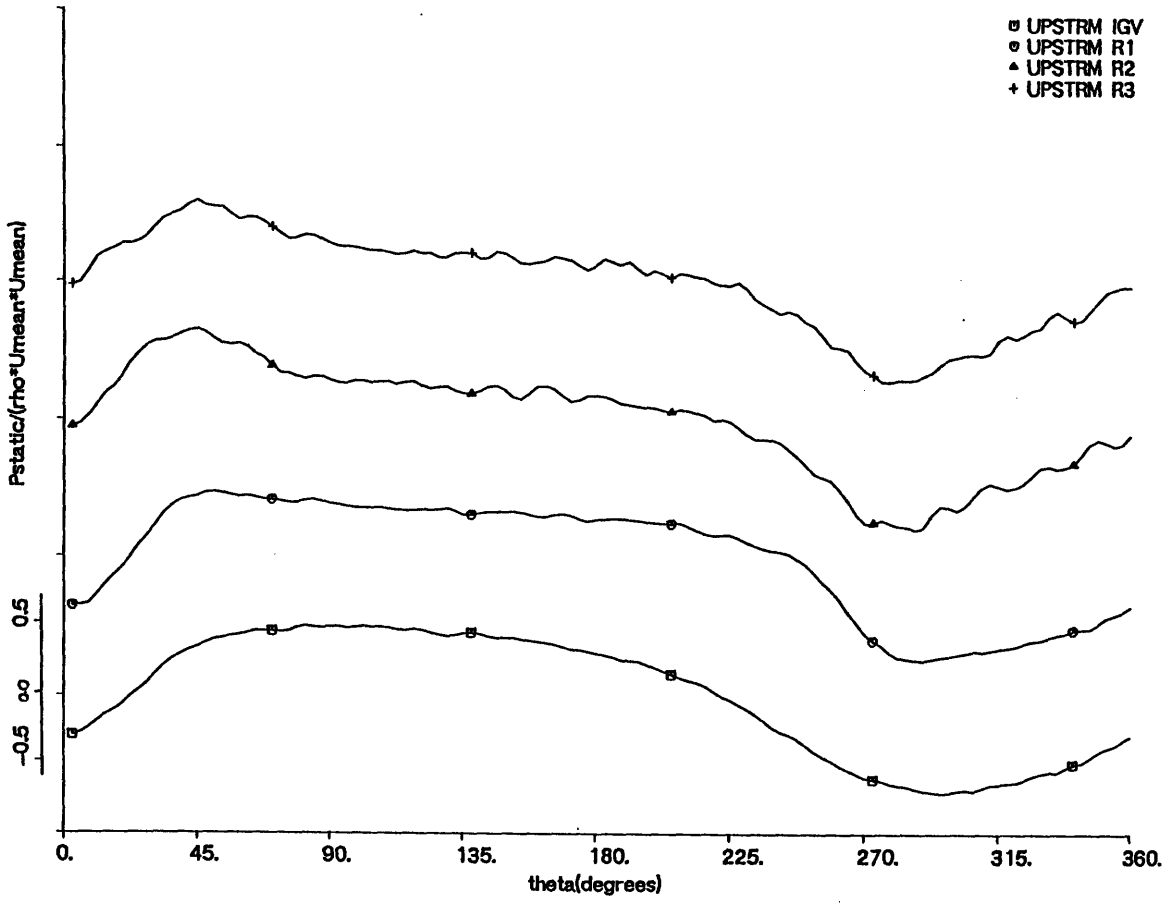

Figure 5-34 Static Pressure Profiles Throughout the Compressor, Standard Distortion, Near Design, f=-0.3, Relative Scale Only.

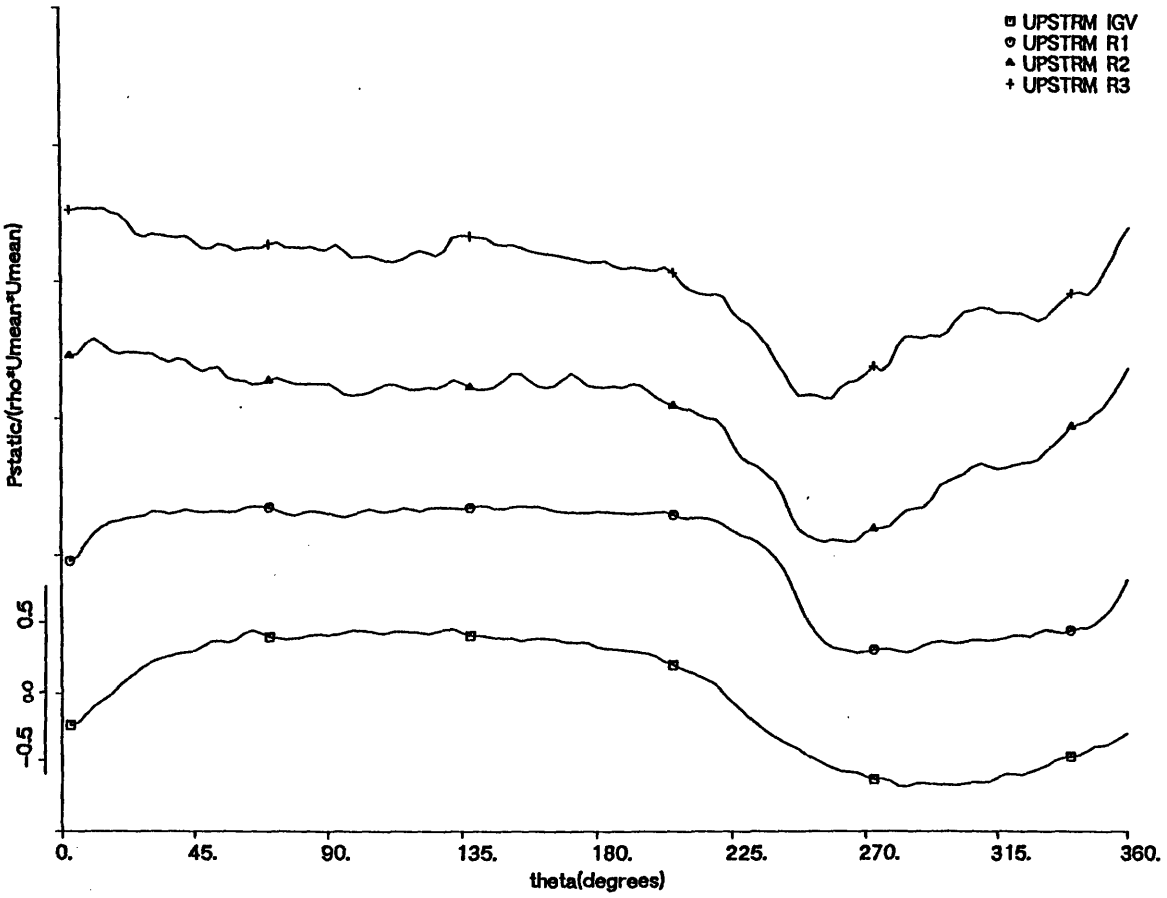

Figure 5-35 Static Pressure Profiles Throughout the Compressor, Standard Distortion, Near Design, f=0.0, Relative Scale Only.

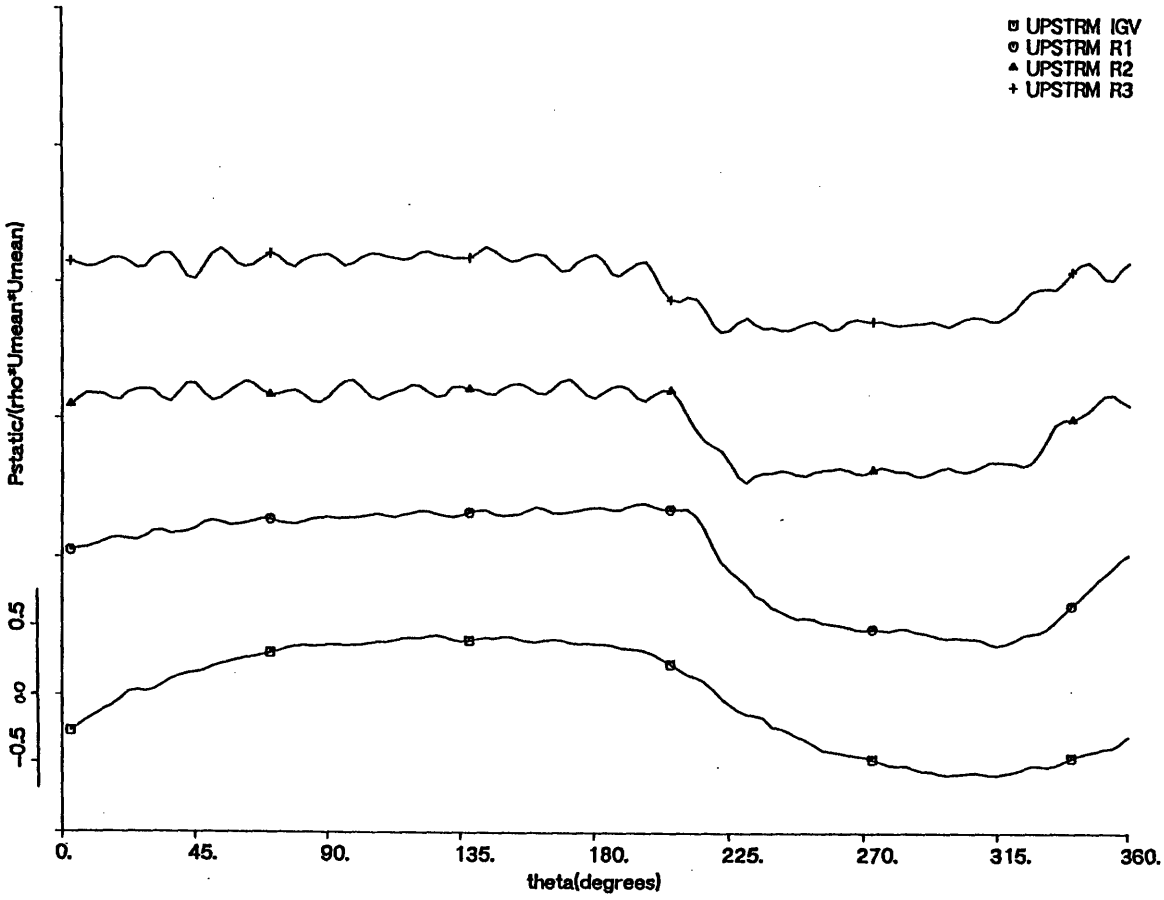

Figure 5-36 Static Pressure Profiles Throughout the Compressor, Standard Distortion, Near Design, f=0.3, Relative Scale Only.

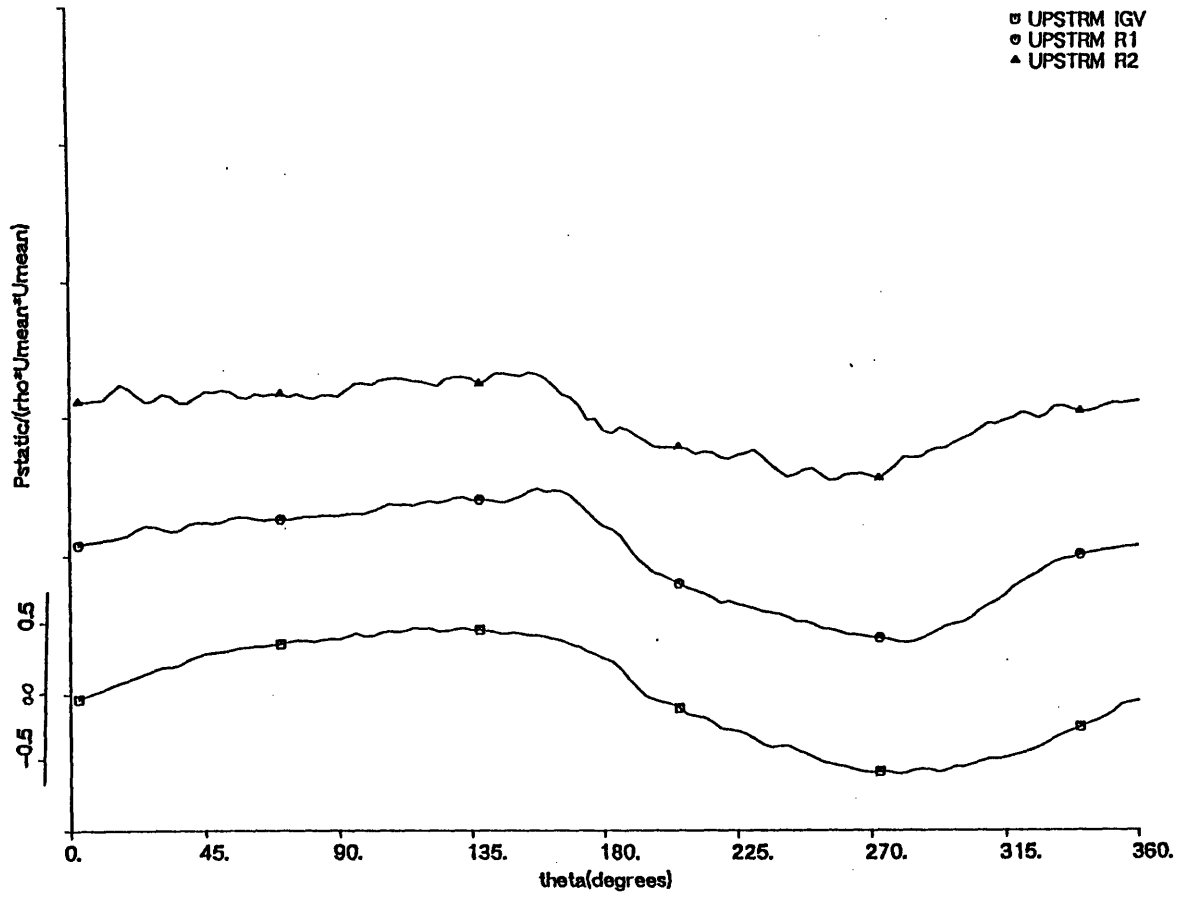

Figure 5-37 Static Pressure Profiles Throughout the Compressor, Standard Distortion, Near Design f=0.5, Relative Scale Only.

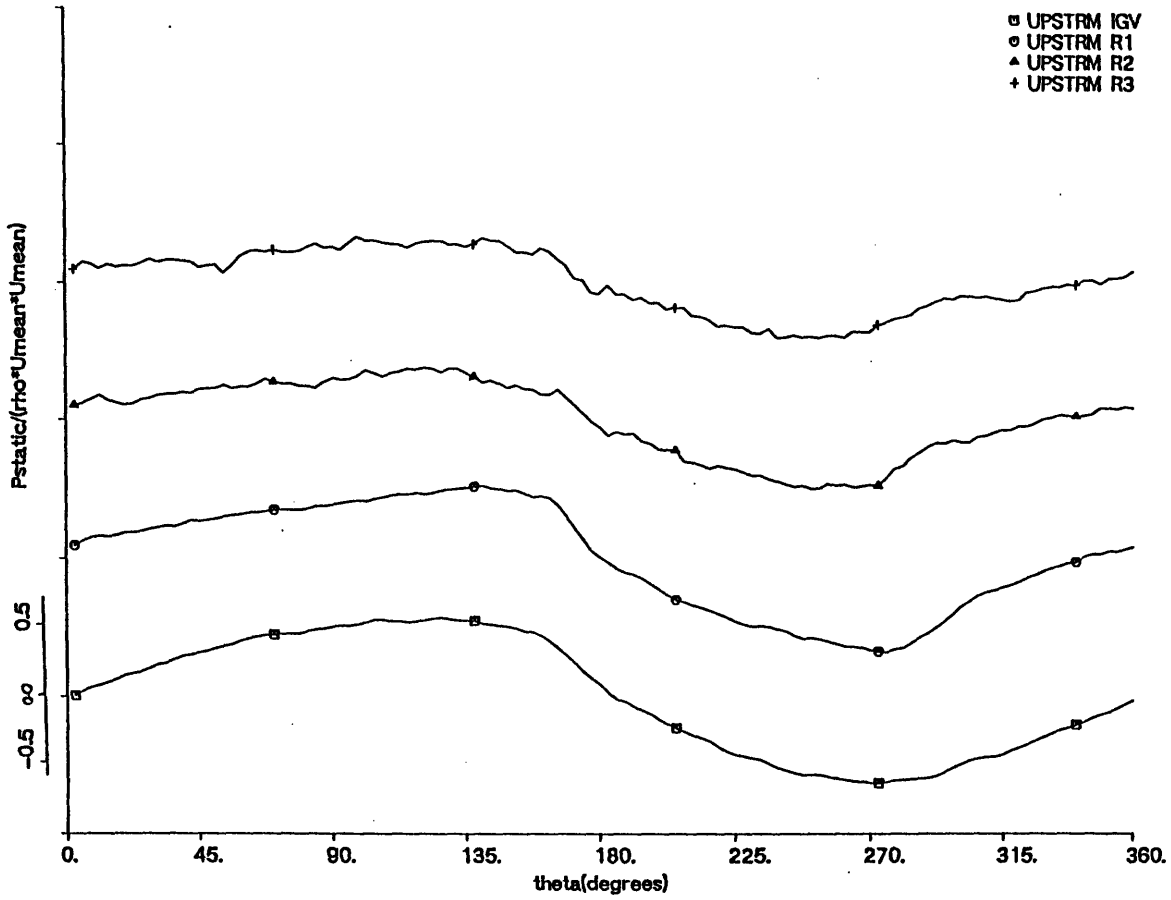

Figure 5-38 Static Pressure Profiles Throughout the Compressor, Standard Distortion, Near Design, f=0.7, Relative Scale Only.

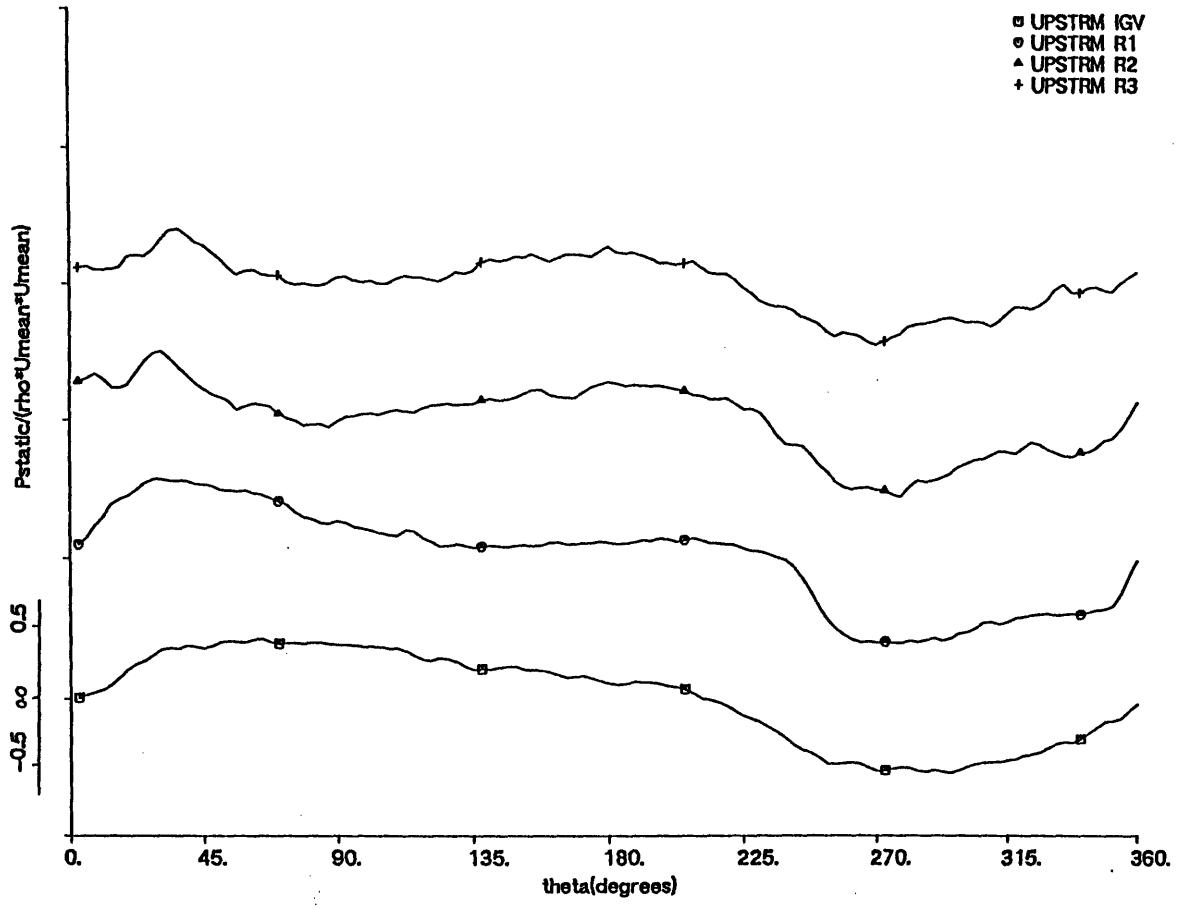

Figure 5-39 Static Pressure Profiles Throughout the Compressor, Heavy Distortion, Near Stall, f=0.0, Relative Scale Only.

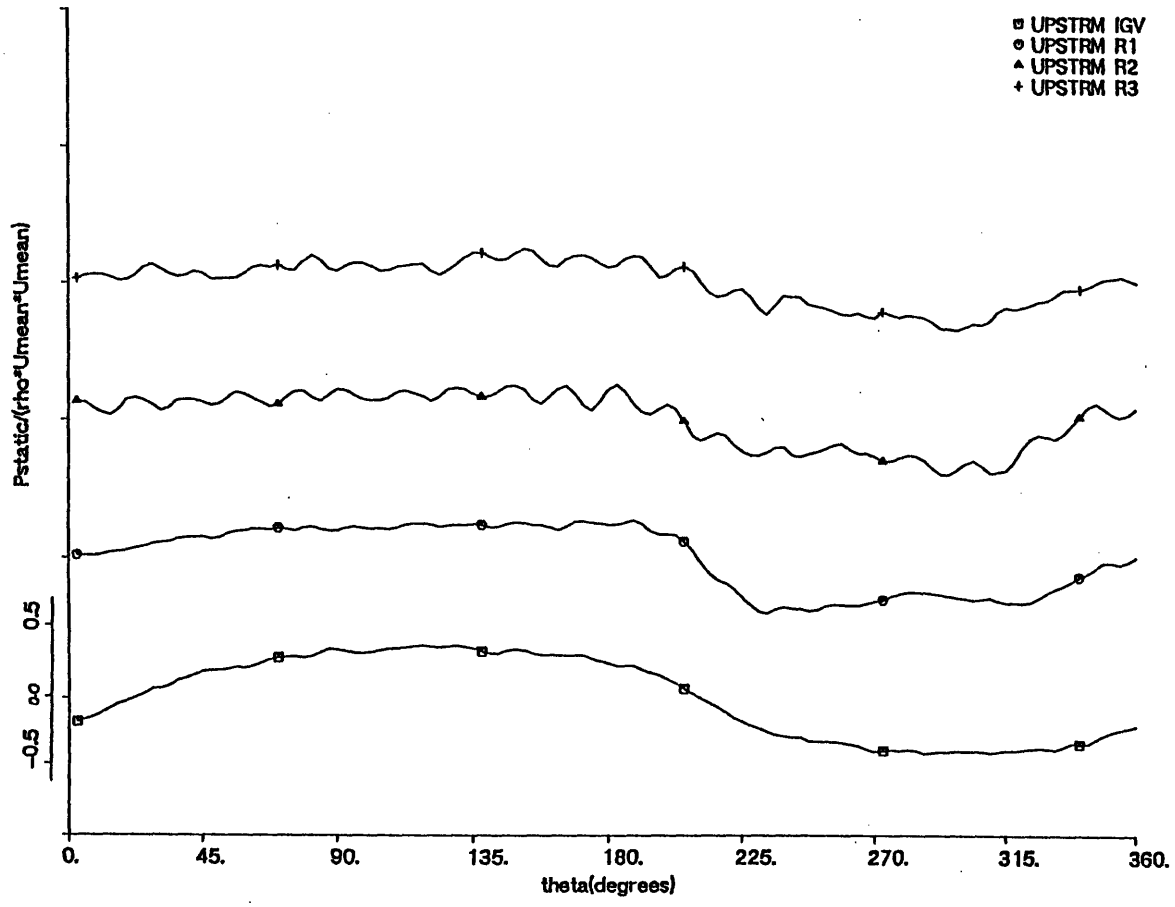

Figure 5-40 Static Pressure Profiles Throughout the Compressor, Heavy Distortion, Near Stall, f=0.3, Relative Scale Only.

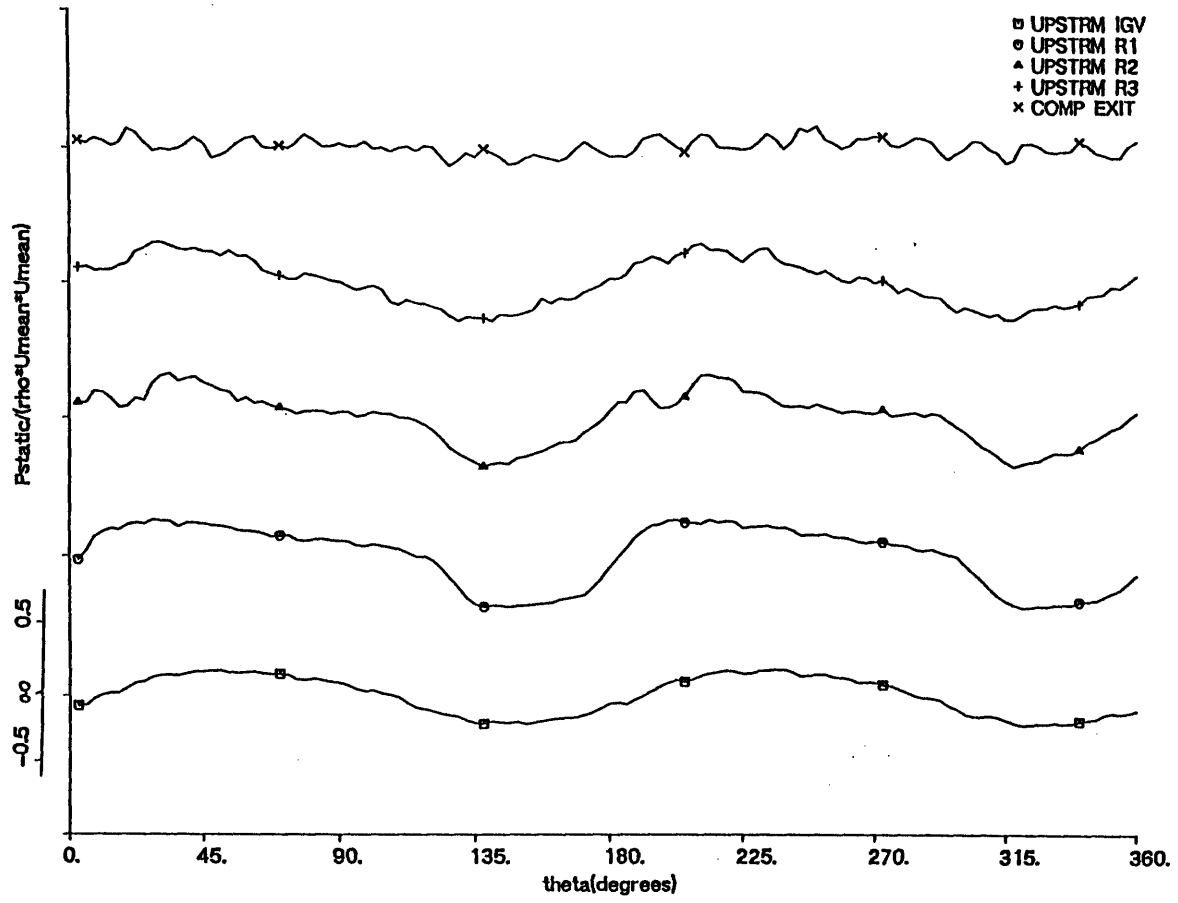

Figure 5-41 Static Pressure Profiles Throughout the Compressor, Double Distortion, Near Stall, f=0.0, Relative Scale Only.

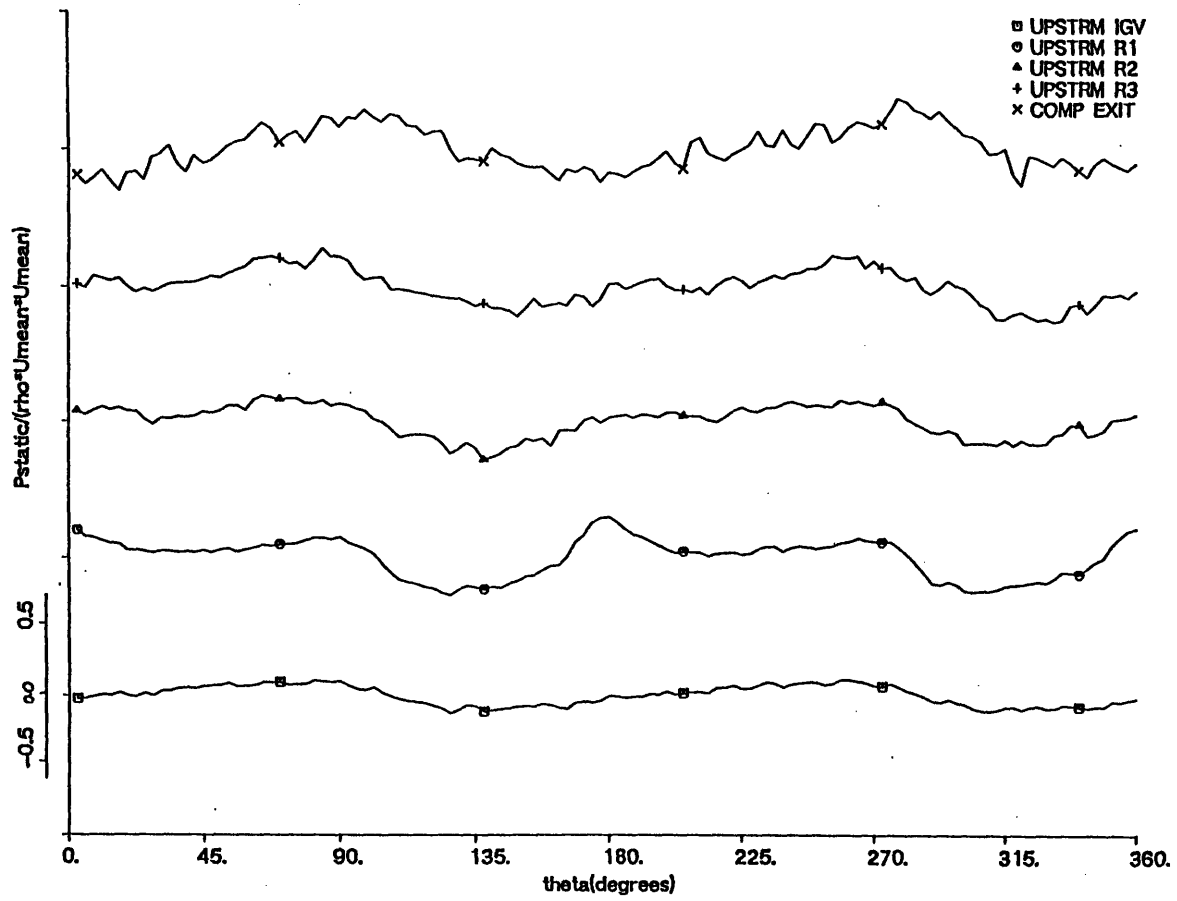

Figure 5-42 Static Pressure Profiles Throughout the Compressor, Double Distortion, Near Stall, f=0.3, Relative Scale Only.

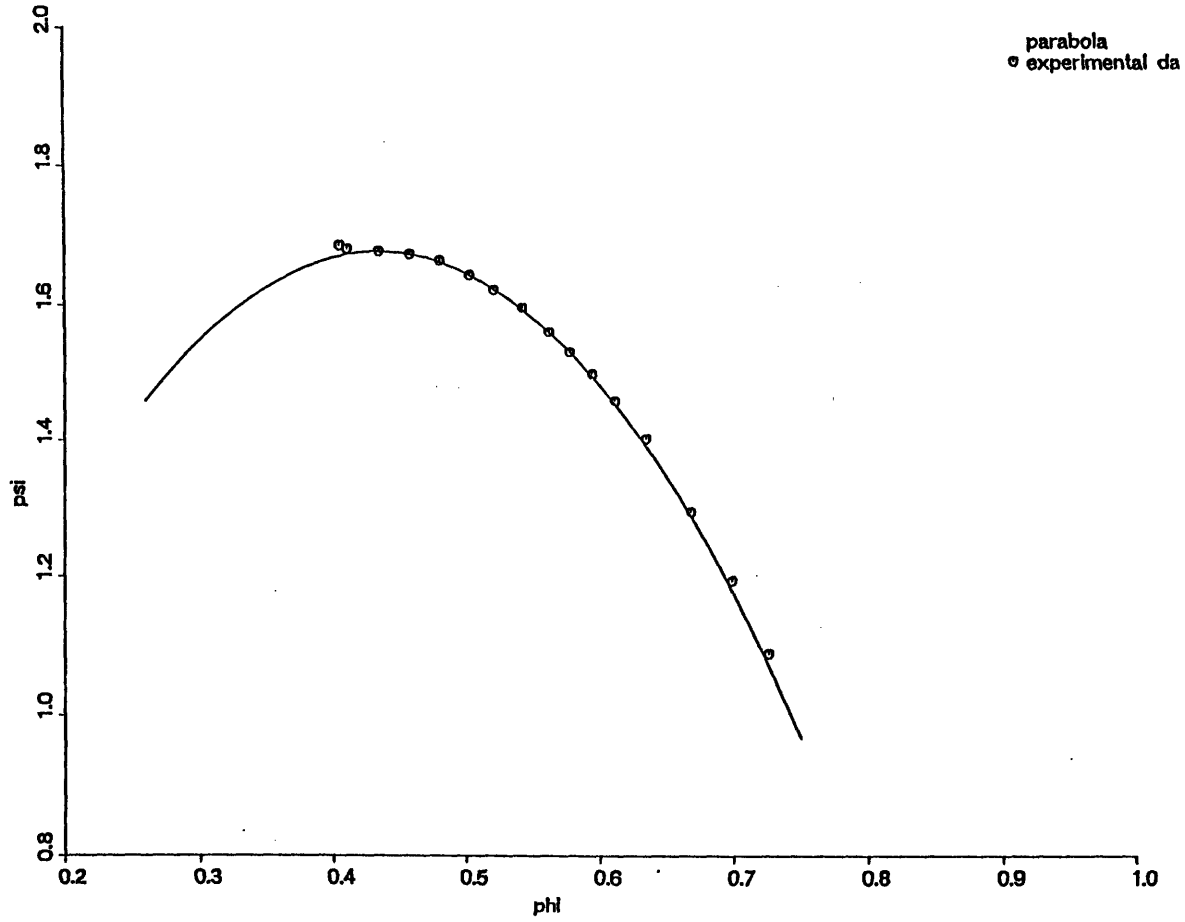

Figure 6-1 Compressor Characteristic: Parabolic Fit Through Experimental Data

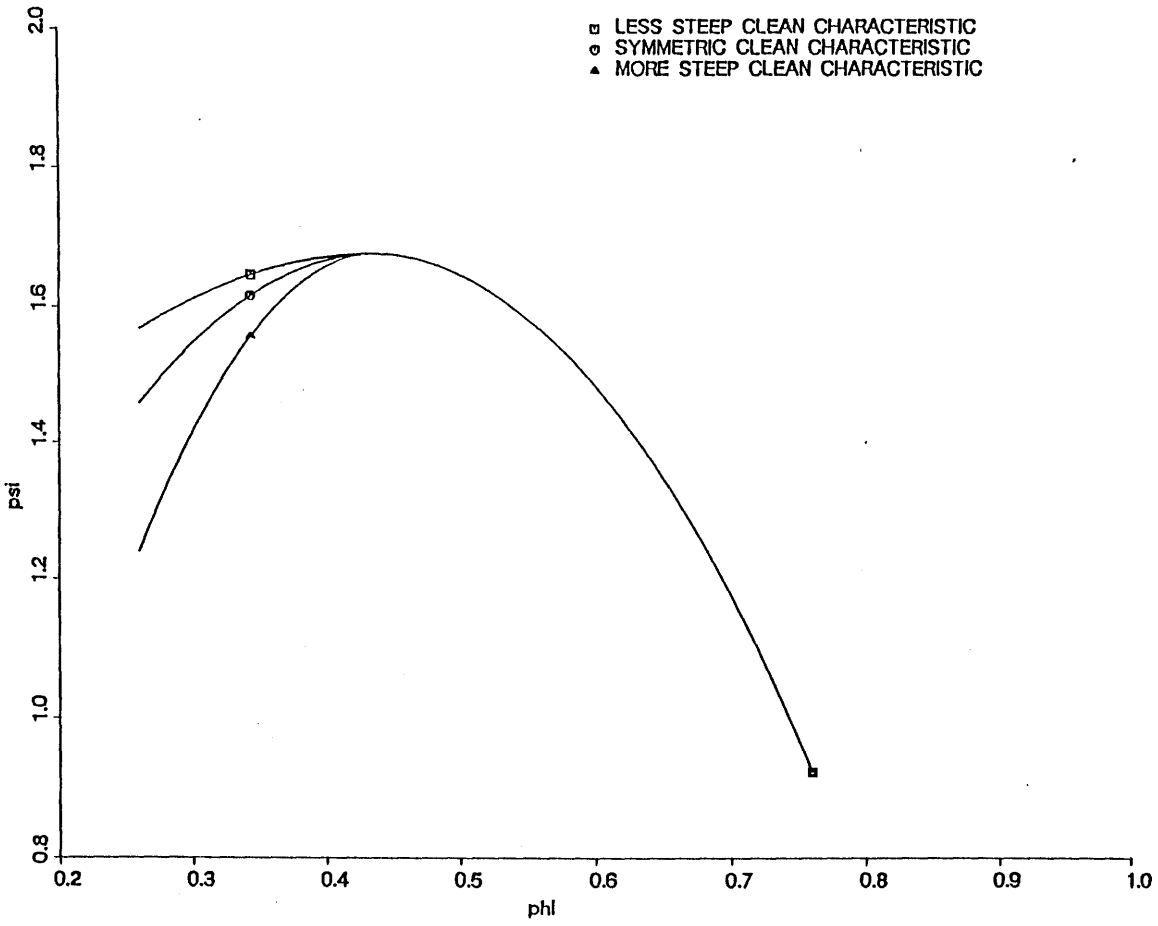

Figure 6-2 Undistorted Flow Compressor Characteristics with Variable Low Flow Side Steepness, Used in Calculations

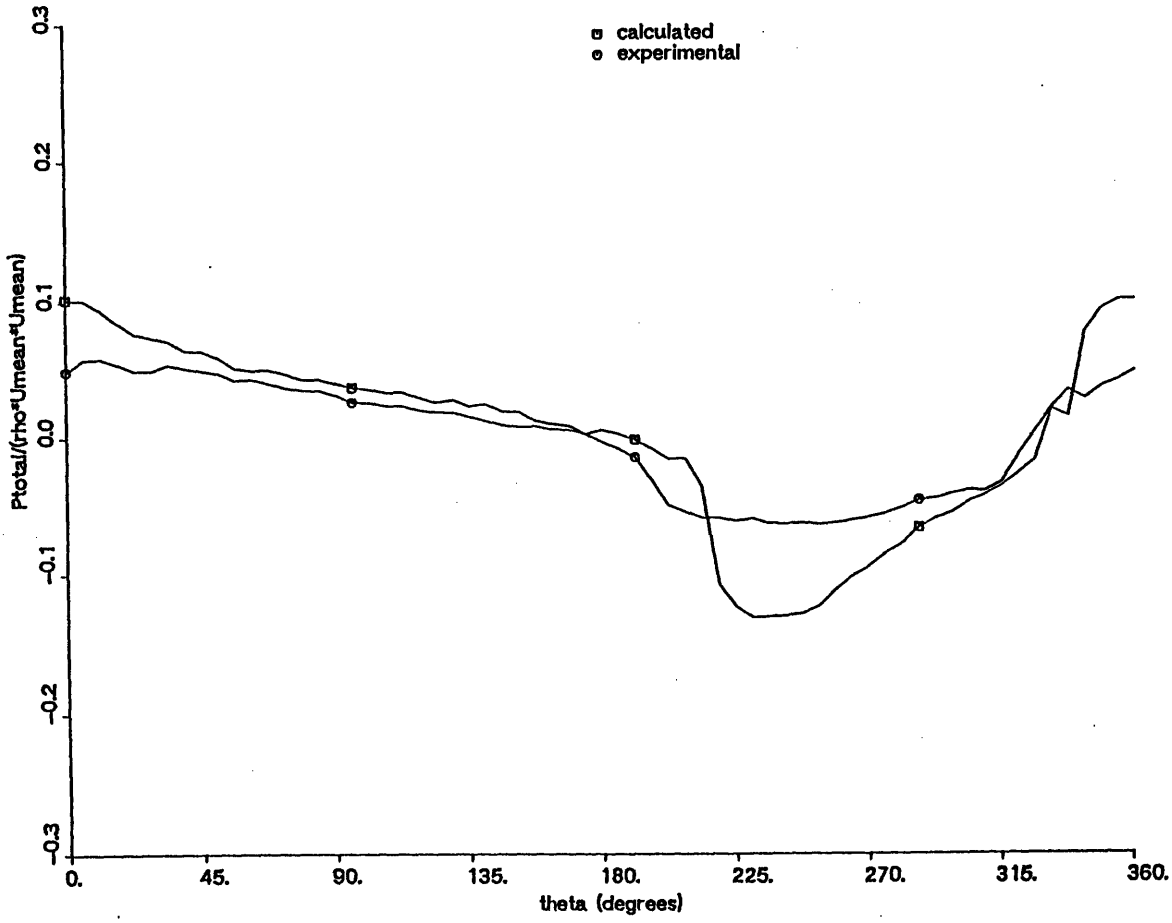

Figure 6-3 Comparison of Calculated and Measured Total Pressure Profiles, at plane 0.45 (.32 radii upstream of IGV's), Near Stall, f=-0.6

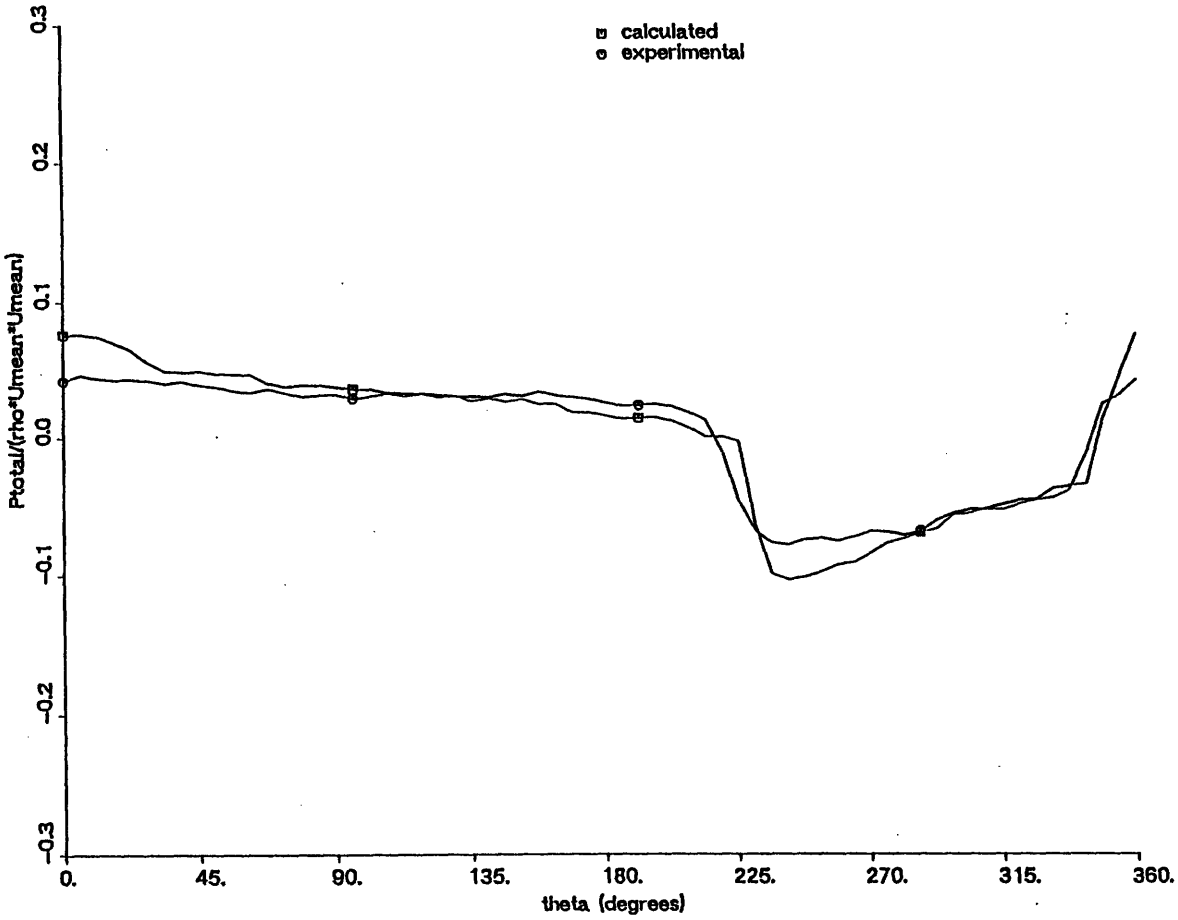

Figure 6-4 Comparison of Calculated and Measured Total Pressure Profiles, at plane 0.45 (.32 radii upstream of IGV's), Near Stall, f=-0.3

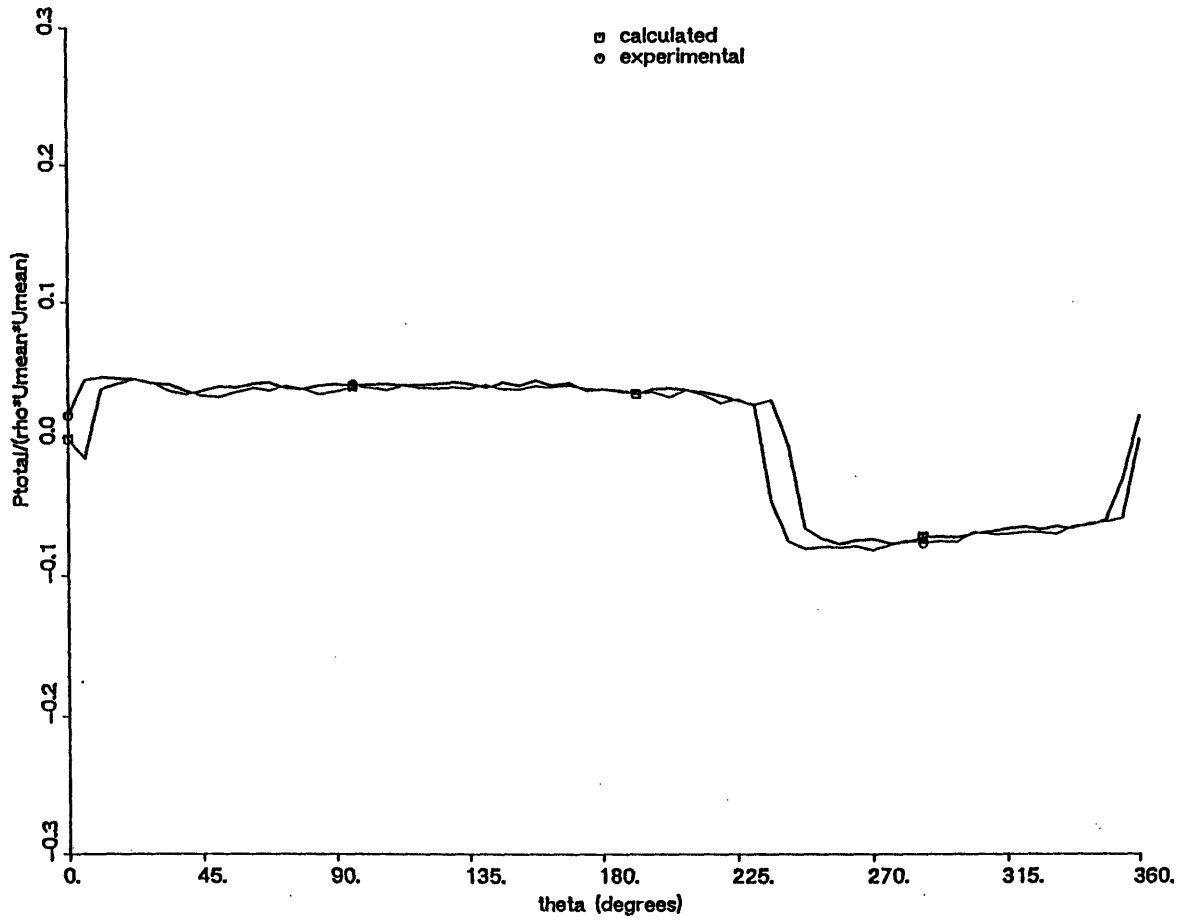

Figure 6-5 Comparison of Calculated and Measured Total Pressure Profiles, at plane 0.45 (.32 radii upstream of IGV's), Near Stall, f=0.0

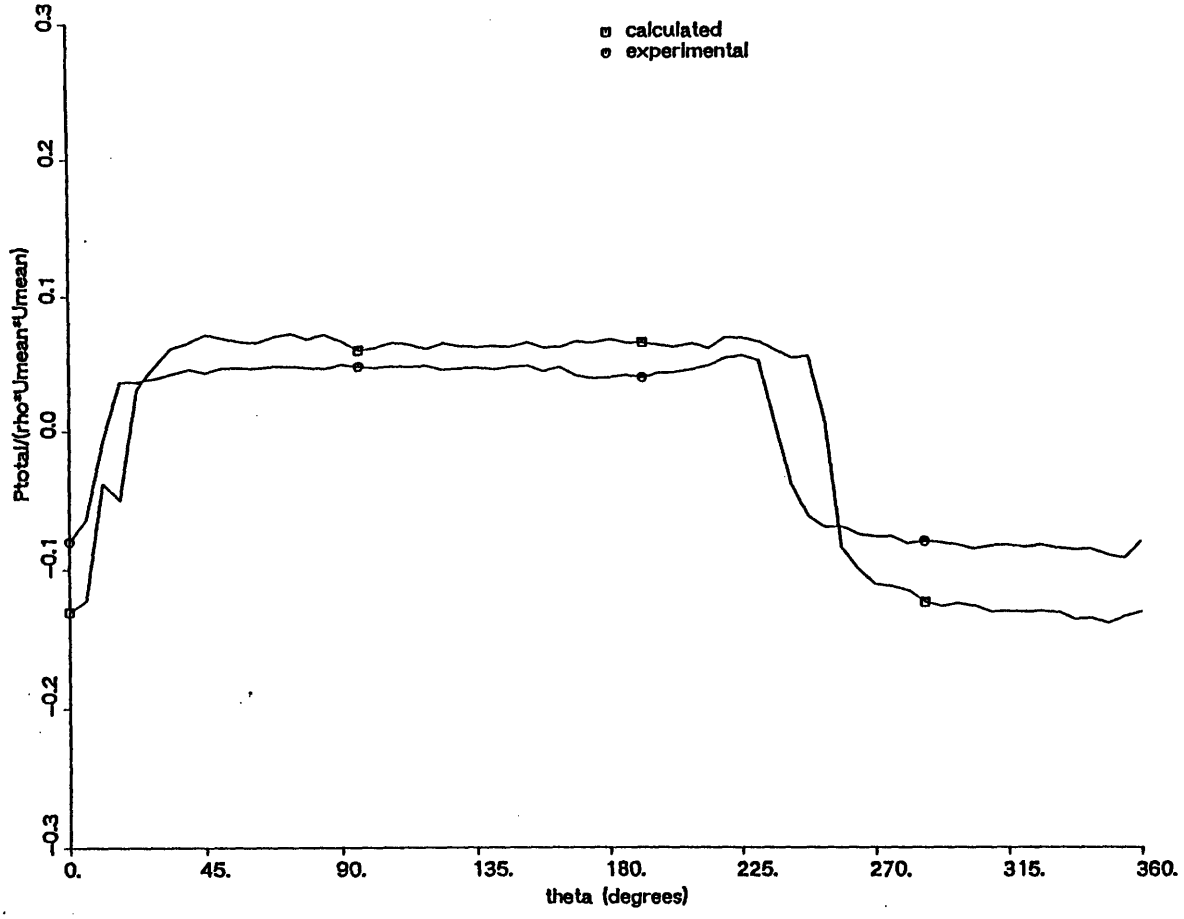

Figure 6-6 Comparison of Calculated and Measured Total Pressure Profiles, at plane 0.45 (.32 radii upstream of IGV's), Near Stall, f=0.3

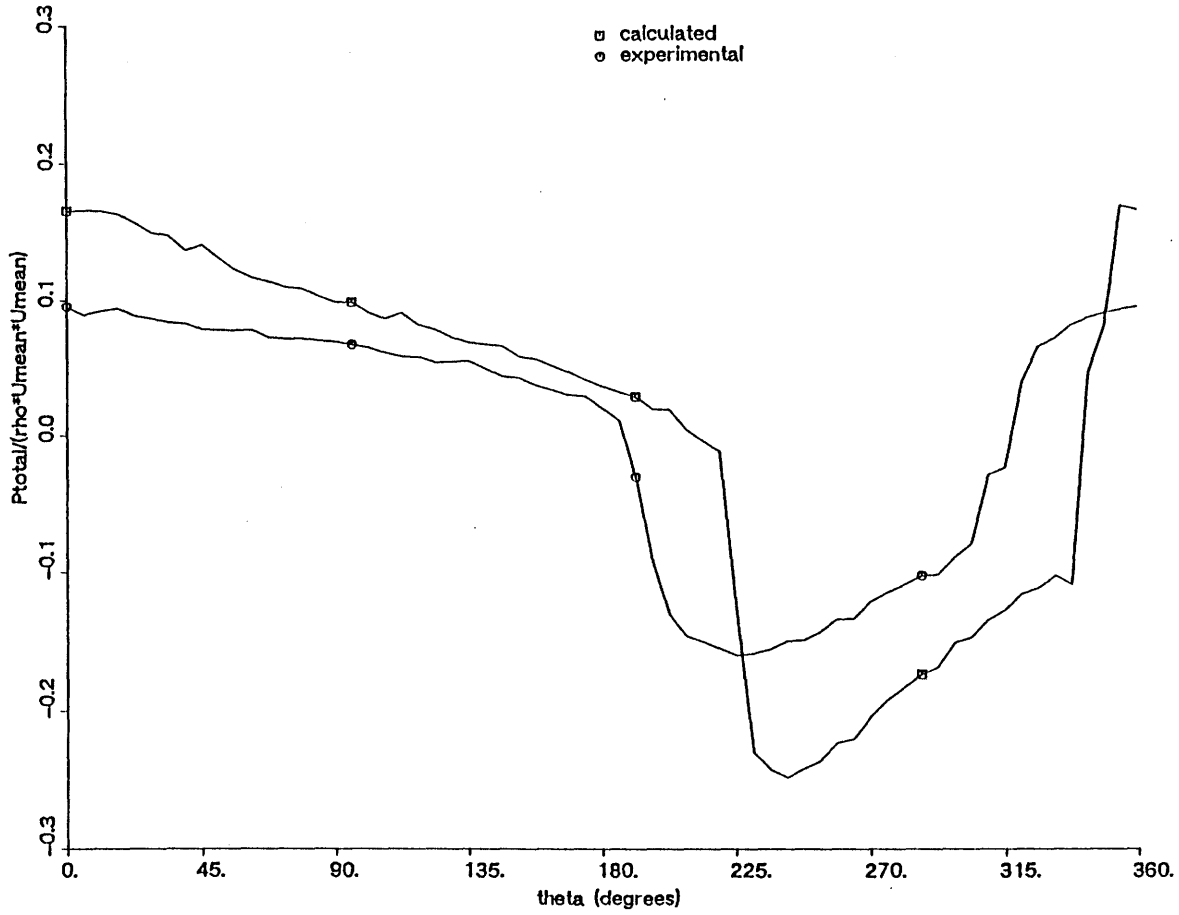

Figure 6-7 Comparison of Calculated and Measured Total Pressure Profiles, at plane 0.45 (.32 radii upstream of IGV's), Near Design, f=-0.6

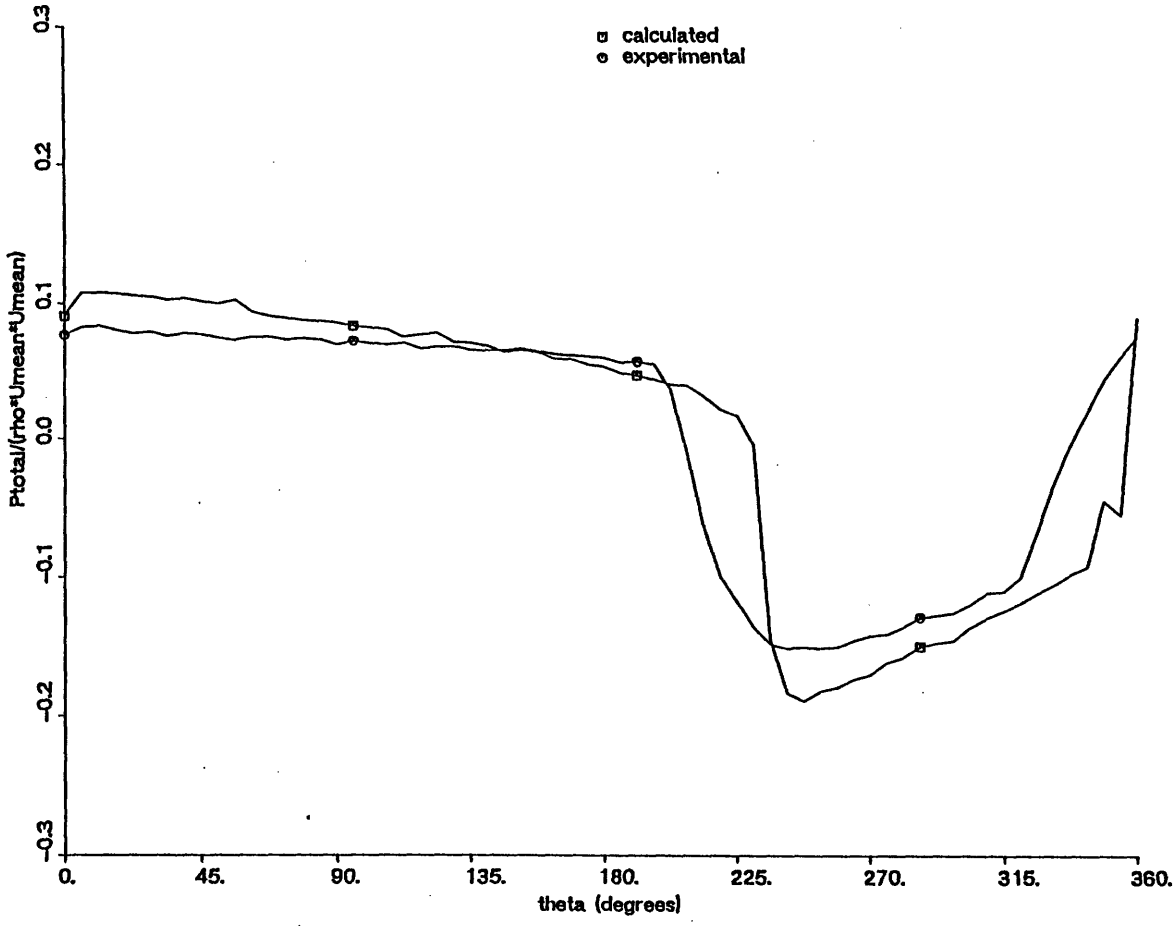

Figure 6-8 Comparison of Calculated and Measured Total Pressure Profiles, at plane 0.45 (.32 radii upstream of IGV's), Near Design, f=-0.3

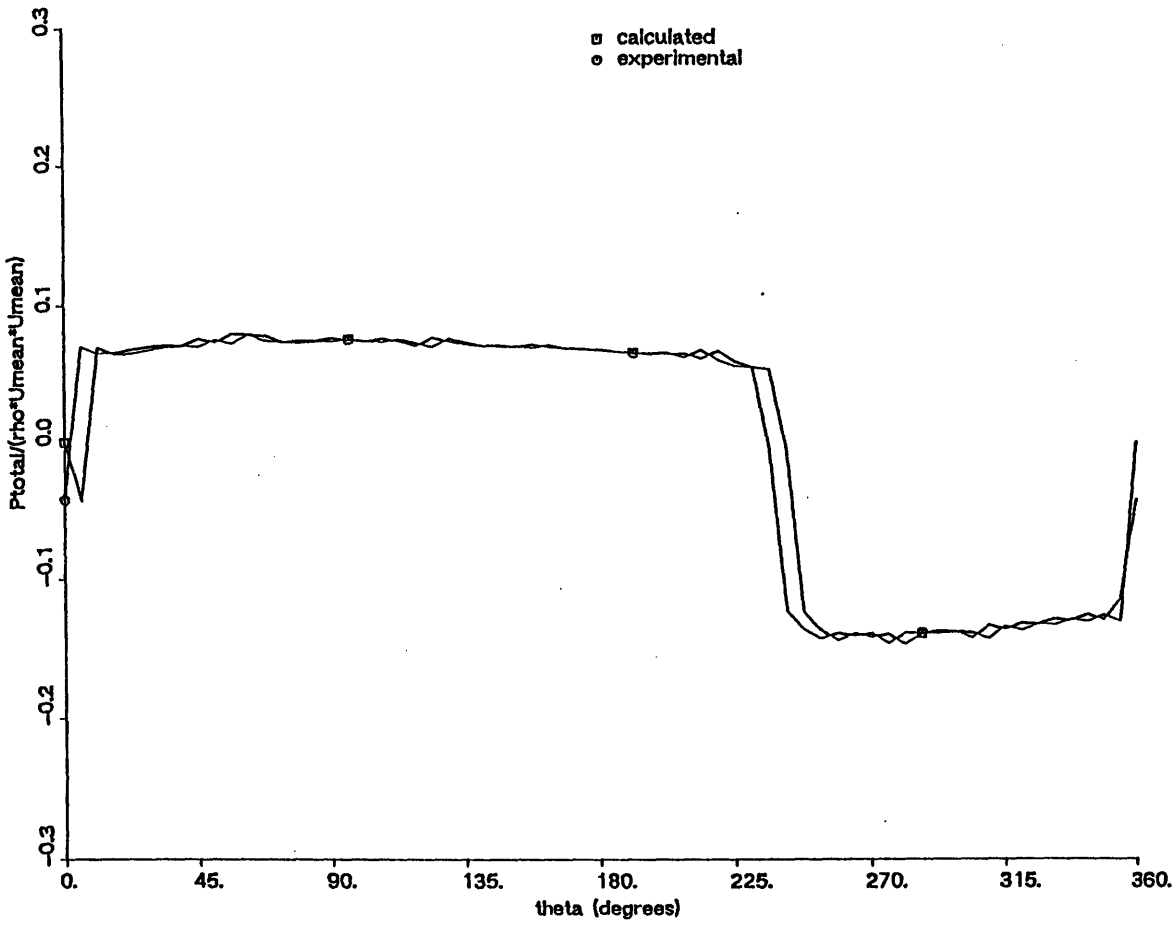

Figure 6-9 Comparison of Calculated and Measured Total Pressure Profiles, at plane 0.45 (.32 radii upstream of IGV's), Near Design f=0.0

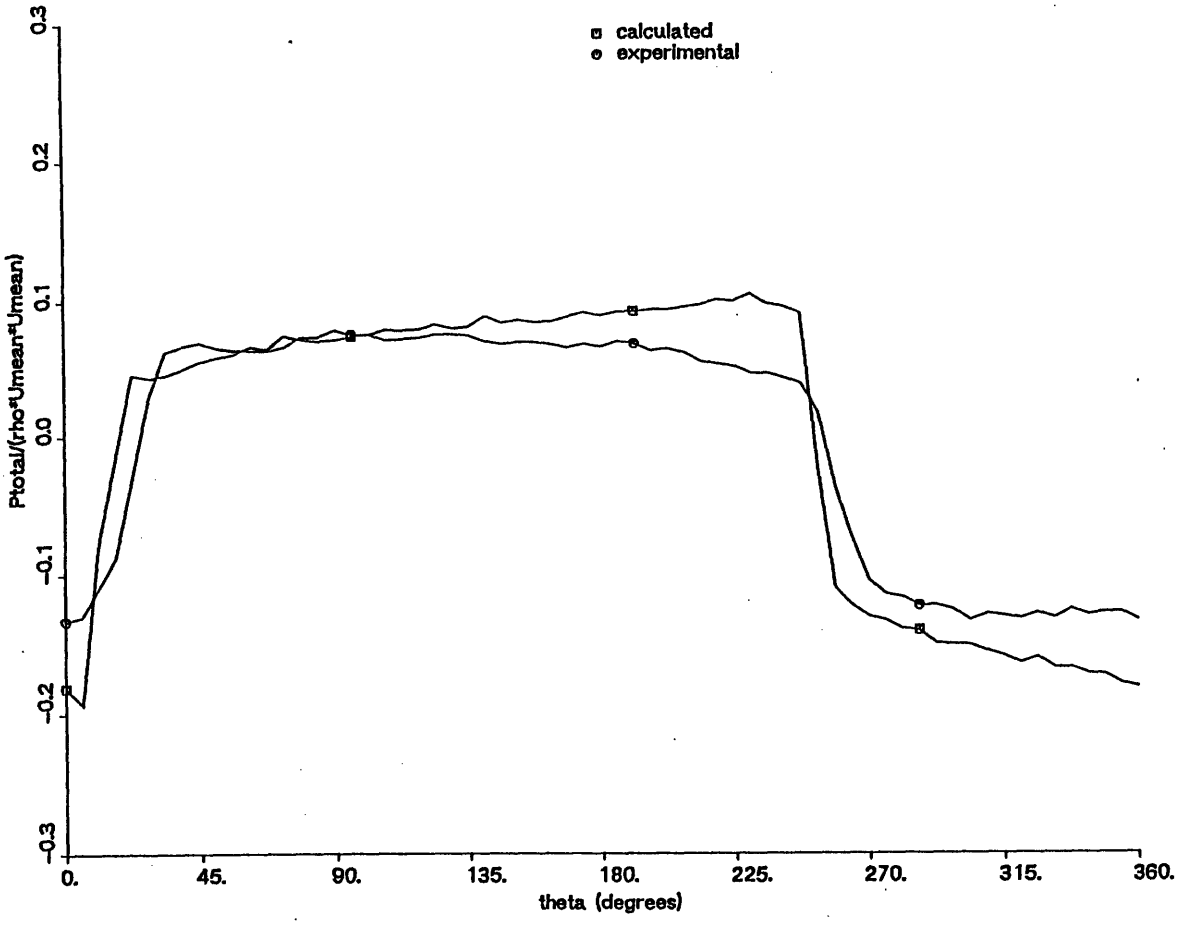

Figure 6-10 Comparison of Calculated and Measured Total Pressure Profiles, at plane 0.45 (.32 radii upstream of IGV's), Near Design, f=0.3

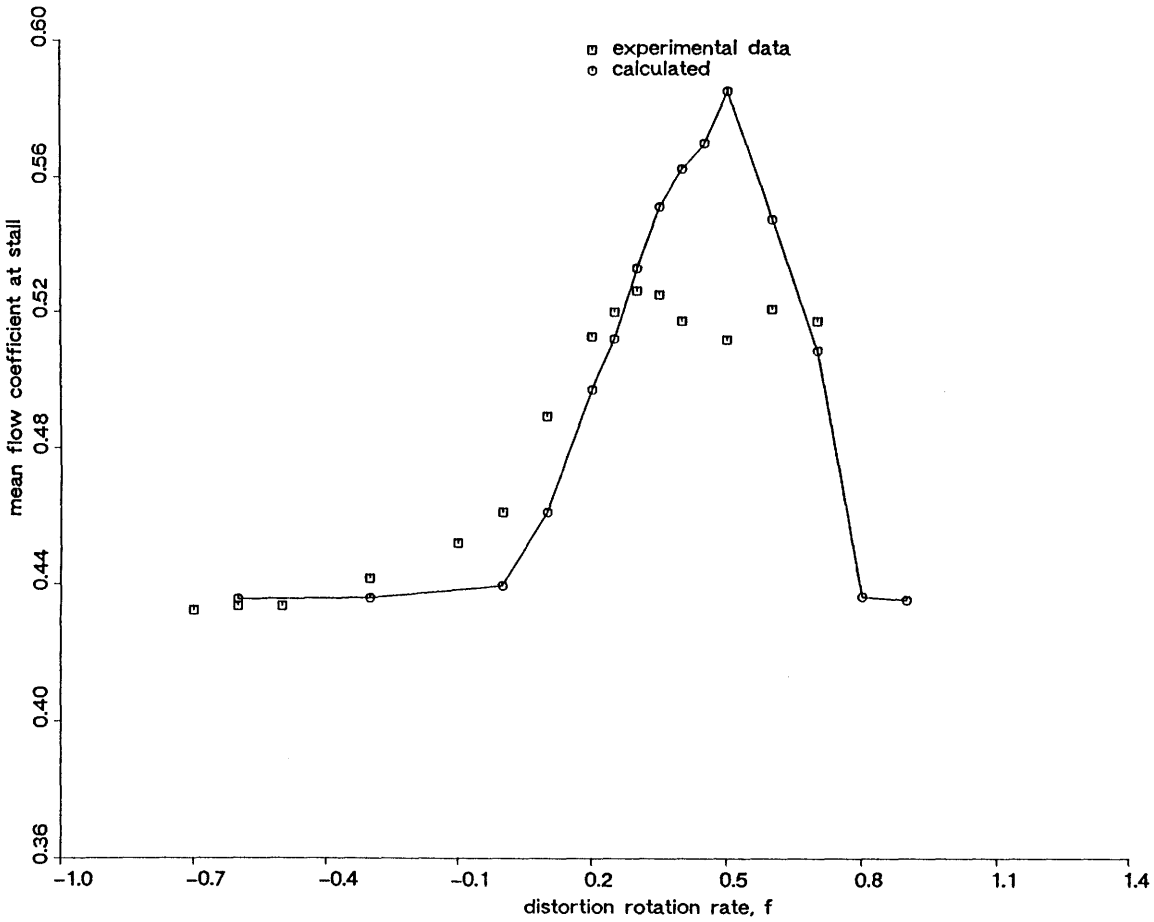

Figure 6-11 Calculated and Experimentally Measured Neutral Stability Flow Coefficients, Heavy Distortion

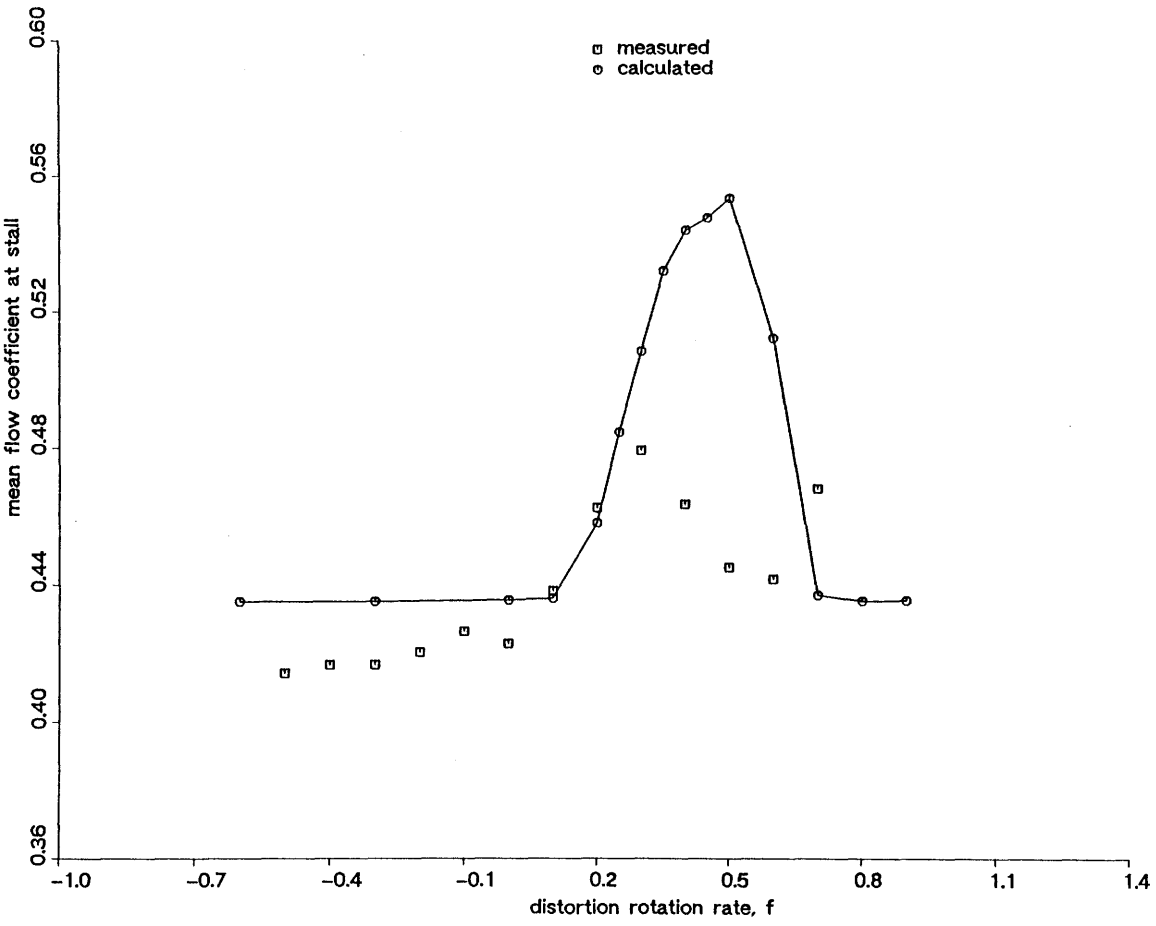

Figure 6-12 Calculated and Experimentally Measured Neutral Stability Flow Coefficients, Double Distortion

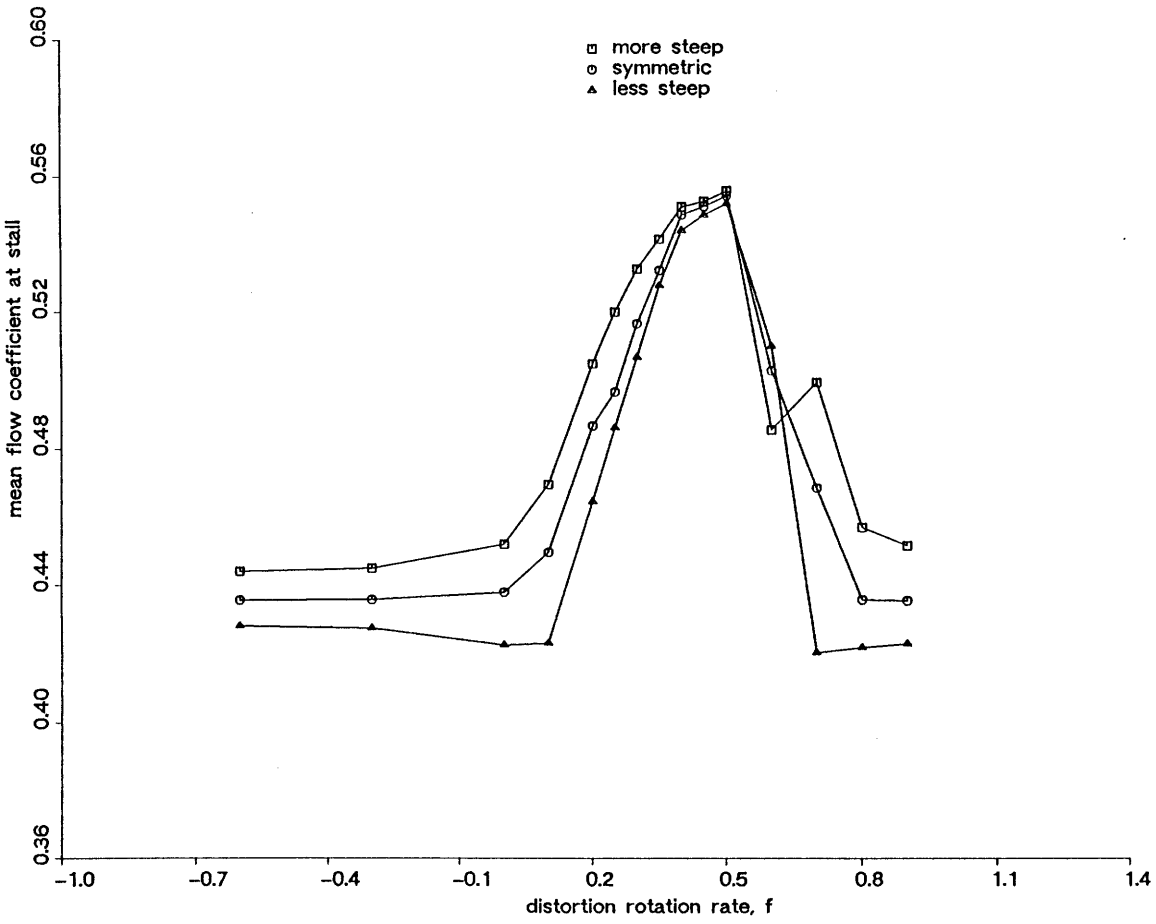

Figure 6-13 Calculated Neutral Stability Flow Coefficients for Characteristics with Variable Steepness, Standard Distortion

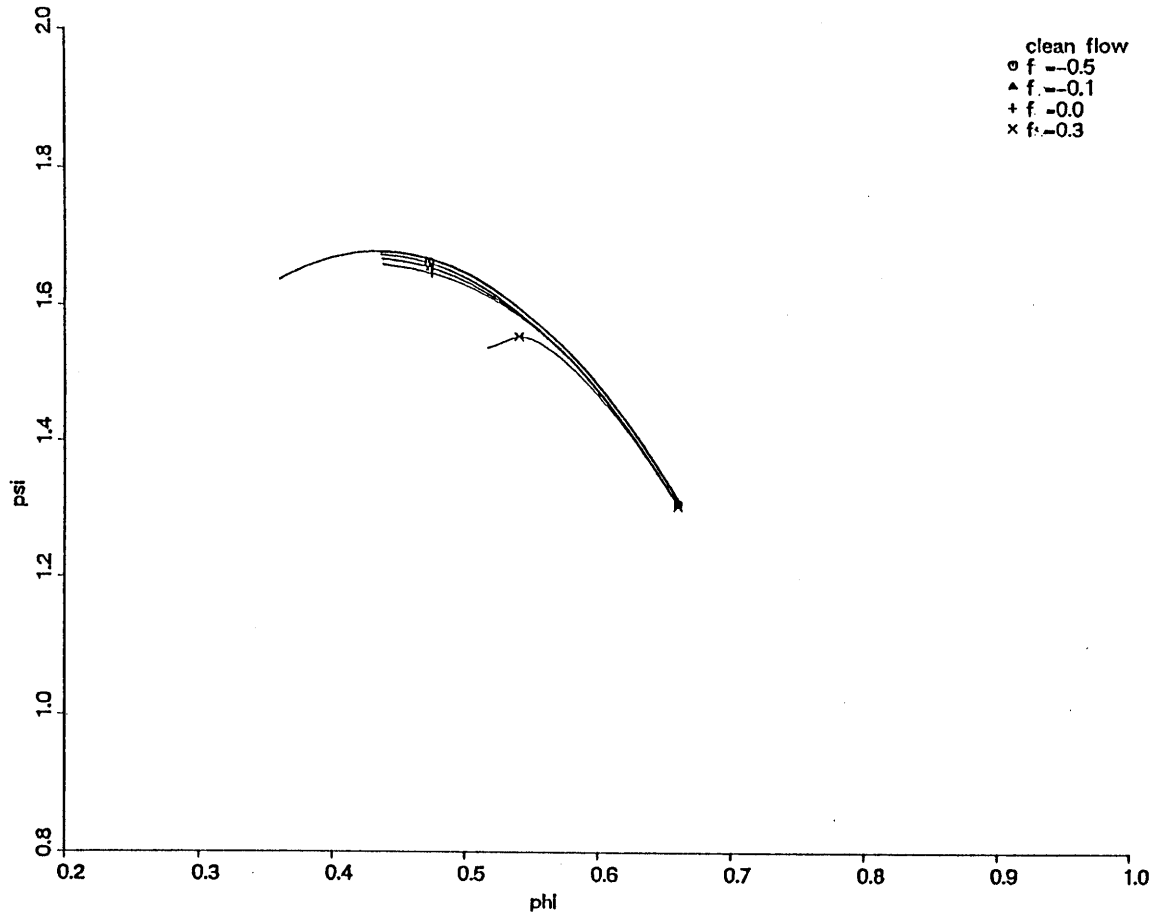

Figure 6-14 Calculated Speedlines for Variable Distortion Rotation Rates, Standard Distortion

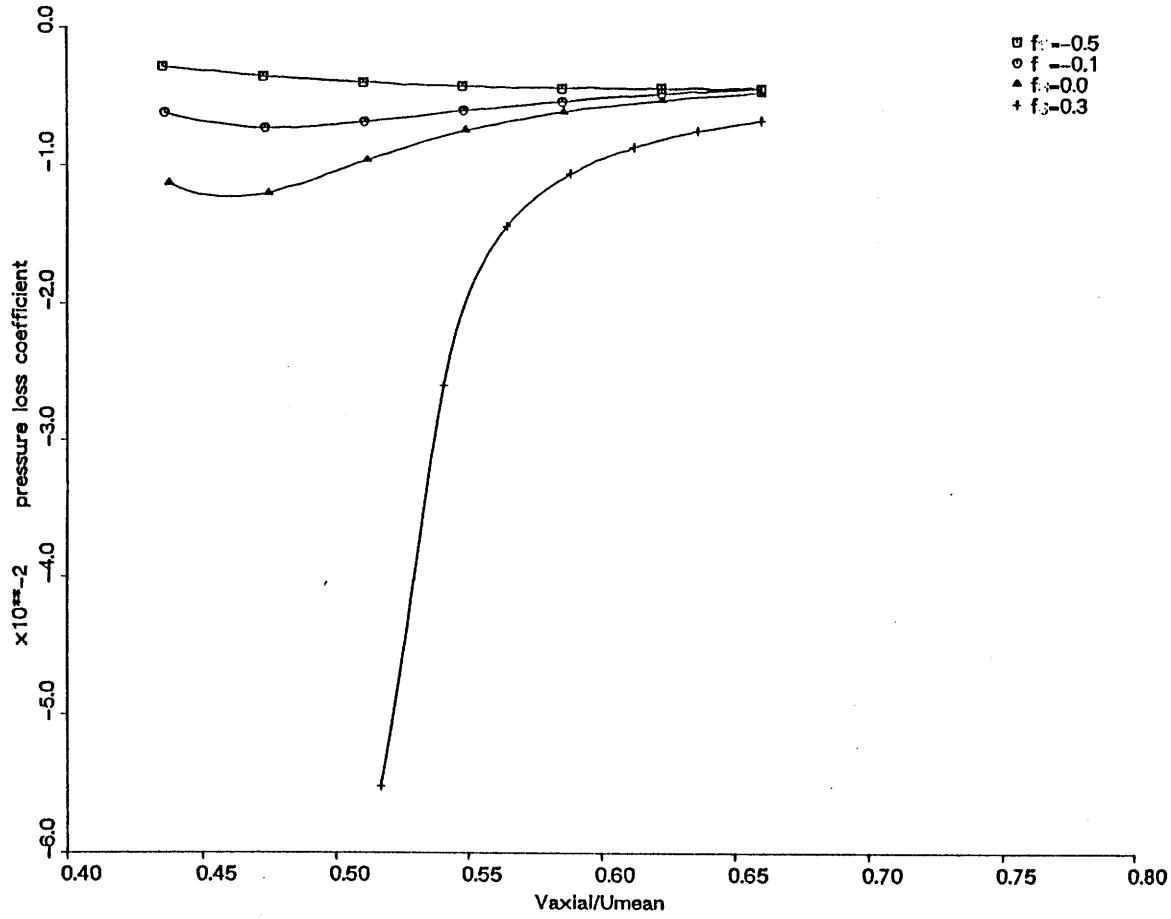

Figure 6-15 Effect of Distortion Rotation Rate on Calculated Pressure Loss

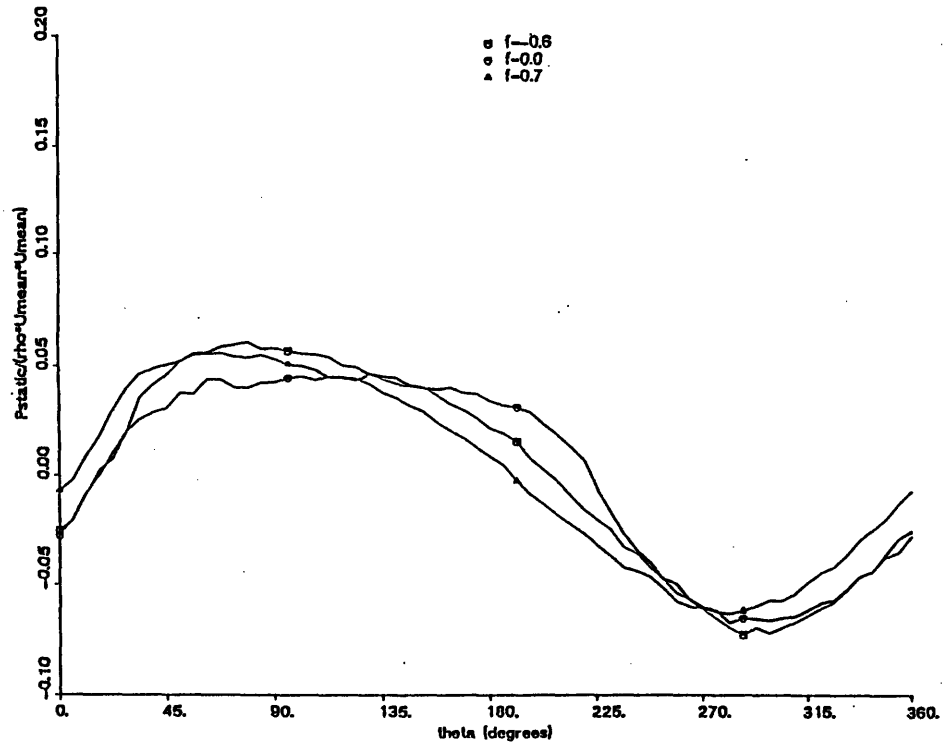

Figure 6-16a Effect of Distortion Rotation Speed on Measured Static Pressure Profiles at Plane 0.45 (.32 radii upstream of IGV's), Near Stall

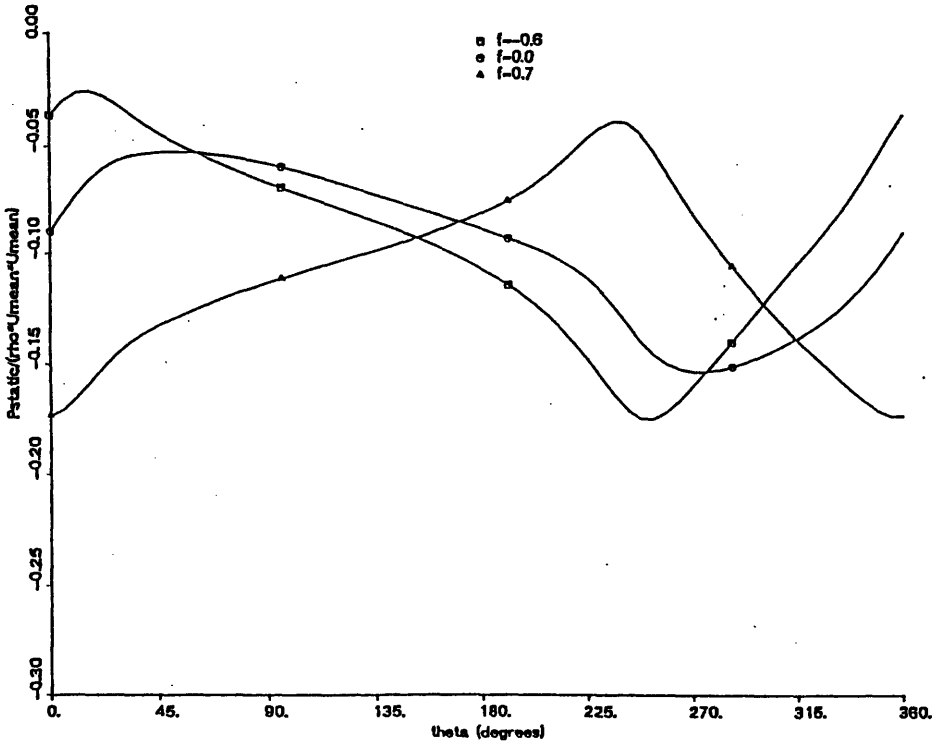

Figure 6-16b Effect of Distortion Rotation Speed on Calculated Static Pressure Profiles at Plane 0.45 (.32 radii upstream of IGV's), Near Stall

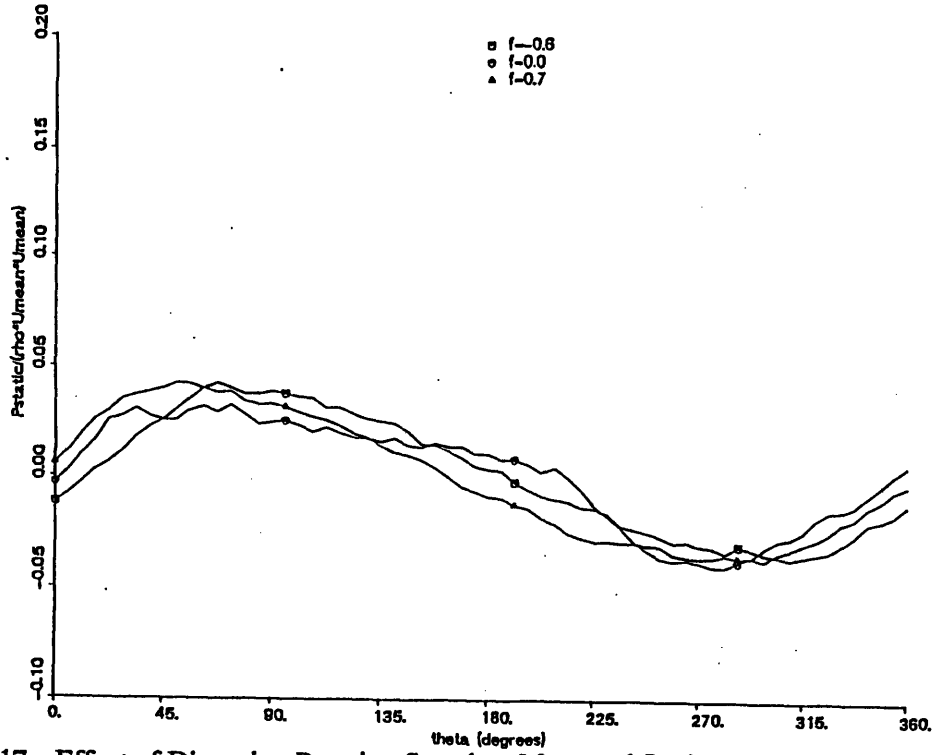

Figure 6-17a Effect of Distortion Rotation Speed on Measured Static Pressure Profiles at Plane 0.45 (.32 radii upstream of IGV's), Near Design

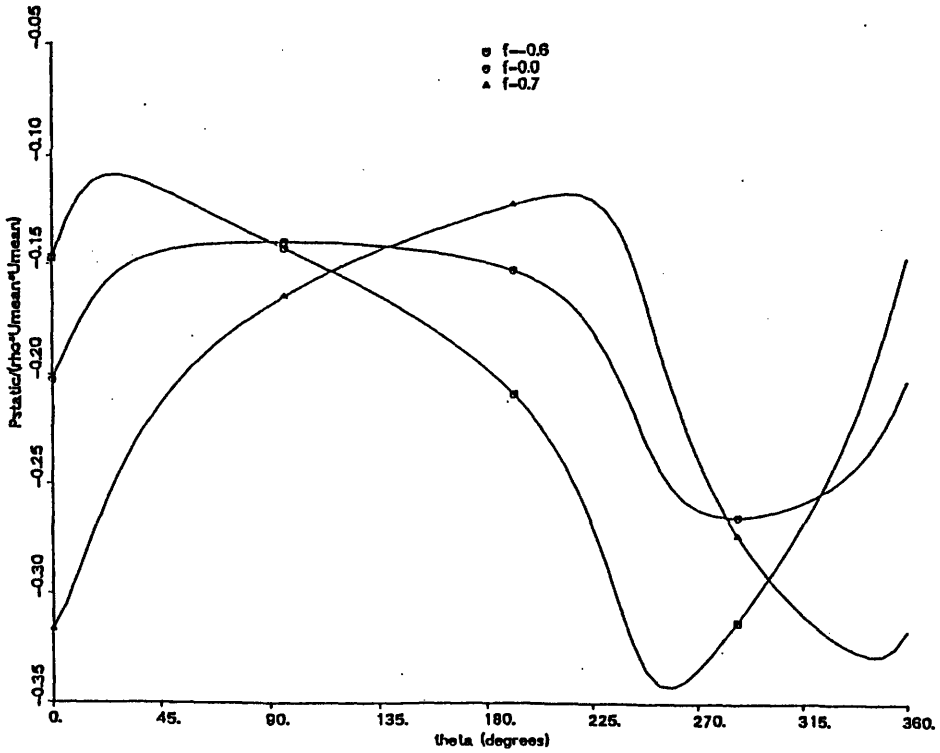

Figure 6-17b Effect of Distortion Rotation Speed on Calculated Static Pressure Profiles at Plane 0.45 (.32 radii upstream of IGV's), Near Design

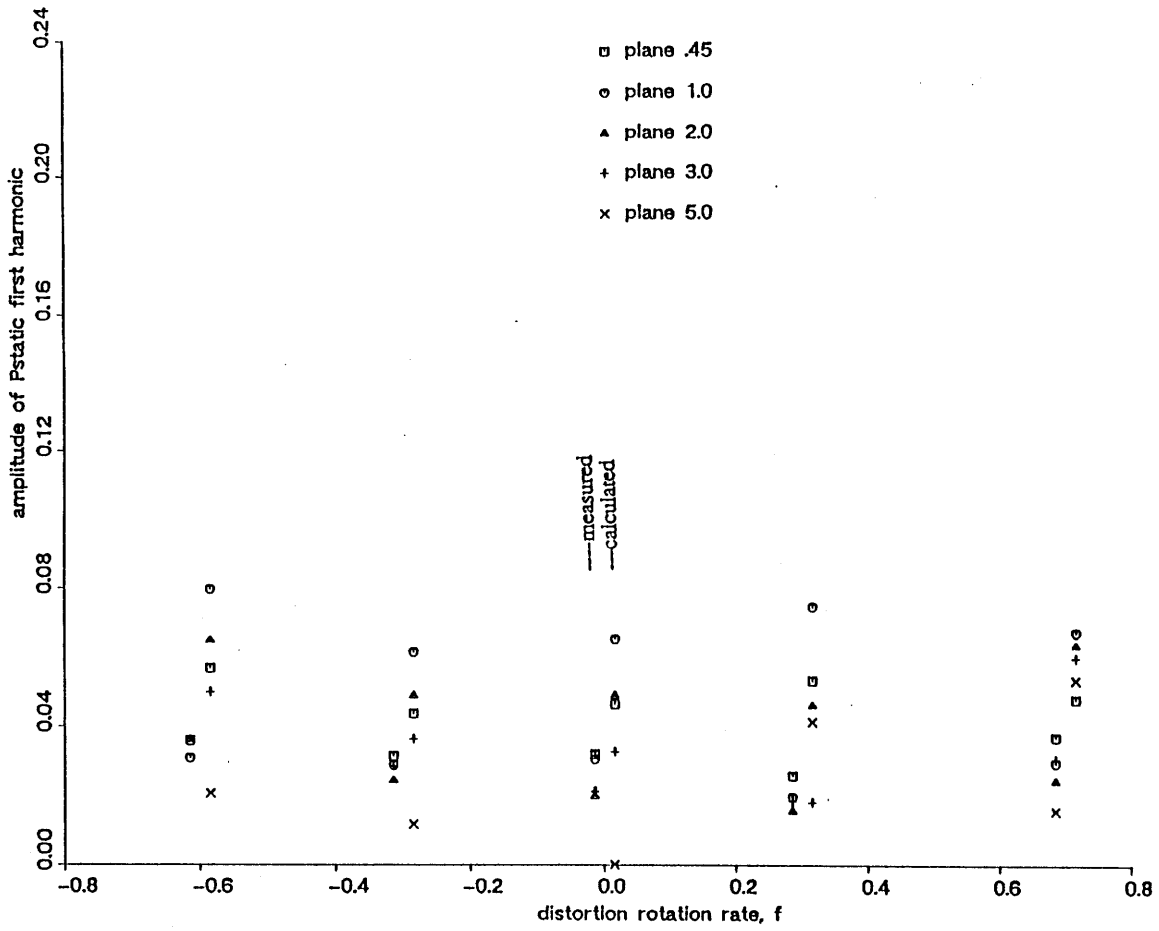

Figure 6-18 Measured and Calculated Amplitude of Static Pressure First Harmonic at Several Axial Locations, Near Stall

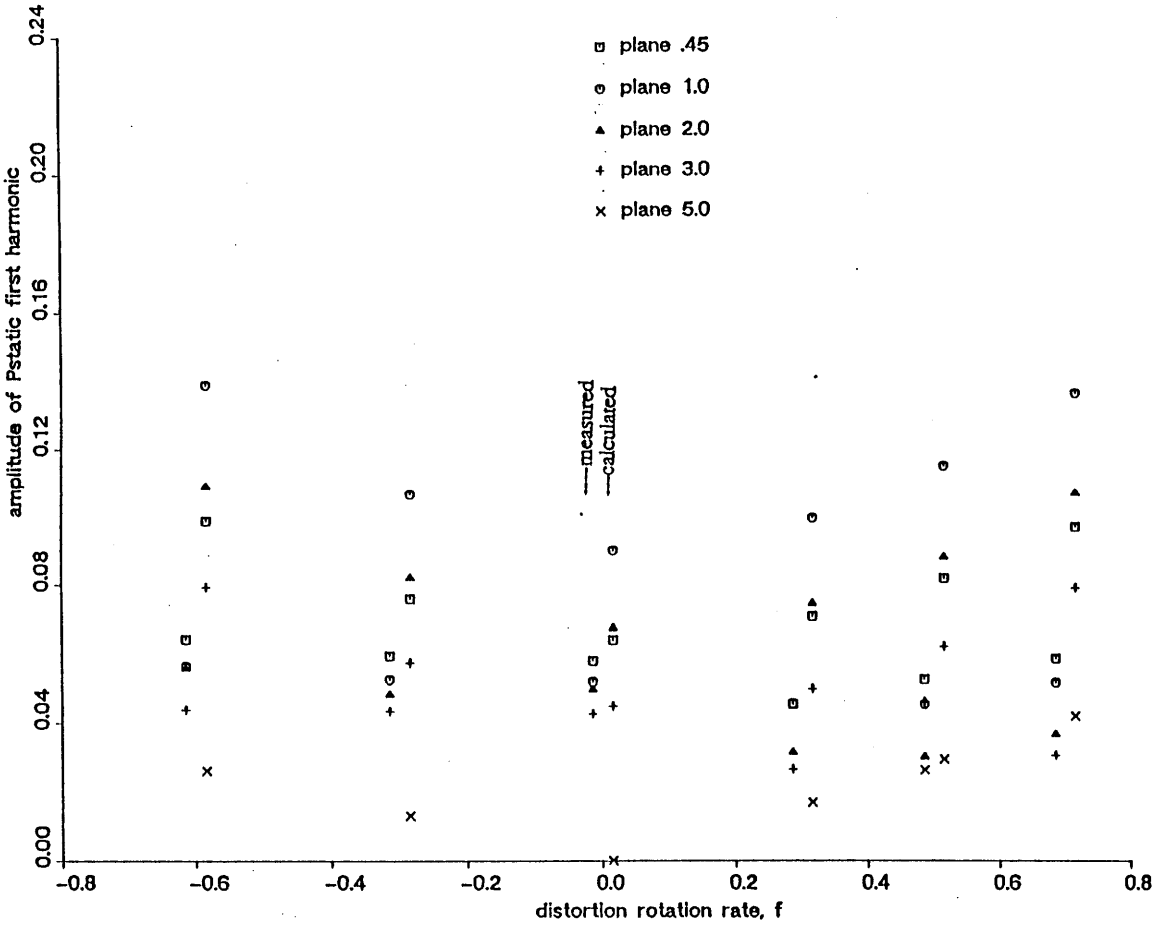

Figure 6-19 Measured and Calculated Amplitude of Static Pressure First Harmonic at Several Axial Locations, Near Design